

A new model for an old camp: The enigmatic Ag-Co-Ni-As-Bi mineralization of
Cobalt, Ontario

by

Louise Victoria Rush

A thesis submitted in partial fulfillment
of the requirements for the degree of
Master of Science (MSc) in Geology

The Faculty of Graduate Studies
Laurentian University
Sudbury, Ontario, Canada

© Louise Victoria Rush, 2021

THESIS DEFENCE COMMITTEE/COMITÉ DE SOUTENANCE DE THÈSE
Laurentian University/Université Laurentienne
Faculty of Graduate Studies/Faculté des études supérieures

Title of Thesis Titre de la thèse	A new model for an old camp: The enigmatic Ag-Co-Ni-As-Bi mineralization of Cobalt, Ontario		
Name of Candidate Nom du candidat	Rush, Louise		
Degree Diplôme	Master of Science		
Department/Program Département/Programme	Geology	Date of Defence Date de la soutenance	April 29, 2021

APPROVED/APPROUVÉ

Thesis Examiners/Examineurs de thèse:

Dr. Dan Kontak
(Co-Supervisor/Co-directeur(trice) de thèse)

Dr. Ross Sherlock
(Co-supervisor/Co-directeur(trice) de thèse)

Dr. Shawna White
(Committee Member/Membre du comité de thèse)

Dr. Eric Potter
(External Examiner/Examineur externe)
supérieures

Approved for the Faculty of Graduate Studies
Approuvé pour la Faculté des études supérieures
Dr. Lace Marie Brogden
Madame Lace Marie Brogden
Acting Dean, Faculty of Graduate Studies
Doyenne intérimaire, Faculté des études

ACCESSIBILITY CLAUSE AND PERMISSION TO USE

I, **Louise Rush**, hereby grant to Laurentian University and/or its agents the non-exclusive license to archive and make accessible my thesis, dissertation, or project report in whole or in part in all forms of media, now or for the duration of my copyright ownership. I retain all other ownership rights to the copyright of the thesis, dissertation or project report. I also reserve the right to use in future works (such as articles or books) all or part of this thesis, dissertation, or project report. I further agree that permission for copying of this thesis in any manner, in whole or in part, for scholarly purposes may be granted by the professor or professors who supervised my thesis work or, in their absence, by the Head of the Department in which my thesis work was done. It is understood that any copying or publication or use of this thesis or parts thereof for financial gain shall not be allowed without my written permission. It is also understood that this copy is being made available in this form by the authority of the copyright owner solely for the purpose of private study and research and may not be copied or reproduced except as permitted by the copyright laws without written authority from the copyright owner.

Abstract

The recent emergence of Co as a critical metal used in a variety of high-technology industries has refocused exploration at Cobalt, Ontario. This district represents an unusual ore deposit-type termed the five-element (Ag-Ni-Co-As-Bi) assemblage and was important historically as Canada's former premier Ag producer at over 460 Moz (1904-1989). This study applies a sophisticated analytical protocol consisting of whole rock analysis, petrography, and in-situ mineral analyses (SEM-EDS, LA-ICP-MS) to a sample suite with spatial coverage across the district. These methods constrain geological controls on regional metal distribution, the sequence of alteration and mineralization, and the physiochemical evolution of the system. An updated genetic model for the mineralization involves the veins representing a district-scale homogeneous hydrothermal-metal melt system driven by contact metamorphism and partial melting of pre-existing sulfides in underlying Archean basement rocks. This model enhances understanding of deposit formation and offers refined geochemical vectors to aid ongoing exploration efforts.

Keywords

Cobalt, Five-element mineralization, Arsenides, Reduction, Metal melt, Metal zonation, Coupled dissolution-precipitation

Co-Authorship Statement

Chapter 2 is written as a journal manuscript co-authored by L.V. Rush, D.J. Kontak, R.L. Sherlock, F. Santaguida, and S.E. White. Sample collection, sample preparation, and the characterization of samples using petrographic, cathodoluminescence, and scanning electron microscopes was completed by L.V. Rush. Assay analysis of samples was done by ALS Laboratories. The geochemical assay dataset obtained from this study for metal zonation exercises was merged with that of First Cobalt Corporation, overseen by F. Santaguida. Assay data manipulation and interpretation was done by L.V. Rush. Laser ablation-inductively-coupled-mass-spectrometry spot analyses was done by L.V. Rush and data processing was done by Dr. Jeff. H. Marsh, Post-Doctoral Fellow and LA-ICP-MS Laboratory Director at the Mineral Exploration Research Centre. Fluid inclusion petrography was done by D.J. Kontak and L.V.Rush, and fluid inclusion microthermometry was done by D.J. Kontak. Detailed mapping of the Cobalt district was done by S.E. White. Although the manuscript benefited from revisions and suggestions by co-authors, L.V. Rush, D.J. Kontak, and R.L. Sherlock wrote the drafts of the paper and are responsible for all interpretations presented in the manuscripts and thesis.

Acknowledgments

I would like to thank first and foremost, my research team, whom I learned so much from and will take this with me for the rest of my career. To my primary supervisor Dr. Dan Kontak, who took a chance on a student whom had never taken ore geology but wanted to learn. Thank you for your endless insightful ideas, patient guidance, continued support, and for answering my endless questions throughout this entire process. Thank you for inspiring me to be a better critical thinker, how to avoid rabbit holes (Occam's razor), and how to balance logical reasoning with creative thinking – after all, geology is a science *and* an art. Thank you to my supervisor Dr. Ross Sherlock for writing the grant application, initiating the project, as well as your leadership and exemplary time management, which kept the thesis on track. Thank you also for your constructive comprehension for regional metal zonation data processing and interpretation. Thank you to Dr. Shawna White for the most memorable field season – thank you for guidance in the field, extensive knowledge of Cobalt geology, being the fearless leader of the Cobalt transect field team, but most of all, thank you immensely for grounding me throughout my masters with your relatable wit and wise advice. I would like to thank Dr. Eric Potter for acting as my external examiner for this work.

A special thanks to Dr. Frank Santaguida, the VP of Exploration at First Cobalt Corporation for co-writing the research grant, for your generosity in providing drill core material, insight into data manipulation, and for your enthusiasm for such a unique style of mineralization. Thank you to Meghan Hewton with First Cobalt Corporation for your guidance through the FCC database. In further regards to funding, thank you to First Cobalt Corporation and the Ontario Centres of Excellence for the research grant that started it all. Thank you to the Ontario Graduate Scholarship committee for the additional funding, which made the load much lighter.

Thank you to Dr. Jeff Marsh for guidance and support with the SEM and LA-ICP-MS, Metal Earth technical staff Kipp Grose, who helped with IT, and Dean Meek who helped tremendously with GIS and Microsoft Access softwares. Thank you to field assistants Ryan Wells and Bradley Piche, who made field work a great experience. To Ben Mark, whose zeal for Cobalt is unmatched – the whole research team thanks you for donating the most important sample for the thesis from your personal collection. Thanks to Doug Robinson, a geologist who worked in the Cobalt mines for decades, for sharing his knowledge and many documentations of mineralization. Thank you to Katherine Dunnell at the Royal Ontario Museum who allowed access to, and observation of, the extensive archived collection of mineralized samples from the Cobalt mining camp.

I would like to dedicate this thesis to my family and friends – to my wonderful parents Carole and Edward, and sister/best friend Charlotte. Words cannot illustrate what your endless support means to me. Thank you to my boyfriend, Tanner, for believing in me, encouraging me, understanding how my brain works even though I may not, and patiently helping me work through every challenge – you healed me at a time when I felt lost in this process. Thank you to my life-long and closest friends – you know who you are – I could not have done this without all your support. Finally, thank you to my fellow graduate students at Laurentian. I could name a long list of people I met in Sudbury whom truly inspire me.

Table of Contents

Abstract.....	iii
Co-Authorship Statement.....	iv
Acknowledgments.....	v
Table of Contents.....	vi
List of Tables	viii
List of Figures.....	ix
List of Appendices	xi
Chapter 1.....	1
1 Introduction.....	1
Chapter 2.....	4
2 Abstract.....	4
2.1 Geological Setting.....	6
2.1.1 Superior Province and the Abitibi subprovince.....	6
2.1.2 Cobalt Embayment.....	7
2.1.3 Cobalt district and South Lorrain Township.....	8
2.2 Cobalt Mineralization and Five-Element Vein Genetic Models.....	10
2.2.1 Five-element vein emplacement	10
2.2.2 Previous models of five-element vein formation at Cobalt	11
2.3 Methodology.....	13
2.3.1 Sample collection of mineralized material	13
2.3.2 Geochemistry and QA-QC of mineralized samples.....	13
2.3.3 Sample Characterization	14
2.3.4 In-situ Laser Ablation Inductively Coupled Plasma Mass Spectrometry (LA ICP-MS) of vein carbonates.....	15
2.3.5 Fluid inclusion petrography and microthermometry	16
2.4 Results.....	16
2.4.1 General features of five-element veins and wallrocks.....	16
2.4.2 Composite petrography of five-element veins.....	17
2.4.3 Mineral paragenesis of five-element veins	19
2.4.4 Mineral chemistry of five-element vein assemblage	20

2.4.5	Chemistry of five-element vein samples: Regional zoning and implications for mineralogy	21
2.4.6	Cathodoluminescence imaging of vein quartz and carbonate.....	26
2.4.7	Chemistry of vein carbonates.....	27
2.4.8	Fluid inclusion studies of five-element veins from the Cobalt district.....	29
2.5	Discussion.....	32
2.5.1	Regional metal zonation and implications.....	32
2.5.2	Geochemical and petrographic features of the five-element veins.....	33
2.5.3	Oxidation controls on the five-element vein paragenesis.....	38
2.5.4	Carbonate REE and trace element data.....	41
2.5.5	Fluid inclusions.....	44
2.6	Refining the genetic model for Cobalt five-element mineralization	45
2.6.1	Review of earlier models	45
2.6.2	An updated genetic model for the Cobalt deposits: Interflow sedimentary sulfide partial melting: metal source, mobilization, and concentration	47
2.7	Conclusion	52
	References.....	55
	Tables.....	65
	Figures.....	81

List of Tables

Table 1. Mineral abbreviations.....	65
Table 2. Representative SEM raster data of bulk native silver-arsenides.....	66
Table 3. Representative SEM spot analysis data for arsenides and sulfarsenides.....	67
Table 4. Representative SEM spot analysis data for Ag and Bi minerals.....	70
Table 5. Elemental ranges of five-element vein assay values.....	71
Table 6. Representative five-element vein assay data for mineral groupings.....	72
Table 7. Representative SEM spot analysis data for five-element vein carbonate.....	74
Table 8. LA-ICP-MS major, trace, and REE data of five-element vein carbonate.....	76
Table 9. Fluid inclusion types.....	80

List of Figures

Figure 1. Location of Cobalt, Ontario, Canada with respect to the Abitibi subprovince.....	81
Figure 2. Location and geology setting of the Cobalt district study area.....	82
Figure 3. Idealized stratigraphy of the Cobalt Embayment.....	83
Figure 4. Massive sulfides in Archean argillic sedimentary rock at the Beaver Temiskaming Mine.....	84
Figure 5. Map of sample distribution.....	85
Figure 6. Representative examples of mineralization seen in Cobalt.....	86
Figure 7. Wallrock alteration related to five-element veins.....	87
Figure 8. Photomicrographs of five-element vein paragenetic stages.....	88
Figure 9. Continuation of photomicrographs of five-element vein paragenetic stages.....	90
Figure 10. Summary of mineral paragenesis.....	92
Figure 11. SEM-BSE images of representative primary native silver dendrite crystals with arsenides.....	93
Figure 12. Ternary diagrams of arsenide and sulfarsenide SEM-EDS data.....	94
Figure 13. Ternary diagrams of Ag-bearing mineral SEM-EDS data.....	95
Figure 14. Representative metal percentile plots of the Cobalt study area.....	96
Figure 15. Representative mineral groupings plots of the Cobalt study area.....	97
Figure 16. Ternary diagrams of five-element vein assay data.....	98
Figure 17. Binary diagrams of five-element vein assay data featuring Ni-Co-Bi-As-Sb.....	99

Figure 18. Binary diagrams of five-element vein assay data featuring Ag as a function of Ni-Co-Bi-As-Sb.....	101
Figure 19. Binary diagrams of five-element vein assay data featuring Cu, Pb, and Zn.....	102
Figure 20. Cathodoluminescence (CL) images of quartz and carbonate vein gangue.....	103
Figure 21. Five-element vein carbonate major and trace element chemistry.....	104
Figure 22. Representative REE patterns of five-element vein dolomite and calcite.....	105
Figure 23. Petrographic images of fluid inclusion (FI) types in five-element veins.....	107
Figure 24. Schematic diagram of fluid inclusion assemblages (FIA) in the five-element veins.....	108
Figure 25. A representative sequence of minerals all with CDP mineral boundaries.....	109
Figure 26. Revised Cobalt model.....	110

List of Appendices

Appendix A: Image Archives of the Base-Metal Sulfide Content of the Archean Interflow Sedimentary Rocks.....	111
Appendix B: Five-Element Vein Assay Methods for Regional Geochemistry.....	113
Appendix C: QA-QC Protocol for Five-Element Vein Assay Data.....	116
Appendix D: The Five-Element Assay Database.....	159
Appendix E: Additional Material for ICP-MS Analysis	166
Appendix F: Petrography, SEM-EDS, and Fluid Inclusion Work.....	205
Appendix G: Additional Material for Percentile and Mineral Groupings	212
Appendix H: Summary of Field Work Report 2019.....	270
Appendix I: Mineral Exploration Research Center Industry Field Trip Guide: Geology, Mineralization, and Mining History of the Cobalt Region, Cobalt, Ontario.....	281
Appendix J: The Prospectors & Developers Association of Canada (PDAC) Student Mineral Colloquium (SMC) Poster: Tracing the origin of metals and fluid in the enigmatic Ag-Co-Ni-As-Bi deposits of Cobalt, Ontario.....	299
Appendix K: The Geological Association of Canada-Mineralogical Association of Canada (GAC-MAC) – GeoConvention Poster: Constraining the origin of metals and fluid in the enigmatic Ag-Co-Ni-As-Bi deposits of Cobalt, Ontario.....	301

Chapter 1

1 Introduction

The recent emergence of cobalt as a critical metal, due to its use in a variety of high-technology industries, has refocused exploration on the enigmatic five-element (Ag-Ni-Co-As ± (Bi, U)) veins at Cobalt, Ontario. This historic mining center was Canada's former premier Ag camp, with over 500 Moz (14,000 tonnes) of Ag, in addition to approximately 45 Mlbs (20,400 tonnes) of Co, 1 Mlbs (450 tonnes) of Ni, and 5 Mlbs (2,300 tonnes) of Cu produced between 1904 – 1989 (Sergiades, 1968). The demand for cobalt, combined with the historic significance of that camp, is why we chose to reexamine the region using modern modern exploration efforts.

Five-element vein deposits have been described in many parts of the world. Scharrer et al. (2019; and references therein) present a comprehensive compilation of these deposits globally, including comparisons of mineralogy, fluid physiochemical conditions, and host rock lithologies. Some of the more well studied deposits are in Europe and include the Erzgebirge Ore Mountains of Germany and the Czech Republic (Müller, 1860; Hofmann, 1992; Baumann et al., 2000), the Odenwald district of Germany (Burisch et al., 2017), and the Penninic Alps of Switzerland (Jaffe, 1986; Kreissl et al., 2018). Canadian examples include Cobalt (Andrews et al., 1986; Kerrich et al., 1986., Marshall et al., 1993; Potter and Taylor, 2010), the Thunder Bay area (Franklin et al., 1986), the Echo Bay-Great Bear Lake area (Robinson and Ohmoto, 1973; Changkakoti and Morton, 1986; Changkakoti et al., 1986), and the East Arm Basin of Great Slave Lake (Burke et al., 2018).

Five-element vein deposits refer to a metal assemblage that generally consists of Ag, Ni, Co, Bi, As with variable amounts of Pb, Zn, Cu, Sb, U, and Au, with no specific genetic implication. The metal assemblages tend to be deposit-specific with differences in tectonic settings, host lithology, deposit ages, and physical-chemical characteristics of the hydrothermal fluids (Boyle 1968; Kissin, 1992). Conventional models suggest variation of hydrothermal origins. However, the metal association can occur in a variety of environments, from paleo-rift settings (Kissin, 1992), to remobilization during metamorphism of earlier ores (Lawrence, 1968; Dunham et al., 1978) such as SEDEX deposits (e.g. Broken Hill, Australia; Frost et al., 2002). The Erzgebirge and Cornwall districts, known as magmatic-hydrothermal Sn-W systems, host five-element veins as a late remobilization of metals into veins cross-cutting earlier Sn and base metal veins (Dunham et al., 1978; Kissin, 1992). Thus, the five-element association can form by different processes and in different geologic environments.

The present study focuses on the five-element vein deposits in Cobalt, which have a Ag-Co-Ni-As-Bi assemblage. However, these deposits also contain Sb, Cu, Zn, and Pb. The mineralogy is complex, comprising native metals (Ag, Bi, and Ag-Sb±Hg alloys) with Ni-Co-Fe-arsenides, sulfarsenides, and minor sulfosalts with quartz and carbonate gangue. In addition, rare native As, Sb, Sb-As alloys, Au, and uraninite can occur. The veins commonly form as narrow (cm-scale) open space-infill that pinch and swell (Andrews et al., 1986; Kissin, 1992).

Historically, research in the Cobalt district focused on single veins rather than examining their regional framework. Furthermore, previous studies (e.g., Andrews et al., 1986, and references therein) focused on Ag without consideration of the Co-Ni-arsenide component. Previous analytical research did not utilize in-situ methods, other than the electro microprobe, and thus meaningful trends may have been previously unidentified. This study aims to

understand the Cobalt district by carrying out detailed-examinations of multiple vein systems over a wide area to determine the distribution of Co (-Ni-Ag) assemblages regionally and the fluid evolution over time by using more sophisticated in-situ analytical protocol and methodology. The results of these detailed fluid chemical investigations will develop a more holistic model for controls on mineralization and possible geochemical exploration vectors.

Chapter 2

A new model for an old camp: The enigmatic Ag-Co-Ni-As-Bi mineralization of Cobalt, Ontario

Louise, V, Rush^{1*}, Daniel, J, Kontak¹, Ross, L, Sherlock¹, Frank Santaguida², Shawna, E, White¹

¹*Mineral Exploration Research Centre, Harquail School of Earth Sciences, Laurentian University*

²*First Cobalt Corporation, Toronto, Ontario, Canada*

*louise.v.rush@gmail.com

2 Abstract

The recent emergence of Co as a critical metal used in a variety of high-technology industries has focused exploration on the enigmatic five-element (Ag-Ni-Co-As-Bi) vein systems at Cobalt, Ontario. This district was Canada's premier Ag producer at over 460 Moz (1904-1989). This study applies a sophisticated analytical protocol consisting of integrated whole-rock assay analysis, petrography, fluid inclusion study, and in-situ mineral analyses (SEM-EDS, LA-ICP-MS) to a sample suite with spatial coverage across the district. These methods constrain geological controls on regional metal distribution, the sequence of alteration and mineralization, and the physiochemical evolution of the system. Results indicate metal zonation in the Cobalt district specifically with a Ag-dominated zone with peripheral Ni and Co enrichment. Furthermore, there is a strong covariance among Co-Ni-As-Bi-Sb but variable Ag distribution. The regional metal zonation and coherency of metal ratios suggests a broad thermo-chemical

gradient generated by fluids and/or a host lithology control. At the micro-scale, a mineral paragenesis consists of early native silver, through arsenide to sulfarsenide (from Ni to Co to Fe solid-solution), and to later overprinting base-metal sulfides. Moreover, dendritic silver displays textures indicative of coexisting melt wetting surfaces. Coupled dissolution-precipitation (CDP) textures record replacement of the arsenides by later sulfarsenides, and there is a clear late stage remobilization of native metals (Ag, Bi). Therefore, the regional metal zoning and decoupling of Ag from Co-Ni-arsenides alternatively reflects a late-stage mobilization or influx and superimposition of Ag on an existing Co-Ni enrichment. Further analytical results consist of carbonate gangue REE contents, which suggest fluid equilibration with one or more lithologies at depth foreign to the Cobalt district. Detailed fluid inclusion studies confirms the numerousness of syn-ore L-V-H and lesser L-V type inclusions. However, V-rich inclusions are predominant and of H₂O-CO₂-CH₄±N₂ nature. Generation of this mixed volatile fluid strongly suggests variable oxidation of graphite, which is noted in Archean graphitic sedimentary rocks at Cobalt. These integrated results allow for an updated genetic model for the mineralization at Cobalt involving the veins representing a district-scale homogeneous, redox-controlled hydrothermal-metal melt system driven by contact metamorphism and partial melting of pre-existing sulfides in underlying Archean basement rocks. Additionally, the superimposition of different fluids invoking changing chemical parameters (i.e., pH, fO_2) created different evolutionary paths on a local scale within the vein network. This model enhances understanding of deposit formation, the cause of the regional metal enrichment, and offers refined geochemical vectors to aid ongoing exploration efforts.

2.1 Geological Setting

2.1.1 Superior Province and the Abitibi subprovince

The Superior Province, the largest Archean craton in the world, consists of a wide range of rock types, which record a geologic history of rock formation, metamorphism, and deformation spanning 1.73 billion years (4.3 - 2.57 Ga; Percival et al., 2012). The Abitibi greenstone belt (ABG) makes up the eastern portion of the Wawa-Abitibi subprovince in the southernmost part of the Superior Province (Percival et al., 2012) and forms the basement to the Cobalt Embayment. Volcanic units in the Abitibi subprovince have been subdivided into volcanic-sedimentary assemblages that range from ~2750 to 2695 Ma (Heather, 2001; Ayer et al., 2002a). These volcanic assemblages are separated by laterally extensive 1 to 350 m thick intervals of interflow sedimentary rocks of chemical and clastic nature (Thurston et al., 2008). Synvolcanic and syn- to post-tectonic plutons of gabbro, diorite, tonalite, syenite, and granite intrude the volcanic and sedimentary assemblages (Ayer et al., 2002a; Daigneault et al., 2004). Sedimentary assemblages unconformably overly earlier volcanic assemblages and intrusions, the oldest assemblage (<2690 Ma) referred to as “Porcupine-type” (predominantly turbiditic greywacke; Frieman et al., 2017). These rocks were affected by large-scale folding and thrusting during at least one deformational event prior to 2679 Ma (Monecke et al., 2017). Younger <2672 Ma (Davis, 2002; Ayer et al., 2004a) “Timiskaming-type” (fluvial coarse clastic; Gunning and Ambrose, 1939) sedimentary rocks were deposited unconformably on the older and already deformed rocks of the AGB in successor basin environments (Thurston and Chivers, 1990; Thurston et al., 2008). Subsequent crustal shortening resulted in the structural burial and preservation of Timiskaming assemblage in the footwall of major crustal-scale fault zones which extend across the AGB (Monecke et al., 2017) and these faults are well known for hosting

numerous orogenic gold deposits. Succeeding deformation generated isoclinal-type folding as part of the 2.5 Ga Kenoran (Algoman) Orogeny (e.g. Dimroth et al., 1983).

2.1.2 Cobalt Embayment

The Cobalt Embayment is an extensive region (~ 30,000 km²) where younger Paleoproterozoic cover (i.e., the Huronian Supergroup) unconformably overlies the Archean basement of the southernmost Abitibi subprovince. It is bounded to the N and W by the Abitibi subprovince, the Grenville Orogen to the SE, and Pontiac subprovince to the NE (Andrews et al., 1986) (Fig. 1). In this region the Archean basement including unconformably overlying Timiskaming sedimentary rocks at $>2683.7 \pm 0.9$ Ma (Ayer et al., 2006), as noted above, which records greenschist facies metamorphism and multiple deformation events that account for the map-scale NW-trending, tight to isoclinal folds which define the main map patterns and associated penetrative axial planar foliation (White, 2019). Timiskaming-age syn- to post-tectonic syenitic and monzonitic intrusions (2685 – 2670 Ma, Ayer et al., 2002a), and younger post-tectonic granite (locally termed the Lorrain Granite in the Cobalt district) intrude the volcanic assemblage in the area. Prior to intrusion of the Nipissing gabbro, lamprophyre dikes (Jambor, 1971a) and N-trending Matachewan quartz-gabbroic intrusions (generally 30 m thick, but up to 120 m; Fahrig et al., 1964; Hester, 1967; dated ca. 2485 Ma, Fahrig and Wanless 1963), intrude all older units.

The Paleoproterozoic Huronian Supergroup, a 2.49 – 2.22 Ga succession of predominantly siliciclastic sedimentary rocks, unconformably overlying the Archean basement (Krogh et al., 1984, 1996; Andrews et al., 1986; Smith and Heaman, 1999) (Figs. 2, 3) in the Cobalt district. The 2.2 Ga Nipissing gabbro (Corfu and Andrews, 1986) intrudes all Archean rocks and younger Huronian Supergroup. The youngest intrusions in the area are the

Keweenawan diabase dikes (~30 m thick, Moore, 1956) related to the Keweenawan rift system (also referred to as the Midcontinent Rift, 1200-1100 Ma; Silver and Green, 1972).

Major N-NW to N-NE striking faults extending across the embayment for 100s of kilometers, defining multiple horst and graben structures in the region (Doughty et al., 2013). Local minor faults, of variable orientation, cross-cut both the older basement and younger sedimentary cover (Thomson, 1967). The major faults are interpreted to have formed or been reactivated during rifting and opening of the Huronian basin (Wilson, 1949; Sampson and Hriskevich, 1957; Symons, 1970; Jambor, 1971a; Card et al., 1973). Their reactivation during and after intrusion of the Nipissing gabbro is interpreted to result in normal displacement of 100s meters (Wilson, 1949; Sampson and Hriskevich, 1957; Symons, 1970; Lovell and Caine, 1970; Card et al., 1973).

Although Ag mining occurred at many locations throughout the embayment, the most significant production of Ag-Co-Ni came from the Cobalt district (Sergiades, 1968). These polymetallic vein deposits are located along or proximal to major faults that cross-cut the embayment and extend into the Archean basement. In the Cobalt district, the veins are hosted in the Nipissing gabbro, Huronian sedimentary rocks, and the Archean basement.

2.1.3 Cobalt district and South Lorrain Township

The Cobalt district, located in the eastern part of the Cobalt Embayment, includes the town of Cobalt and Silver Centre (Figs. 1, 2). The Archean basement is exposed in small inliers surrounded by younger Paleoproterozoic siliciclastic rocks. The Archean stratigraphy (Fig. 3) is predominantly pillowed to massive basalt flows (e.g. Thurston, 2002) of tholeiitic affinity with lesser andesites. Intermediate- and felsic calcalkaline volcanic rocks of 2687.4 ± 1.7 Ma occur as massive to brecciated flows and synvolcanic sills (Hamilton, 2006; Jambor, 1971a). The

interflow sedimentary rocks ranging from ~ 40-200 m in thickness (Patterson, 1979) include chert, black shale, siltstone, sandstone, carbonaceous greywacke, reworked tuff, graphitic schists, and thin intervals of banded iron formation (Jambor, 1971a; Petruk, 1971a; Smyk, 1987).

Almost all the historic mine sites in the Cobalt district (>60), particularly those where the five-element veins are hosted in Archean rocks, are noted to contain local accumulations of sulfides in the host rocks (Patterson, 1979; Goodz et al., 1986; Smyk and Watkinson, 1990). This consists of pyrite and pyrrhotite with lesser sphalerite, galena, and chalcopyrite (Patterson, 1979; Goodz et al., 1986) within pillow basalt selvages in the Archean mafic volcanic rocks, as boudinaged nodules, stockwork veinlets, and as massive to semimassive, 1-3 m thick, laterally extensive lenses throughout the interflow sedimentary units (Fig. 4; App. A; Patterson, 1979; Nichols, 1988), or as disseminated sulfides in the Huronian rocks, as described below.

Archean aged sedimentary successions, which outcrop in the NE part of the study area (Fig. 2), include polymictic conglomerate, trough cross-bedded lithic to feldspathic arenite, and planer to massive wacke. These are interpreted as “Timiskiming-type” sedimentary rocks (Ayer et al., 2005) based on a detrital age of $<2683.7 \pm 0.9$ Ma (Ayer et al., 2006), in addition to their lithofacies reflecting deposition in a fluvial-alluvial environment. Similar strata in nearby locations is interpreted to rest unconformably on older volcanic units (Ayer et al., 2005), although the contact is nowhere observed in the Cobalt district.

The Archean-Proterozoic unconformity, a ~300 Ma hiatus in the rock record, is subhorizontal to gently dipping and late broad, open folds expose the unconformity and Archean strata in antiformal cores (e.g., Nipissing Hill; Thomson, 1964a; Fig. 2). In the Cobalt district, only the Cobalt Group of the Huronian Supergroup is exposed (Fig. 3). The lowermost interval, the Gowganda Formation (2288 ± 87 Ma, Fairbairn et al., 1969), which is subdivided into the

Coleman and overlying Firstbrook members (Fig. 3). The former is up to 180 m thick and consists of mono- and polymict diamictite, conglomerate, sandstone, siltstone, and greywacke (Jambor, 1971a). Disseminated syn- and epigenetic pyrite, chalcopyrite, sphalerite, and galena occur in siltstone, whereas the conglomerate contains detrital sulfide clasts, attributed to erosion of pre-existing sulfide material in the Archean basement (Patterson, 1979; Smyk and Watkinson, 1990). The last occurrence of dropstone defines the top of the Coleman Member after which it transitions into the overlying Firstbrook Member (Lindsey, 1967, 1969), 210 – 305 m thick succession of finely-laminated to rippled sandstone, siltstone, and argillite (Jambor, 1971a).

The Lorrain Formation, locally >300 m thick, conformably overlies the Gowganda Formation (Fig. 3). It consists of granule-to-pebble conglomerate, arkose and quartz arenite (Jambor, 1971a). No known five-element veins are hosted in this unit or younger strata (Andrews et al., 1986).

In the Cobalt district, the Nipissing gabbro, having a maximum thickness of 350 m, was emplaced as a complex series of shallow-dipping sills possibly intruded in two pulses with a broad basin and dome-like geometry (Thomson, 1957a; Eakins, 1961; Lovell and Caine, 1970; Owsiacki, 1982). Locally it is observed to follow along faults and the Archean-Paleoproterozoic unconformity, but it also cross-cuts strata (Symons, 1970; Patterson, 1979; Robinson, 1984).

2.2 Cobalt Mineralization and Five-Element Vein Genetic Models

2.2.1 Five-element vein emplacement

The five-element veins of the Cobalt district are hosted by Archean and Huronian rocks as well as the Nipissing intrusions, however, the dominant host is the Coleman Member of the Gowganda Formation (Fig. 3; Bastin, 1939). The veins typically extend 300 m laterally and 100 m vertically. They are often found: (i) proximal to major regional faults; (ii) striking subparallel

to the fabric in Archean rocks; (iii) proximal to the regional Archean-Paleoproterozoic unconformity; (iv) within 200 m of the Nipissing gabbro; (v) localized to lithological contacts; (vi) intersecting shallow-dipping quartz-calcite-sulfide veins and shear zones; and (vi) proximal to sulfide-rich, interflow sedimentary rocks of Archean age (Miller, 1913; Knight, 1924; Bastin, 1939; Petruk, 1971a; Andrews et al., 1986; Nichols, 1988; Marshall and Watkinson, 2000).

The aforementioned quartz-calcite-sulfide veins are a distinct vein set distinguished by their subhorizontal orientation and the absence of five-element mineralization, apart from intersections with the subvertical five-element veins. Their mineralogy consist of quartz, potassic feldspar, epidote, axinite, minor carbonate, with intervals containing massive pyrite, pyrrhotite, chalcopyrite, sphalerite, galena, and trace native bismuth (Petruk, 1971a; Andrews et al., 1986). Cross-cutting relationships indicate that these veins are coeval or slightly postdating the five-element veins (Jambor, 1971a; Andrews et al., 1986). They occur up to 15 cm thick and are noted to cross-cut the Archean basement and Coleman rocks (Jambor, 1971a). Additional observation of sulfide-dominated veins occur (i) extending parallel to the margins of five-element veins, sometimes offsetting or converging with them, resulting in sulfide overprint and/or replacement (Petruk et al., 1971d), and (ii) as subvertical extensions of five-element veins whereby the five-element mineralization is enriched at the tops of vein bodies, which grade to sulfide-dominated with greater depth into the Archean mafic volcanic rocks (Petruk, 1971a).

2.2.2 Previous models of five-element vein formation at Cobalt

A number of studies propose various genetic models for five-element vein formation, which are consolidated and summarized in Kissin (1992), Marshall et al. (1993), and Marshall and Watkinson (2000): (i) a *magmatic-hydrothermal model* whereby the metalliferous fluid was sourced from the cooling Nipissing gabbro (Bastin, 1939; Sampson and Hriskevich, 1957;

Jambor, 1971g; Scott, 1972); (ii) a *metamorphic-hydrothermal model* where the Nipissing gabbro promoted fluid circulation with leaching of metals from Archean organic-rich black shales, pre-existing massive sulfide-rich beds, or mafic volcanic rocks (Boyle and Dass, 1971b; Goodz et al., 1986; Kerrich et al., 1986; Thorpe et al., 1986, and Smyk and Watkinson, 1990); (iii) a *foreign fluid model* whereby juvenile fluids sourced at depth at the crust-mantle boundary ascended via deep-rooted structures (Halls and Stumpfl, 1972); and (iv) a *rifting model*, which suggests circulation of basinal brines from the Huronian rocks was triggered by periods of extension and related to high-crustal heat flow (Kissin, 1988). Common to all models is the role of the Nipissing gabbro as a key component in ore formation due to its spatial relationship with the veins. However, the role of the gabbro as either a metal/fluid source, heat agent, and/or structural trap remains controversial (Andrews et al., 1986; Kerrich et al., 1986; Potter, 2009, 2010).

Several studies address possible mechanisms for precipitation of the five-element vein assemblage for Cobalt and elsewhere, which include: (i) simple cooling of a Ag-saturated fluid (Kissin, 1992; Marshall and Watkinson, 2000); (ii) fluid mixing and related dilution of a metal-rich saline brine with a low salinity fluid of likely meteoric origin (Marshall et al., 1993); (iii) boiling of Ag-saturated fluid with its unmixing into low- and high-salinity fluids (Kerrich et al., 1986); (iv) rapid reduction of an oxidized, metal-rich solution due to mixing with a reductant in structural traps (Markl et al., 2016; Burisch et al., 2017); and (v) continuous reduction of oxidized metal-rich fluids by reaction with, and oxidation of, Fe²⁺-bearing minerals (e.g., siderite) in mafic volcanic rocks (Robinson and Ohmoto, 1973; Kreissl et al., 2018).

Possible reductants relevant to the Cobalt district are: (i) pre-existing sulfides, such as in the organic, black shales containing massive sulfides (Kissin, 1992); (ii) organic carbon such as

graphite in sedimentary units or fault gouge (Kissin, 1992; Essarraj et al., 2005; Scharrer et al., 2019); (iii) hydrocarbons in the sedimentary strata, which is an integral part of the model for European five-element veins (Markl et al., 2016; Burisch et al., 2017) and not dismissed for vein genesis at Cobalt (Naumov et al., 1971a; Kerrich et al., 1986; Kissin, 1992; Marshall and Watkinson, 2000; Potter and Taylor, 2010); or (iv) Fe-rich minerals from volcanic units of the Archean basement (Robinson and Ohmoto, 1973; Kreissl et al., 2018).

2.3 Methodology

2.3.1 Sample collection of mineralized material

Samples of mineralized (Co, Ni, Ag, As, Bi ±Cu, Pb, Zn) veins (n = 211) were collected from discard piles adjacent to 85 past-producing mine sites across the Cobalt district (Figs. 5, 6A). These were studied and analyzed to determine regional trends in metal content of the five-element veins. Additionally, drill holes from First Cobalt Corporation's (First Cobalt) 2017 and 2018 exploration programs in the South Lorrain (Keeley Frontier property) and Cobalt (Kerr Lake) areas (Fig. 2) that intersected five-element vein, Archean basement sulfide-rich interflow sedimentary rocks (Fig. 6B, C), and quartz-carbonate-base-metal sulfide veins (Fig. 6D) were also similarly sampled for study and analyses.

2.3.2 Geochemistry and QA-QC of mineralized samples

All five-element vein samples collected (n = 211) were analyzed by four-acid digestion followed by inductively coupled plasma mass spectrometry, and fire assay-atomic absorption spectroscopy (App. B) at ALS Laboratories (Sudbury, Ontario). Industry-standard QAQC protocol was followed; a total of 8 blanks (one per 30 samples) and 13 certified reference standards (one per 30 samples for Ag, Ni, Co, As, Bi; one per 50 samples for Au, Cu, Pb, Zn), and 7 duplicates (one per 30 samples) were submitted (QAQC details included in App. C). In

total, 28 QA-QC samples were submitted as part of this study and the data is tabulated in Appendix D. These data were combined with a database of samples collected by First Cobalt (n = 828); First Cobalt samples were analyzed by AGAT Laboratories and SGS Canada Inc., all of which utilized industry standard QA-QC protocols. The First Cobalt data is not included in Appendix D, but is included in presented diagrams of results and is consistent with the data from this study. As many samples had high-metal values and thus were reported as overlimit values, more than one method was used to capture their metal values. Lastly, due to multi-element laboratory analytical packages, the most appropriate assay method was assessed for each sample and this was combined into a single database (App. D).

2.3.3 Sample Characterization

A subset of samples was selected for detailed analyses including petrography, scanning electron microscopy-energy dispersive spectroscopy (SEM-EDS), and optical cathodoluminescence (CL). All work was done at the Mineral Exploration Research Centre – Isotope Geochemistry Laboratory (MERC-IGL), Sudbury, Ontario. Samples selected were representative of spatial coverage in the district with a focus on those that had multi-mineral aggregates and cross-cutting mineral relationships to ensure a consistent mineral paragenesis across the district. Polished thin sections (30 μm , n = 107) were used for mineral identification, textural studies, determination of mineral paragenesis, identify the presence of fluid inclusion assemblages, defining wallrock alteration, and detect possible growth zoning in minerals (Dong et al., 1995; Götze et al., 2001). Conventional microscopy (reflected and transmitted light) utilized an Olympus BX53M microscope. For mineral identification and CL analyses of vein quartz and carbonate, a Tescan Vega3 SEM-EDS with Tescan backscatter electron (BSE) and CL detector and a Bruker Quantax EDS system with a 60 mm² detector were used. Operating

conditions employed were: accelerating voltage 15 kV, working distance 15 mm, and beam current for spot and raster analysis ~ 1 nA and ~ 5 -10 nA for element maps. The CL imaging of quartz and carbonate used an acceleration voltage of 15 kV and beam current of ~ 1 nA.

2.3.4 In-situ Laser Ablation Inductively Coupled Plasma Mass Spectrometry (LA ICP-MS) of vein carbonates

A subset of representative polished 30 μm sections ($n = 8$) featuring multiple generations of hydrothermal vein carbonate throughout the five-element vein paragenesis were selected for in-situ LA ICP-MS analyses at the MERC-IGL. Select major and trace elements (Ca, Fe, Mg, Mn, Sr, Th, U) and rare earth element (REE) analyses were done with a Photon Machine, Analyte G2 laser ablation and Thermo iCap-TQ ICP-MS system with a Helex II, large format, two-volume ablation cell (Woodhead et al., 2007; Paton et al., 2011). Operating conditions used were a laser wavelength of 193 nm, fluence of 4 J/cm^2 , repetition rate of 6 Hz, and ablation duration of 30 s. Ablation pit depth was $\sim 15 \mu$ with an ablation rate of $\sim 0.5 \mu\text{m/s}$ and spot sizes 25 to 35 μm . Gas flow rates for He₁, He₂, Ar, and N₂ carrier gases were set to 0.525 L/min, 0.1 L/min, 0.65 L/min, and 0.006 L/min, respectively. All other analytical conditions, reference material, and data processing information are in Appendix E. Glass standards G_NIST610 and G_NIST612 were run every 4 samples. The percent difference between measured values and accepted values of each element for the standards were -19% for Mg, -11% for Mn, 103% for Fe, and all other elements were below 5%. Departure of the mean values for each element of the analyzed standards always had a percent standard deviation (% RSD) of less than 5%, except 7& for Mg, 16% for Mn, and 11% for Fe in the first batch of analyses, and 10% for Mg, 6% for Si, 9% for Fe in the second batch. The data were processed offline using the protocols of Woodhead

et al. (2007) and Paton et al. (2011). Values of U and Th are not reported because these elements fell below the limit of detection.

2.3.5 Fluid inclusion petrography and microthermometry

A subset of double-polished, 150 μm thick sections ($n = 20$) were prepared from representative vein quartz for fluid inclusion study. Petrographic study and CL imaging was used to identify inclusion types and constrain their timing of entrapment using the approach of fluid inclusion assemblages (FIA; Goldstein and Reynolds, 1994; Bodnar, 2003a). A few representative samples were selected for a preliminary microthermometric study carried out in the Fluid Inclusion Laboratory at Laurentian University, Sudbury, Ontario. Measurements were made using a Linkham THMSG 600 heating and freezing stage attached to an Olympus BX-51 petrographic microscope; the stage was operated with a computer controller unit which regulated the heating and cooling rate. The stage is calibrated with synthetic fluid inclusions: triple point of CO_2 (-56.6°C), the triple point of H_2O (0°C) and the critical point of H_2O (374°C). Details of the protocol used are given in Slater et al. (2021).

2.4 Results

2.4.1 General features of five-element veins and wallrocks

The five-element veins at Cobalt occur as narrow veins (2-3 mm to 120 cm) with textures indicating infill of extensional fractures (Fig. 6A). The vein infill consists of comb-textured quartz, native metals, arsenides, sulfarsenides, accessory sulfosalts, and base-metal sulfides encased in pale pink ferroan dolomite and clear to cloudy white, fine-grained to massive calcite (Fig. 6A, E, F). The metal and quartz-carbonate proportions of vein segments is heterogeneous between samples, but are typically high-tenor.

Alteration selvages a few centimeters thick follow vein margins (Fig. 7) and they texturally obliterate the wallrock mineralogy and former features. Although veins are hosted in different lithologies, alteration is consistent with chlorite, carbonate, actinolite, albite and minor epidote with the addition of arsenopyrite and disseminated Ni-Co-arsenides (Fig. 7). In the wallrock, plagioclase is albitized and pyroxene, biotite, and amphibole are chloritized. Chlorite is zoned with a Mg-rich core and Fe-rich rim and overall becomes more Fe-rich towards the veins. Calcite replaces plagioclase in mafic volcanic rock, as well as the fine-grained matrix and rims of lithic clasts of sedimentary rocks. Trace sericite and sulfides occasionally rim vein margins. Wallrock clasts often incorporated into the veins are angular, of variable size, and are usually chloritized and carbonate altered.

2.4.2 Composite petrography of five-element veins

There is a consistent development of mineral and textural stages in vein samples with the following paragenesis noted: (i) early vein fill of comb quartz; (ii) the five-element stage; (iii) a stage of coupled dissolution-precipitation (CDP) of early arsenides which has not been previously noted at Cobalt; (iv) a carbonate-fill stage; (v) native metals (Bi, Ag); and (vi) base-metal sulfides. These stages are described in order below.

The early vein fill consists of comb quartz (Fig. 8A) that is aligned perpendicular to the vein walls, hence it represents an extensional feature. Post-dating the quartz as vein fill is bladed actinolite, epidote, trace albite, and anhedral to acicular hematite encased in calcite crystals. Flamboyant chlorite, either as vein septa or radial reniform clusters, forms as bands or on the comb quartz.

The five-element assemblage post-dates the comb quartz and other aforementioned silicates and includes elongate rosette features cored by dendrites of native silver that are

enveloped by Ni-Co-Fe-arsenides. These features are followed by carbonate and minor silicate minerals (Fig. 8B). The dendritic native silver, a common feature in five-element settings, is attributed to disequilibrium growth related to rapid precipitation (e.g., Markl et al., 2016). Arsenides and sulfarsenides are concentrically-zoned (e.g., Figs. 8F, H, 9A), multi-mineral rims surrounding the native silver as circular- to oblong-shaped, mm- to cm-scale colloform-rosette aggregates that cluster in patches (Fig. 8C-K). The dominant Ni-Co-Fe-arsenide minerals include nickeline (abbreviated Nic; NiAs), rammelsbergite (Ram; NiAs₂), Ni-skutterudite (Ni-skutt; Ni,Co,Fe)As₃, safflorite (Saff; CoAs₂), skutterudite (Skutt; CoAs₃), and loellingite (Lo; FeAs₂), whereas sulfarsenides include gersdorffite (Ger; NiAsS), cobaltite (Cob; CoAsS), and arsenopyrite (Apy; FeAsS). That micro-spheres (a few μm) or trails of native bismuth occur within all Ni-Co-Fe arsenide minerals with no associated CDP textures suggests these droplets are primary features (Fig. 8L, M).

The CDP textures (e.g., Ruiz-Agudo et al., 2014, and references therein) are seen between concentrically-zoned arsenide phases (e.g. CDP mineral boundaries are labelled in Fig. 9B, but this texture occurs in Fig. 9A-F) which generally progress from Ni- to Co- to Fe arsenides. The earlier phases are corroded and overgrown by new minerals that are characterized by euhedral terminations, such as they occlude in cavities, and abundant pitting; both of these textures are features noted where CDP occurs (Ruiz-Agudo et al., 2014). The CDP textures are also localized to hairline fractures where fluids were focused and dissolution occurred.

Similar to the arsenide aggregates, carbonate is multi-generational and displays CDP textures between partially replaced rhombohedral dolomite or calcite with late overprinting calcite (termed calcite 1 and calcite 2 in section 2.4.9; Fig. 9G). This late calcite additionally

infills fractures and dissolution pits of vein and wallrock material. Dolomite always precedes calcite if both carbonate minerals are present.

The late minerals include anhedral to sub-rounded, blebby, or ribbon-like native silver (Fig. 6E) and bismuth (Fig. 9H), base-metal sulfides (i.e. chalcopyrite, sphalerite, galena, bornite, acanthite, bismuthinite; Fig. 9I, J), and rare sulfosalts. These phases infill fractures within jigsaw breccia-textured, and partially dissolved, arsenide aggregates and along late fractures in vein carbonate. This is textural evidence for the late-stage remobilization of native metals and overprint of sulfides.

2.4.3 Mineral paragenesis of five-element veins

The above observations are used to develop the paragenetic stages, which is correlated with the numbering sequence below in brackets corresponds to that of the schematic vein-assemblage diagram in Figure 10. In sequential order, the paragenetic stages are as follows:

- *Barren stage* (1): Euhedral comb quartz fills open space with subsequent chlorite, epidote, actinolite, and rare pyrite.
- *Five-element stage* (2, 3): The main mineralization for native silver as dendritic crystals rimmed by Ni-Co-Fe-arsenides (the “arsenide window”), along with ferroan dolomite or calcite. Arsenides occurs as colloform and rosette aggregates and may occur with (e.g. 2) or without (e.g. 3) a native-metal component. There is a general elemental progression of Ni- to Co- to Fe-arsenide solid solution involving multiple superimposed coupled dissolution-precipitation replacement fronts within the arsenide aggregates.
- *Ni-Co-Fe sulfarsenide and Ag-As-Sb sulfosalt stage* (4, 5): CDP replacement of the arsenide phases (e.g. 4) accompanied with CDP replacement of early carbonate by late calcite (e.g. 5).

- *Native metal (Ag, Bi) remobilization (6)*: Infill of native bismuth and silver or related phases with varying amounts of S (i.e. bismuthinite and acanthite compositions) into micro-fractures and jigsaw brecciation of pre-existing vein phases;
- *Sulfide stage (7)*: Overprinting sulfide event (i.e., chalcopyrite, sphalerite, bornite, galena, and minor pyrrhotite pyrite, and cubanite) accompanied by calcite, quartz, and minor fluorite and barite.

It is noted that the relative timing between remobilization of native metals (6) and sulfide precipitation (7) is uncertain and that these stages may overlap.

2.4.4 Mineral chemistry of five-element vein assemblage

The compositions of the five-element vein assemblages are presented in Figures 11 – 13, with representative data in Tables 2 – 4 and additional data in Appendix F.

Rosette features cored by dendritic native silver and with multi-phase arsenide rims analysed in raster mode (Fig. 11B, C) have a consistent bulk composition of approximately 59.8 wt. % (59.1 at. %) As, 17.3 wt. % (11.8 at. %) Ag, 14.8 wt. % (18.6 at. %) Co, 4.0 wt. % (5.2 at. %) Fe, 1.5 wt. % (0.9 at. %) Sb, 1.2 wt. % (1.5 at. %) Ni, and 1.0 wt. % (2.2 at. %) S (Fig. 11B; Table 2). Raster analysis of the dendritic native silver cores are consistent with an average of 92.6 wt. % (91.0 at. %) Ag, 4.7 wt. % (4.1 at. %) Sb, and 0.5 wt. % (1.6 at. %) S (Fig. 11C; Table 2). These dendritic Ag-Sb cores are surrounded by annuli of small Ag-Sb inclusions of irregular shape having identical composition (Fig. 11D). At high magnification there are cusped interfaces with dihedral crystal angles between the Ag-Sb dendrites and skutterudite (Fig. 11D). The outward progression of the arsenide mineral sequence gradually transitions from skutterudite to safflorite (Fig. 11E). Additionally, some arsenide aggregates are cored by dissolution pits

infilled by carbonate, which assume the same relict shape as the dendritic native silver cores seen in other samples (Fig. 11F).

Ternary plots (As-S-Ni-Co-Fe) of the arsenide and sulfarsenide minerals (Fig. 12) indicate that data fall between end-member arsenide and sulfarsenide minerals. Thus, the minerals have extensive and variable nonstoichiometric substitution among Ni-Co-Fe, as well as varying amounts of S incorporated. Ag (0.1 wt. % detection limit) was not detected in the arsenide or sulfarsenide phases. Furthermore, ternary plots (Ag-As-Sb-S) of the Ag-bearing minerals in Figure 13 indicate that remobilized Ag (as well as Bi) can be pure or accompanied with ranging proportions of sulfur.

2.4.5 Chemistry of five-element vein samples: Regional zoning and implications for mineralogy

The analytical data for five-element vein samples were combined with that of First Cobalt and plotted spatially to identify potential regional trends in metal zonation. Any samples that were over-limit or under-limit were assigned the over-limit or under-limit detection values, respectfully, for plotting purposes.

The ranges for elements of interest are presented in Table 5 (see all data in App. D), which show large ranges from high values to below the detection limits for different elements. Percentile groups for each element (<P₇₅, P₇₆₋₉₀, P₉₁₋₉₅, P₉₆₋₉₉, and >P₉₉) and element ratios (e.g. Ag/Co; <P₅, P₅₋₁₀, P₁₁₋₅₀, P₅₁₋₉₀, P₉₁₋₉₅, >P₉₅) were geospatially referenced and plotted in ArcMap® (Fig. 14). Figure 14 shows a subset of representative element-ratio plots for the Cobalt subarea with Figure 14B and C showing maps of Ni/Ag and Co/Ag percentile ratio values, respectfully. In both cases, the distribution of percentile ratio values indicate that samples in the central regions of the sample clusters are Ag-dominant over Ni and Co (red symbols). Peripheral to the

Ag-dominant area, Ni (Fig. 14B) and Co (Fig. 14C) dominant samples are more common (blue symbols). Figure 14D shows a map of percentiles of Co/Ni in the same region, which suggests that Co-dominated samples (blue symbols) are ubiquitous, but the few Ni-dominated samples (red symbols) are noted to be proximal to Archean mafic volcanic inliers. These percentile groupings demonstrate that, in Cobalt at least, a metal zoning with a Ag-rich mineralization core and Ni- and Co-rich peripheral region exists.

Detailed assessment of metal distribution with respect to host-rock types indicates no preferential host lithology for the high Ag and Co percentiles. However, there is a preference for high Ag at localities having high vein densities, such as at Kerr Lake or Cobalt Lake (Fig. 14A, B), and generally agrees with the locations of the highest yielding historical Ag-producing mines (Sergiades, 1968; MDI, Ontario Geologic Survey, 2019; App. G). These high-vein densities are often hosted in the Huronian sedimentary rock proximal to outcropping of the Archean interflow sedimentary rocks, whereby erosion of the overlying Huronian rocks is inferred. In contrast, the highest percentiles for Ni are from samples hosted in the Archean mafic volcanic rocks, with the smallest percentile groupings from samples hosted in the Nipissing gabbro.

The spatial distribution pattern of Bi most closely mimics that of Co, and Sb most closely mimics that of Ag (App. G). Arsenic is ubiquitous throughout the district, whereas Zn and Pb have similar distributions and differ from Cu. However, the spatial distributions of these base metals differ greatly from that of Ag, Ni, Co, As, Bi, or Sb (App. G).

Further assessment of the aforementioned bulk sample assays included plotting it as atomic proportion in binary and ternary diagrams for various elemental combinations (Ag, Co, Ni, Bi, As, S, (As+S), Sb, Cu, Pb, Zn, Mo) to evaluate the dominant mineralogy present in samples and hence the studies areas. Grouping of minerals followed the paragenetic mineral

sequence previously noted: native silver to Ni-arsenides to Co-arsenides to base-metal sulfides. Complex sulfosalts were not included in the mineral groupings, as these phases are overall rare and do not dominate the veins.

The following summarizes the procedure followed to group the samples into major mineral groupings:

1. Highly anomalous Ag-rich samples were attributed as Ag samples given it is the dominant element compared to the other metals in the assemblage (i.e. Co, Ni, Bi, etc.).
2. The Ag-rich outliers were filtered out and the remaining data were plotted in the As:Ni:Co ternary. All samples below ~45% As were attributed to being sulfide-dominant as they plot outside of arsenide mineral space.
3. For the binary Co:Ni plot, all points above the 1:1 line were categorized as Ni-dominated arsenide and points below the 1:1 line as Co-dominated arsenide.
4. The Ni-dominated arsenide points were plotted in the binary Ni:As as to define “NiAs”, “NiAs₂”, and “NiAs₃”, grouped according to slopes of 1:1 – 1:1.5, 1:1.5 – 1:2.5, and >1:2.5, respectfully.
5. The Co-dominated arsenide points were plotted in the binary Co:As to define “CoAs”, “CoAs₂”, and “CoAs₃”, grouped according to slopes of 1:1 – 1:1.5, 1:1.5 – 1:2.5, and >1:2.5, respectfully.
6. All Ni-Co-arsenide data points were plotted in As:Ni:Co ternary space, where points with >90% As normalized atomic proportion were grouped as “As”.
7. The remaining sulfide-dominated samples were grouped as “Cu-sulfide-dominated”, “sphalerite-dominated”, and “galena-dominated”, dependent on which of these metals (Cu, Zn, Pb, respectfully) was most abundant in the remaining samples.

8. All mineral groupings were geospatially referenced in ArcMap® overtop of geology.

This mineral groupings approach for Cobalt (Fig. 15; see additional figures in App. G) shows: (i) the Ag-dominated samples are located in pockets in the center of the Cobalt subarea (Fig. 15B); (ii) the Ni-rich samples (orange and green circles in Fig. 15C) occur along the periphery of the Cobalt subarea; (iii) the Co-rich samples (purple and blue circles in Fig. 15D) are much more abundant than the Ni-rich samples; (iv) the CoAs_3 -dominated samples (dark blue circles in Fig. 15D) occur mostly in the dashed areas, which generally correlate to Ag-dominated samples (Fig. 15B); and (v) the CoAs- (purple circles in Fig. 15D) and CoAs_2 -dominated (light blue circles) samples are peripheral to the CoAs_3 distribution, in the same areas as the Ni-dominated samples. Examination of the spatial distribution also shows that there is no apparent lithological preference or spatial trends for the distribution of monarsenides versus diarsenides versus trisarsenides. However, the Co-trisarsenide (skutterudite) is the most abundant mineral, and thus ubiquitous, whereas the CoAs (monarsenide) is rare and therefore not mineralogically favored. The Ni- monarsenide (nickeline) and diarsenide (rammelsbergite) are more abundant than the triarsenide (Ni-skutterudite).

These plots also show potential associations among mineral groupings and the type of host lithology. The main vein host environments are noted: (i) Huronian and Archean mafic volcanic-Huronian sedimentary rocks (i.e. close to the regional unconformity); (ii) Archean mafic volcanic; and (iii) veins that pinch out into the Nipissing gabbro. There is an apparent preference of Ni-arsenide minerals to the Archean mafic volcanic basement inliers (Fig. 15C), whereas there is no apparent host lithology preference for native Ag (Fig. 15B) or the Co-arsenides (Fig. 15D). Ag does occur in gabbro-hosted veins, however, Ag is more abundant in areas of higher vein densities, which tend to be hosted in the Archean basement or Huronian

sedimentary rock (e.g. Fig. 15B, Kerr Lake, Cobalt Lake, and NE corner of Cobalt, in the dashed areas).

Detailed evaluation of mineralized areas indicate local variations in metal distribution (maps in App. G). Areas scrutinized include the Kerr, Cart, Cobalt, and Crosswise Lakes, and Southern Cobalt region, and the Woods and Watson veins in the Keeley Frontier property in the South Lorrain township (Fig. 2). The subtle variation in metals seen at one locality is not consistent at the local scale across other veins, thus metal distribution is locally heterogeneous.

The use of the ternary diagrams of elements provides the means to assess the vein assay data in relation to stoichiometric minerals. Results reveal that the vein assay data falls between mixtures of end-member arsenide minerals (Fig. 16A-F; Table 6). For example, in the As-Ni-Co and As+S-Ni-Co ternaries (Fig. 16B-D), vein assay data scatter between the Ni- and Co-arsenides with the point density indicating Co mineralogy dominates. The most abundant mineral is the triarsenide skutterudite (CoAs_3), which is confirmed during petrographic study of the widely-dispersed sub-set of samples. In contrast, the monarsenide nickeline (NiAs) was the most common Ni-arsenide. Figure 16C and 16D (Ni-As-S and Co-As-S ternaries, respectively) show the Ni- and Co-arsenides contain varying amounts of non-stoichiometric substitution of S. Figure 16F (Ag-Ni-Co ternary) demonstrates Ni- and Co-arsenide dominant samples that do not contain high levels of Ag.

Binary plots of elements (Co-Ni-As-Bi-Sb) in log-log space (Fig. 17) all show strong covariance. For example, in Figure 17A, a plot of As versus Ni, demonstrates that Ni-arsenide data points fall along the mineral trajectories, whereby coloured lines represent Ni-arsenide mineral trajectories. This linear trend is seen in all the binary plots in Figure 17, meaning the ratio between the binary relationships is consistent across the concentration ranges for the

samples, the latter reflecting the abundance of the vein gangue (i.e. quartz and carbonate). As well, the Co:Ni ratio (Fig. 17C) remains uniform, especially when considering the number of widely-distributed samples. In contrast, Ag shows a sporadic, or scattered, distribution versus Co-Ni-As-Bi (Fig. 18). Ag always occurs with Co-Ni-Bi-As-Sb, however these same elements are not always accompanied by Ag. Additionally, rare enrichment of Hg is associated with Ag-rich samples.

Concentrations of Cu, Zn, and Pb do not correlate with any combination of Ag-Co-Ni-Bi-As-Sb (Fig. 19 with additional plots in App. G). Despite the large data scatter, these base metals show a possible bimodal distribution when plotted against Ag, Co, Ni, Bi, As (e.g. Fig. 19E, H), and Sb which would suggest two styles of mineralization: the overprinting of late stage Cu-Zn-Pb sulfide mineralization on the five-element assemblage versus base-metal sulfides in the wallrock. Notably, there is slightly tighter clustering for Cu-Zn-Pb when plotted against each other (Fig. 19C, F, I), which confirms their noted close association.

2.4.6 Cathodoluminescence imaging of vein quartz and carbonate

Cathodoluminescence imaging of the early stage of comb quartz reveals two types of quartz, as distinguished by differing luminescence intensities (Fig. 20A). The earlier quartz has a dull CL, but with broad bands of variable CL (i.e. a zoning), as do other similar quartz grains that extend further outwards from the vein margin. In contrast to this quartz, the later quartz, which nucleated on the former and in general displays a feathery or plumose texture, has a strong CL response (Fig. 20A-C). This quartz shows two patterns which are seen in quartz that is cut both subparallel and perpendicular to the *c*-axis. In each case, there is an oscillatory zoning seen as alternating dark and light CL quartz which outlines growth zones and this is then cut by a cobweb- or grid-like pattern of variable luminescence in quartz (Fig. 20D, E; e.g. Rusk and

Reed, 2002). Therefore, in addition to the euhedral zoned cores and outer plumose-textured quartz types, there is overprinting of dark CL region that appears to be related to micro-shearing features.

Dolomite and calcite are the main gangue phases in the five-element veins. When both minerals are present, dolomite always precedes calcite, indicated by CDP textures between partially replaced euhedral dolomite overprinted by the calcite. CL images collected on several samples indicate the same sequence and features, this being that the dolomite commonly has a euhedral rhombohedra habit, with growth zoning interpreted from CL patterns of a patchy core to dark rim (Fig. 20F). It is common for the dolomite to be variably replaced by later calcite, which in CL lacks apparent zoning.

2.4.7 Chemistry of vein carbonates

Representative samples of vein dolomite and calcite (two generations, termed calcite 1 and calcite 2) were analyzed for major, trace, and REE contents with sampled locations based on petrography and CL imaging. Representative data are presented in Tables 7 and 8 and the complete data are given in Appendix E. The data are summarized in Figures 21 and 22.

The average Ca, Mg, Fe, and Mn contents of zoned dolomite range from 16.45-28.87 wt. %, 8.38-12.27 wt. %, 0.40-1.40 wt. %, and 0.08-0.72 wt. %, respectively. The same values for calcite range from 29.30-53.88 wt. %, 0.01-0.6 wt. %, 0.06-0.63 wt. %, and 0.30-1.35 wt. %, respectively. As seen in the Ca-Mg-(Mn+Fe) ternaries (Fig. 21A, B), calcite has <2-3 at. % Mg and <5 at. % Fe+Mn, with calcite 1 more enriched in Fe+Mn. For dolomite, the plots indicate Ca>Mg and many samples have elevated Fe contents (ferroan dolomite). The Fe content of dolomite is higher and more variable than in calcite, whereas Mn content is similar. The average Sr values range from 23 to 71 ppm for dolomite and 52.8 to 232.4 ppm for calcite. For the

dolomite, no systematic chemical zoning was noted despite growth zoning seen during CL imaging.

Due to the preferential incorporation of some redox sensitive elements into carbonate (e.g., Fe Mn), in addition to Sr (Ichikuni, 1973; Shannon, 1976; Bau, 1991), Fe, Mn, and Sr are plotted as a function of Eu anomaly ($\text{Eu}/\text{Eu}^* = 0.0014\text{-}0.76$ for all samples) in Figure 21C – E. The plots show that, in general, there is little elemental enrichment of Fe and Sr with respect to Eu/Eu^* , but for Mn contents are higher for Eu anomaly as $>0.1\text{-}0.2$ in dolomite and calcite 1.

The chondrite normalized (CN) REE patterns for the different carbonates are summarized in Figure 22. In general, there is an overlap of the data in terms of the $\sum\text{REE}$ – dolomite has 22-26 ppm, calcite 1 0.36-2914 ppm and calcite 2 3.66-870 ppm $\sum\text{REE}$. Comparison of the REE patterns for the different carbonate types indicates three repeating REE patterns as summarized below:

- i. A dominant pattern with subtle or no LREE enrichment relative to the HREE with variable negative Eu anomalies in both dolomite and calcite (e.g., Fig.22A, B). These patterns can have a large range in CN values, but are always >10 . In many cases these patterns give way to a flattening of LREEs as the $\sum\text{REEs}$ decrease.
- ii. A few calcites are strongly enriched in LREE over the HREEs (Fig. 22E, F).
- iii. A pronounced HREE enrichment over the LREEs and seen in both calcite types (Fig. 22 C, D, E, J), but only for samples with low $\sum\text{REEs}$ and at $\text{CN} < 1$.
- iv. A listric-shaped pattern with relative depletion of the middle REE and a negative Eu anomaly (Fig. 22 F, I); again this is for both dolomite and calcite havng lower $\sum\text{REEs}$.
- v. A few samples show a pronounced positive Ho anomaly, but only where the CN value are <10 (Fig. 22E, F, I, J).

In general, the patterns from samples which have the highest REE content appear similar, but the magnitude of LREE enrichment and negative Eu anomalies vary slightly ($\text{Eu}/\text{Eu}^* = 0.0014\text{-}0.76$). Most calcite samples show an incremental decrease in REE concentration, up to three or four orders of magnitude, with very little overall change in the REE profile (e.g. Fig. 22B, C, D, F, G, H), whereas dolomite shows lesser changes in REE concentrations. As the ΣREEs decrease, the HREE patterns remain roughly subparallel, but at lower ΣREE the LREE become depleted to $<\text{HREE}$ (Fig. 22C, D). In contrast, a few calcite samples, both types 1 and 2, have low ΣREEs with the CN profiles <10 .

There is no systematic trend of REE enrichment or depletion from core to rim or vice versa for either dolomite or calcite. Additionally, a calcite generation in a particular sample can have more than one pattern in rare cases (Fig. 22D).

2.4.8 Fluid inclusion studies of five-element veins from the Cobalt district

Select five-element vein samples and base-metal rich footwall vein samples containing quartz and carbonate (e.g. Fig. 6D) were studied for fluid inclusions and samples were chosen based on where well-preserved populations (i.e. FIAs; Goldstein and Reynolds, 1994) and types of inclusions – primary (P), secondary (S), pseudosecondary (PS), and indeterminate (I) (see Bodnar, 2003a) – could be identified. The inclusion types are summarized in Table 9 and representative inclusions, as seen at room temperature (20-25°C), are shown in Figure 23 and schematically summarized in Figure 24. Six types of inclusions seen in the five-element vein samples, the main focus of this study, are described below.

Type i L-V-Halite (H) inclusions (Fig. 23B, C) are $<5\ \mu\text{m}$ and regular to irregular shaped. They are abundant and occur as P- and I-types inundating the cores of comb quartz, but also as S-type cutting comb quartz. Importantly, they do not coexist with other inclusion types, such as

V-rich if fluid unmixing had occurred. Locally, L-H inclusions occur with L-V-H inclusions but are attributed to necking of the latter.

Type ii L-V-Solids(S) \pm H inclusions are $<7 \mu\text{m}$ and of irregular shape (Fig. 23D, E), which may also include decrepitated inclusions. Less abundant than type i L-V-H inclusions, these I- and S-types also occur coring comb quartz, but are not seen as part of the type i FIA, although they can host H. Based on petrographic features (i.e. high birefringence), some solids are likely mica (e.g. sericite) and are considered to be accidentally trapped grains versus daughter minerals.

Type iii L-V ($<20\%$ V) inclusions are $<5 \mu\text{m}$ and regular in shape (Fig. 23F, G). They occur as PS-type along healed fractures cutting the cores of comb quartz, but also as I-type towards the margins of comb quartz.

Type iv L-V (40% V) inclusions, distinguished from type iii based on a large V %, are $<7 \mu\text{m}$ and of regular to irregular shape (Fig. 23H, I). As with type iii, they occur PS- and I-types in comb quartz, but also occur as P-type of $<30 \mu\text{m}$ on the margins of euhedral calcite grains. In the latter, they are accompanied by V-type inclusions (Fig. 23J, K). Rare, monophasic L-type inclusions associated with types iii and iv are attributed to necking.

Type v V-type inclusions can include both V-only and also V-rich, the latter having a thin rim of L (Fig. 23L-N). These inclusions are $<5 \mu\text{m}$ and have regular shapes. They occur as P- and I-types in coring comb quartz cores and also in quartz entrained in the arsenides (Fig. 23L, M), S-types cutting comb quartz (Fig. 23N), and as P type of $<30 \mu\text{m}$ on the margins of euhedral calcite coexisting with type iv inclusions (see above). Some type v inclusions define trails of radial, elongate-shaped decrepitated inclusions, which resemble textures seen in epithermal-type

quartz generally inferred to be trapped during rapid quartz growth (e.g, Dong et al., 1995; Sander and Black, 1998).

The last inclusion type, type vi, is defined based on shape rather than phases present and are referred to as decrepitates. These are inclusions whose shapes were substantially modified post entrapment (Fig. 23 O, P). Such inclusions are abundant and tend to be found on the margins of comb quartz grains. These inclusions are large, ranging from around 5-30 μm , with the majority containing mainly V, and fewer containing L and solids.

The base-metal vein samples studied also contained the same populations of inclusions as noted above. The only noted difference was that for the type v inclusions more L-phase was present (to 20-40%).

Microthermometric data collected to date was restricted to the base-metal veins (e.g. Fig. 23Q-S), as the very low amount of gangue in the five-element veins compromised most of the samples in regards to dismounting quartz and carbonate for such studies. Hence, at present only data for the base-metal veins are summarized and since a more detailed study is to be followed, only a brief summary of data acquired is provided here. For these samples, the following is noted for inclusion type i, iv and v. For type i L-V-H type inclusions the $T_{\text{h}}(\text{H})$ values of 168 to 280°C equate to salinities of 30.4 to 36.7 wt.% equiv. NaCl using tables in Bodnar (2003b). The low first melting (T_{fm}) or eutectic temperatures of these inclusions indicate the presence of CaCl_2 . These inclusions homogenized over a broad range from 170 to 295°C, but smaller ranges of <10-20°C are noted for an FIA. The homogenization behavior was of three types, as follows L-V-H \rightarrow L-V \rightarrow L, or L-H \rightarrow L, or just to L. For type iv L-V inclusions, $T_{\text{m}}(\text{CO}_2)$ was -62.3 to -64.4°C, which indicates the presence of other dissolved gases such as CH_4 and/or N_2 . The $T_{\text{h}}(\text{CO}_2)$ for the carbonic phase was to the liquid and ranged between -17.8 to +7.8°C. Using the

$T_m(\text{CO}_2)$ versus $T_h(\text{CO}_2)$ plot of Mernagh et al. (2004) suggests up to 20-30 mol % CH_4 mixed in the CO_2 component of these inclusions. That T_{fm} for these inclusions indicate that CaCl_2 is present in solution and that hydrohalite was the last phase to melt indicates salinities between 23 and 26 wt. % equiv. NaCl (Roedder, 1984). Lastly, for the type v V-rich inclusions (Fig. 23Q-S), these showed low homogenization temperatures, always the L, from -120 to -106°C . This type of phase behavior suggests a mixed CO_2 - CH_4 system with >60 mol % CH_4 and, in addition, N_2 may also be present (Van den Kerkhof and Thiéry, 2001).

2.5 Discussion

2.5.1 Regional metal zonation and implications

This study has shown that there is a metal zonation in the Cobalt district specifically with a Ag-dominated zone compared to a peripheral Ni and Co enrichment and, furthermore, that high Ni is spatially associated with exposures of Archean mafic volcanic rocks. This metal zonation suggests therefore a broad thermo- and/or chemical (e.g. redox) gradient generated by fluids and/or a host lithology control. Alternatively, the zoning might reflect a late-stage mobilization of Ag, as noted in many samples, and/or an influx of Ag and its superimposition on an existing Co-Ni enrichment. This in turn implies the localization of the late Ag was controlled by an event that preferentially focused it into effective traps (i.e. zones of high fracture density), rather than by a chemical or thermal gradient during the earlier mineralizing event. The amount of remobilized of Ag, however, is difficult to quantify and for this reason a broad thermo- or physio-chemical gradient is currently preferred as a more likely a cause for the metal zonation.

The local association of high Ni in five-element veins hosted by Archean basement rocks could be more apparent than real due to its low overall abundance in the five-element system. Additionally, the restricted amount of sampling limits statistical relevance of the Ni distribution.

Thus, the relative enrichment of Ni is possibly related to a significant amount of sulfide (e.g. pyrrhotite) locally derived from the Archean interflow sedimentary rocks and/or perhaps an initially high content in mafic volcanic rocks (i.e. original enrichment in olivine). Additionally, if metals originate from a stratigraphically lower Archean basement reservoir, the veins could also be vertically zoned with Ni more concentrated proximal to the source, presumably now as nickeline, due to a lower relative mobility than other elements. In this context, a greater relative mobility of Co would account for its' more ubiquitous distribution compared to Ni.

The Cobalt subarea metal distribution maps (Figs. 14, 15) reveal the most important feature of high-metal contents are lithological contacts between the Archean basement and Nipissing gabbro. In contrast, the many kilometers of contact between the Nipissing gabbro and Huronian sedimentary rocks, and lesser so Lorrain granite, across the area appears not equate to areas of higher metal endowment. Instead, Archean basement inliers are the most relevant for high metal values and, within this, it is the interflow sedimentary rocks that are the most relevant in context of plausible metal source. The latter includes sulfide-rich intervals with high Ni-Co in addition to other Cobalt relevant elements (Ag, Bi, Sb) (unpublished data, First Cobalt Corp.). However, a further detailed study of this potential metal reservoir is needed to better understand and further explore this working hypothesis.

2.5.2 Geochemical and petrographic features of the five-element veins

2.5.2.1 *Covariation of Co-Ni-As-Bi-Sb in vein samples*

The strong covariation of Co-Ni-As-Bi-Sb based on multi-element analysis of vein samples indicates these elements are coupled and, based on petrography and SEM-EDS studies, occur in various Ni-Co-arsenide and sulfarsenide phases, but dominated by nickeline, safflorite, skutterudite, gersdorffite, and cobaltite (Figs. 8, 9). As for Bi and Sb, the former occurs as

amoeboid-shaped micro-inclusions (few μm) in arsenide aggregates versus elemental substitutions in arsenides, whereas Sb occurs as: (i) Ag-Sb alloys (i.e. allargentum, dyscasite, stephanite: Petruk et al., 1971b); and (ii) a substitution for As in Ni-Co-Fe-antimonides intergrown with arsenides (Petruk, 1971c; Petruk et al., 1971a). The coherency of metal ratios in various binary and ternary plots, regardless of extensive coupled dissolution-precipitation (CDP) processes, indicates subsequent modification of the primary mineralogy did not modify metal tenor or elemental ratios. Thus, the arsenide-to-sulfarsenide transition in the paragenesis reflects sulfur addition without apparent metal mobilization. In contrast, the noted scatter of Ag in metal plots (i.e. Co, Ni, As, and Bi) suggests it behaved independent of these elements, as is indicated by its dominance as native silver versus substitution into arsenide or sulfarsenide phases. Furthermore, the decoupling of Ag from Co-Ni-arsenides reflects its late remobilization and separation from other minerals, as supported from petrographic and SEM-EDS observation (e.g. Fig. 11F).

2.5.2.2 *Wallrock alteration and early vein fill by comb quartz*

The lack of extensive (i.e. $>\text{cm}$ scale) wallrock alteration with complementary high-ore tenor (i.e. massive arsenide-sulfarsenide vein fill) relative to other hydrothermal environments (e.g. porphyry vein and skarns, epithermal, orogenic gold) has long been noted for five-element vein settings at Cobalt and in general (e.g., Jambor, 1971d; Appleyard, 1980; Andrews et al., 1986). The narrow, intensely developed propylitic-type alteration halos infer localized high fluid:rock interaction and related disequilibria with limited fluid ingress distal to the vein margins. This alteration is interpreted as early, pre-vein stage which was succeeded, in most but not all cases, by comb quartz that effectively isolated the wallrock from the fluids; micro-fragments of altered wallrock in the veins supports this interpretation. This isolation of the

wallrock from the vein fluid also infers the wallrock did not serve as a significant geochemical buffer to the fluids.

The abrupt transition from fracture-focused fluid flux and related alteration to dilatancy and through flow is marked by formation of elongate, high-aspect comb quartz that records vein extension with little shear component. CL imaging of this quartz highlights a variety of zoning patterns that includes both broad light and dark luminescence with normal (i.e. bright-to-dark from core-to-rim) and the reverse zoning, and also fine-scale oscillatory zoning. Such features are typical for hydrothermal quartz in high-crustal deposit settings (e.g. porphyry-epithermal) and reflect cyclicity of temperature and/or fluid chemistry. As we lack such data (e.g. Ti content), a more conclusive statement is not possible. Notably, other textures that might be expected in systems wherein rapid growth of quartz occurred and where silica supersaturation might be expected (e.g. colloform, moss, jigsaw, and lattice; Moncada et al. 2012), are lacking. Thus, whereas growth of comb quartz was favoured, evidently conditions did not induce silica saturation, such as inferred in settings where fluid unmixing occurs (Moncada et al. 2012, 2017).

2.5.2.3 Primary textures of native silver and Co-arsenides

The implications of dendritic-textured native silver (Figs. 6E, F, 8B, 11A-C) for vein and deposit genesis has not been accounted for in previous models at Cobalt. As with others (e.g. Petruk, 1971b; Marshall, 2008), this study has also noted the native silver dendrites coring rosettes or cruciform features surrounded by Co (\pm Ni) arsenide assemblages. In addition, we also note the presence of native silver as angular-shaped phases in arsenides that define an annulus about the native silver dendrites (Fig. 11C, D). The native silver dendrites are also noted to have cusped interfaces with primary skutterudite which suggest wetting surfaces (Fig. 11C, D), a feature not highlighted in earlier studies. Furthermore, the native silver is generally

compositionally uniform with about 4 wt. % Sb, although up to 8 wt. % of both Sb and Hg are reported by others (see Marshall, 2008). Additionally, we note the presence of native bismuth in the surround Co-arsenides, as have others (e.g. Petruk, 1971b; Marshall, 2008).

The formation of dendrite-textures are generally interpreted to reflect far-from-equilibrium conditions and are attributed to kinetically-controlled, unimpeded rapid growth, as seen in many controlled experimental studies of silicate systems (e.g. London, 2009; Maneta and Baker, 2014; Sirbescu et al. 2017). That the native silver dendrites from Cobalt form spheroidal and curvilinear versus planar interfaces also suggests they represent the boundary between former coexisting melts. Importantly, the textures persevered in the Ag-rich Cobalt ores are identical to those produced under controlled laboratory conditions involving the partial melting and subsequent solidification via quenching of sulfide mixtures (Pb-Zn-Fe-Sb-Cu-Ag-S-As; see Fig. 3C in Mavrogenes et al., 2013). Similar textures have been noted in many studies of natural settings where low melting-point chalcophile elements (LMCE) are involved in a variety of base- and precious-metal deposits (e.g. Frost et al., 2002; Tomkins et al., 2007; Mavrogenes et al., 2013; and references therein) and considered as a means to mobilize and upgrade a variety metals (Frost et al., 2002; Tomkins and Mavrogenes, 2002; Tomkins et al., 2004; Ciobanu et al., 2006; Tooth et al., 2008; Acosta-Gongora et al., 2015; Biagioni et al., 2020).

The composite native silver rosettes and surrounding Co-arsenide phases are considered to have originally been a single homogeneous melt (Ag-Co-Bi-As-Ni-Sb±Hg; Table 2) that coexisted with saline aqueous fluids, now preserved as type i L-V-H inclusions, that formed the early silicate (i.e. comb quartz) and later massive carbonate infill and arsenide-sulfarsenide veins. Importantly, this model for the rosette features differ from that of earlier suggestions, in particular of Marshall (2008), that specifically refers to the small trails of native silver inclusions

that branch off from silver veins cutting the earlier assemblages and lining healed planes in quartz with coexisting saline fluid inclusions (L-V-H). We note here in particular how the native silver dendrites differ from the equivalent in native gold from epithermal settings where it is in contact with gangue phases (e.g. Saunders and Burke, 2017; Sanders et al., 2008). This suggests therefore the native silver is intimately related to the arsenides and favours a melt origin. The generation of this melt is later discussed and here we further explore its solidification.

Formation of the consistently observed sequence from rim-to-core of safflorite, skutterudite to native silver from an inferred sulfide melt is shown schematically in Figure 25A and interpreted in two ways. The melt may have unmixed upon cooling following on the analogue experiments of Mavrogenes et al. (2013) to generate coexisting Ag-Sb±Hg and Co(-Ni) arsenide melts. Whereas the former melt gave rise to the native silver dendrites, the latter crystallized to the two noted Co-arsenide phases. Alternatively, following on the model of Tomkins et al. (2007), the native silver may have been the residual product of the fractionation of the initial melt (i.e. formation of Co-arsenides) with related enrichment of Sb±Bi±Hg lowering its point of solidification of the Ag-rich melt. Regardless of the model, the cusped interfaces require the native silver to have at one time been a melt. Importantly, the common presence of the noted rosette textures and their uniform mineralogy and chemistry in vein material from the Cobalt district suggests the unmixing of an original metal melt was a district-scale phenomenon.

The temperature of vein formation at Cobalt has been estimated at 290-350°C based on fluid inclusions, however the inclusions are hosted in phases that post-date the rosette features (Marshall et al., 1993) and is thus taken as a minimum temperature for their formation. The effect of LMCE is to substantially lower the temperature at which sulfide and arsenide melts form and by inference also for the residual melts that are suggested to have become enriched in

Bi-Sb-Hg (Tomkins et al., 2007; Tooth et al., 2008, 2011). Although the same melt compositions discussed here have not been quantitatively modelled in the latter studies (i.e. Co-Ni-As), we do note that for the Ag-Sb-Hg system coexisting with aqueous salts, the eutectic temperature is around 350°C (Mavrogenes and Bodnar, 1994; Wykes and Mavrogenes, 2005), for the Ag-Bi system, the eutectic is 262°C (Hansen and Anderko, 1958), and for Ag-Sb mixtures the eutectic can be as low as about 500°C (see summary in Marshall, 2008). Thus, while it remains to be fully explored, we suggest that enrichment of the original bulk metal assemblage of Co-Ni-As-Ag-Bi-Sb enabled it to exist as a melt, the evolution of which generated the native silver dendrites.

2.5.3 Oxidation controls on the five-element vein paragenesis

The paragenesis of the native silver-arsenide-sulfarsenide assemblages is considered to reflect the chemical evolution of the system from an initial Co-Ni-arsenide stage with subsequent superimposed Co-Ni-sulfarsenides related to fluid-mediated coupled dissolution-precipitation (CDP) processes, and then later base-metal sulfides. The role of replacement textures has not previously been recognized at Cobalt, but are documented for other five-element settings (e.g. Fanlo et al., 2004; Kiefer et al., 2017; Kreissl et al., 2018). The elements in five-element veins are redox-sensitive; thus, when reduced the native metals and arsenide phases are more stable compared to their respective oxidized aqueous species. Also relevant is the variable relative oxidation states of the five elements in the assemblages, in particular Ni versus Co and As versus S. The following discussion is based on reference to the earlier schematic paragenesis in Figure 10 and a more detailed one in Figure 25 that shows representative paragenetic mineral progressions with CDP mineral fronts and associated elemental valence states (Ni, Co, Fe, As, and S).

The presence of nickeline as the first arsenide phase (Fig. 25B) was likely favoured due to the reduced nature of the ore system that stabilized As^{2-} , which then coupled with Ni^{2+} to generate this early phase. The lack of a stable Co-arsenide phase precluded early Co mineralization even though the Cobalt district is much enriched in Co over Ni, as the vein samples in Figures 8 and 9 show, as well as the literature (e.g. Petruk, 1971b). However, subsequent formation of safflorite and Ni-skutterudite with rammelsbergite reflects oxidation of As (from As^{2-} to As^{1-}) and formation of diarsenide phases, whereas the appearance of skutterudite marks the stability of Co^{3+} and formation of triarsenides (e.g. Fig. 25B, C). The formation of the Ni-diarsenides may also have included part Ni released from the earlier nickeline as it locally shows replacement textures as it is overgrown by the latter phases (Fig. 25B). Thus, the paragenesis can simply be related to the progressive oxidation of the system in terms of both the metals and arsenic species. Furthermore, formation of the rosette features noted above and related fractionation of the Co-Ni-Ag-Bi-Sb-As melt is also tied to this process.

The formation of sulfarsenides represents two significant changes in the nature of the mineralization at Cobalt. Firstly, these phases formed via CDP processes rather than the infilling of existing dilatancy in the vein network, thus earlier phases were first dissolved. Secondly, this assemblage marks the introduction of reduced sulfur as S^{1-} , thus a complementary increase and decrease in the activities of these phases. The latter favoured selective formation of cobaltite and gersdorffite where earlier Co- and Ni-diarsenides were present (e.g. along arsenide mineral boundaries or fractures in Figs. 10, 25). The chemistry for the sulfarsenides is seen to be a complete continuum of gersdorffite to cobaltite (Fig. 12) due to the incorporation of elements from the dissolved pre-existing Ni-Co-arsenides. As these reactions involve sulfidation, there

was also the net loss of As, the latter of which resulted in formation of late-stage arsenopyrite (Fig. 25B, C).

The general succession of Ni- to Co- to Fe-arsenides to sulfarsenides to sulfides noted above is interpreted to reflect a process whereby initial metals and anion production was in a continually reducing system with coupled oxidation of a carbon source which is seen as later infill of carbonate in the five-element systems (Markl et al., 2016; Scharrer et al., 2019). The aforementioned model was presented by Scharrer et al. (2019) to account for the precipitation sequence of minerals seen in five-element deposits, both based on their studies focused on European deposits, but also elsewhere. They concluded that primarily evolving fluid fO_2 , but also pH and P-T conditions, determine the fluid reaction pathway into respective arsenide mineral stability fields and the consequent Ni- to Co- to Fe-bearing mineral sequence. The fO_2 -pH conditions change throughout the paragenesis due to: (i) spatially restricted influx of a reducing agent from a local source (hydrocarbons, pre-existing sulfides, carbonaceous shales, or even Fe^{2+} -bearing minerals in host rocks); (ii) dissolution of earlier formed minerals; (iii) precipitation of new minerals; or (iv) fluid mixing. Furthermore, the type of reducing agent will have implications for the mineral sequence, as H^+ consumption as a function of O_2 depletion will vary between reductant type (Scharrer et al., 2019). Local (sample-scale) reversals or partial repetitions of the Ni- to Co- to Fe- mineral progression (e.g. late skutterudite postdating cobaltite; e.g. Skutt 2 in Fig. 25B) is interpreted to reflect a system whereby fluid chemical evolutionary pathways vary locally due to heterogeneous composition of the local source rocks and varying fluid-reductant interaction (Scharrer et al., 2019).

The transition from arsenide stability to sulfarsenides and the later sulfide stage reflects either one or both of changing redox state or changing fS_2 in the fluid (e.g. Kissin, 1992; Scharrer

et al. 2019). In the former, the noted progressive increase in redox which favoured di- and tri-arsenide formation must have reversed to allow sulfarsenide formation then continued into the base-metal stage. Alternatively, or in concert with the latter, is that the early formation of arsenides may relate to an initially low fS_2 due to either a lack of sulfur in the system or it being oxidized as sulfate and thus it remained in solution, although the lack of abundant sulfate phases (e.g., barite, anhydrite) suggest the former and suggests therefore that late-stage fluid interaction with sulfidic country rock, such as the interflow sedimentary rocks, could have remobilized sulfide. Also relevant to this argument are reaction rates, as noted by Scharrer et al. (2019), such that native metal and arsenite/arsenate to arsenide reduction is kinetically faster compared to the sulfate to sulfide reduction (Ohmoto and Lasaga, 1982). Rare examples of cross-cutting mineral relationships observed in the Cobalt district do indicate rare sulfarsenides pre-dating arsenides, thus locally fluctuating sulfide activity may at least locally have favored early formation of sulfarsenides.

2.5.4 Carbonate REE and trace element data

Analysis of carbonate phases through the vein paragenesis provides the means to address fluid reservoirs using the REE and also to track the redox state of the system due to the update, or not, of redox sensitive elements such as Fe, Mn, Ce and Eu.

Several features of the carbonates suggest they formed from fluids that were overall reducing in the context of the analysed elements. Thus, enrichment of both Fe and Mn (1000s ppm to 2 wt. %) suggest in both cases Fe^{2+} and Mn^{2+} dominated over their oxidized equivalents. The lack of negative Ce anomalies, as would be expected if Ce^{4+} were present due to an oxidized fluid, also favours a reduced fluid. Lastly, the relationship between the Eu anomalies and Fe and Mn contents indicate that enrichment of the latter elements is not sensitive to the degree of the

Eu anomaly in the carbonates. The latter precludes therefore a redox control and instead suggests the Fe and Mn, and also Sr, contents of the fluid varied. As for the Eu anomaly, this is very similar for most carbonates at 0.1 to 0.2 (Figs. 21, 22) and is uniform in each carbonate analysed. This suggests little if any change in oxidation state of Eu, as excursions to a more reduced fluid would favour Eu^{2+} which would be manifest as positive Eu anomalies (e.g. Bau and Möller, 1992; Rollinson, 1993; Kontak and Jackson, 1995). Thus, the observed Eu anomaly is considered an intrinsic feature of the hydrothermal fluid inherited from its source.

Two features of the REE data are addressed, first the patterns and the variable $\sum\text{REE}$ and secondly the implications for fluid reservoirs. In regards to the first, we note that three general patterns are present, but the one with a generally flat pattern or with slight LREE enrichment dominates. Furthermore, in most analysed samples there is a similar maximum CN value and with decreasing $\sum\text{REE}$ patterns remain similar until the LREE fall to <10 CN values at which point the LREE decrease and a positive CN profile develops (i.e. $\text{La}_{\text{CN}} < \text{Lu}_{\text{CN}}$). The common inflection of Ho is attributed to the tetrad effect. This observed REE behaviour is not uncommon for hydrothermal minerals, for example it is common for both carbonate (e.g. Kontak and Jackson, 1995, 1999) and scheelite (e.g. Brugger et al., 2000b; Poulin et al. 2018), and is attributed to closed system fluid fraction (Möller and Morteani, 1983). In the case of carbonate, there is little preferential fractionation of the REEs (Zhong and Mucci, 1995), hence, similar patterns are recorded as the system fractionates. This also applies to patterns generated from replenishment of the same fluid, which would increase the $\sum\text{REE}$ values but not change the pattern. As for the lowering of the LREE, this is attributed to the role of synchronous phase enrichment in the LREE precipitating (e.g. monazite, apatite; Rollinson, 1993). That monazite was observed in one of the five-element vein samples during petrography, although not subject

to LA-ICP-MS analysis, is therefore noted. Using this interpretation for the REE patterns noted, those samples that have low Σ REE values with depletion of the LREEs (e.g., Fig. 22E, I, J) are considered to reflect fluids where earlier formation of carbonate and monazite occurred, that is evolved or fractionated fluids. For the few patterns where the MREEs are depleted, we have not identified an appropriate phase that might account for this (e.g. apatite, axinite, rutile, and anatase are among many accessory phases reported by Petruk, 1971b; Jambor, 1971c; and Andrews et al., 1986). An alternative model to the above is fluid mixing with related dilution of the original fluid (e.g. Mathieu et al., 2015). Based on the REE patterns, this would require a fluid depleted in Σ REE with a strongly fractionated pattern low in LREE (i.e. <0.1 CN) and relatively enriched in HREE at a similar value of the primary fluid. That low-salinity fluids occur in the veins (Marshall et al. 1993), albeit in low abundance, is consistent with mixing, but stable isotopes only record a single fluid through the vein paragenesis (Kerrick et al., 1986). Based on this, the model discussed previously is therefore preferred.

The REE data can also be used to make inferences about the rocks that the vein fluid equilibrated with due to protracted fluid-rock interaction. This is particularly applicable for carbonates since there is little preferential partitioning of the REEs (Zhong and Mucci, 1995), thus such patterns reflect the REE signature of the fluid. Also relevant is that modification of the fluid due to wallrock alteration is deemed insignificant in comparison, as it is restricted to narrow halos and also preceded carbonate precipitation. Thus the REE patterns unmodified due to in-situ fluid fractionation, that is those with highest Σ REE, are considered to best reflect the primary signature of the fluid. Comparing this pattern with plausible reservoirs represented by the Cobalt lithologies in Figure 21F reveals no obvious or preferred source as these units all have strongly fractionated CN profiles. Also of note in this regard is that the REE signature for the Nipissing

gabbro, a preferred source of fluids for some (e.g. Marshall, 2008), is markedly different to the carbonate REE signatures can thus cannot be considered as a fluid source. Thus, the REE data suggest the fluids have equilibrated with one or more lithologies at depth along its flow path that are different to the those in the Cobalt district.

2.5.5. Fluid inclusions

Previous studies of Cobalt materials (Scott and O'Connor, 1971; Kerrich et al., 1986; Marshall et al., 1993) identified three distinct fluid inclusion types in the ore system: (i) a L-V-H type of 35 wt. % equiv. NaCl with a CaCl₂: NaCl: KCl ratio of 3:2:1, respectively; (ii) a L-V type with ranging salinities up to 25 wt.% equiv. NaCl; and (iii) V-rich type. Whereas the high-salinities and Ca-rich nature were interpreted to indicate basinal-brines for the fluid origin, the nature of the V-rich type was controversial with both fluid unmixing (Kerrich et al., 1986) and post-entrapment modification (i.e. necking; Marshall et al., 1993; Marshall, 2008) suggested. Regardless of the latter, the microthermometric data for the other types indicated fluid entrapment between 300° and 350°C at pressures between 60 and 136 MPa (600 and 1360 bars; Marshall et al., 1993).

This study has confirmed the predominance of the L-V-H and lesser L-V type inclusions, with the latter further refined based on consistent L:V ratios into two FIAs, types iii (<20% V) and iv (>40% V). However, in contrast to the earlier studies, the samples used in this work were in fact characterized by having V-rich inclusions as the most common FIA. Furthermore, these inclusions were noted to extend throughout the paragenesis (Fig. 24) which indicates the process responsible for their formation extended over the duration of the mineralization. The results of preliminary petrographic studies and microthermometry on quartz-hosted fluid inclusions hosted in base-metal (i.e. Cu, Zn and Pb) sulfide veins provide insight into the five-element veins as the

inclusion types noted are identical, as are the overlap in thermometric data. Thus, the Th values and salinities for type i L-V-H inclusions match those of earlier workers (Scott and O'Connor, 1971; Kerrich et al., 1986; Marshall et al., 1993) on Cobalt-type veins and suggest a similar fluid event for both systems. However, the occurrence of carbonic V-inclusions is anomalous, as these have not been reported before in the Cobalt district. Two aspects are noted in regards to these inclusions: (1) the H₂O-CO₂ type equate to the type iv of the five-element veins in terms of room temperature appearance, hence these may also be of similar chemistry, but need to be verified; and (2) the type v inclusions also appear the same in the two systems, which strongly suggests a similar mixed carbonic fluid of CO₂-CH₄±N₂ chemistry in both. The obvious source of carbon in these fluids is the interflow sedimentary rocks in the Archean basement, which could have liberated the carbon via oxidation of graphite (e.g. Ohmoto and Rye, 1979). That some of the H₂O-CO₂ inclusions are saline and Ca-bearing based on microthermometric data suggest that such fluid:rock interaction may be including the saline fluid noted by others and confirmed in this study (i.e. types i and ii). Although beyond the scope of the present study, it is worth noting that generation of a mixed volatile fluid (i.e. CH₄-CO₂±N₂) in a high-crustal setting, as is likely for the Cobalt system, will facilitate fluid mixing (Roedder, 1984; Van den Kerkhof and Thiéry, 2001) and, therefore, it is very possible that the H₂O-CO₂ and CH₄-CO₂±N₂ type inclusions were generated via such a process.

2.6 Refining the genetic model for Cobalt five-element mineralization

2.6.1 Review of earlier models

There is no consensus on a universal genetic model for the five-element vein deposits, in part due to the distinctiveness of areas in terms of geological setting, host rocks, and physiochemistry of mineralizing fluids. However, a number of similarities are common to all

districts: (i) disequilibrium ore textures (e.g., dendrites); (ii) complex ore mineralogy with common paragenesis (e.g. arsenides to sulfarsenides to sulfides); (iii) intense, but localized wallrock alteration; (iv) high ore tenors; and (v) ore shoots developed at intersections of veins, shear/fracture zones, or at lithological contacts (e.g., Petruk, 1971a; Andrews et al., 1986; Changkakoti and Morton, 1986; Franklin et al., 1986; Markl et al., 2016; Burke et al., 2018). Recent work on the European deposits (Markl et al., 2016; Burisch et al., 2017; Kreissl et al., 2018; Scharrer et al., 2019) has provided an updated model that accounts for the noted features. These studies suggest a rapid-onset and continuous reduction of a metal-rich fluid with the coupled oxidation of a local reductant in the host rocks, such as hydrocarbons, graphite, Fe^{2+} phases, or pre-existing sulfides. One novel part of this model is “natural fracking” due to the liberation of reduced hydrocarbons (e.g. methane) which mixed with the oxidized metal-rich fluids and facilitated precipitation of native metals and arsenides (Markl et al., 2016). More recently, Scharrer et al. (2019) modelled the varying metal abundances and mineral paragenesis of European as resulting from differing reaction kinetics, due to fluid pH and $f\text{O}_2$, and the reductant species involved that is deposit specific.

For the Cobalt deposits, several genetic models exist (section 2.2). Several authors suggest leaching of metals from sulfide-rich Archean basement units due to interaction with evolved, highly saline Huronian formational brines, although derivation of metals from the intrusion has been preferred by some. Regardless, fluid circulation relates to cooling of the Nipissing gabbro and heat transfer with resulting hydraulic gradients developed, the timing of which is generally supported by model Pb-isotope data for sulfides (Thorpe, 1974; Thorpe et al., 1986; Potter and Taylor, 2009). These fluids were subsequently focused into structural traps controlled by the configuration of the gabbro along the Huronian-Archean unconformity and

possibly regional structures. The extraction of metals due to fluid interaction with the sulfide-rich layers of the interflow sedimentary units have often been cited (e.g. Boyle and Dass, 1971b; Goodz et al., 1986; Smyk and Watkinson, 1990); isotopic data (Pb, S, C) are not inconsistent with this model (Thorpe, 1974; Thorpe et al. 1986; Goodz et al., 1986; Kerrich et al., 1986). Aqueous phase separation, or degassing, has also been suggested as a deposition mechanism (Andrews et al., 1986; Kerrich et al., 1986), as opposed to simple fluid mixing of a saline fluid with a more dilute fluid (Marshall et al., 1993).

As these and many other studies of the Cobalt district highlight, there remains uncertainty in regards to the many aspects that characterize the mineralization: the source of metals, genetic link between the Nipissing gabbro and the veins, restriction of veins to a narrow vertical interval, high ore-tenor, metal deposition mechanism(s), metal zoning, and complex disequilibrium textures. The present study has provided new data, which permits reassessing some aspects of the Cobalt deposits and is now addressed below.

2.6.2 An updated genetic model for the Cobalt deposits: Interflow sedimentary sulfide partial melting: metal source, mobilization, and concentration

There has long been the recognition of the proximity of sulfidic layers in the interflow sedimentary units and the silver rich veins in Cobalt (see Patterson, (1979); Nichols (1988); Smyk and Watkinson (1990), and references therein; Fig. 4). Although not extensively studied, these layers are known to have anomalous metal contents in the Cobalt district (Ag, Ni, Co, As, Sb, Bi, Cu, Hg; Boyle and Dass 1971b; Smyk, 1987; unpublished data, First Cobalt Corp.), but also in the Gowganda district, as recently summarized by Hamilton (2020). This study also suggests a correlation of metal enrichment (i.e. Co, Ni) to sites proximal to the Archean

basement and likely interflow sedimentary units. That many of these elements are also enriched in primary pyrite hosted in graphitic sediments related to hydrothermal seafloor processes using modern LA ICP-MS analytical methods (e.g. Maslennikov and Large, 2021) is intriguing and likely relevant, but further work is clearly needed to evaluate this. Furthermore, it has been suggested many of the aforementioned elements were mobilized physically or hydrothermally from these sulfidic layers (e.g. Petruk, 1968; Goodz et al., 1986; Smyk and Watkinson, 1990). Of particular note are the observations of Smyk and Watkinson (1990), who suggested mobilization of the sulfides via secretion injection structures, which might be re-interpreted in the context of modern processes as partial melts (e.g. Tomkins et al., 2007; Mavrogenes et al., 2013). Taking into account these earlier observations at Cobalt and the fact that Pb isotope studies broadly constrain Cobalt vein formation to the emplacement of the Nipissing gabbro, we strongly favour the Archean sulfidic interflow sedimentary units, both at the present level of exposure but also at depth, as the most likely metal source involved in the five-element veins. In addition, we suggest that the Nipissing intrusive settings, which is part of a much larger magmatic system at depth, may have mobilized these metals as melts, as further discussed below.

The conventional understanding has been that most low-temperature ore systems relate to metal transport via ligands in fluids and for Cobalt five-element veins as metal-chloride complexes (Marshall et al., 1993). Thus, we note the potential relevance of these veins to alternative methods of metal mobility, namely nanoparticles of gold (e.g. Saunders and Burke, 2017; Voisey et al., 2020; Petrella et al., 2020; Hastie et al., 2021) and base, semi- and precious-metal melts (e.g. Tomkins et al., 2007; Tooth et al., 2011; Mavorogenes et al., 2013; Acosta-Góngora et al., 2015; Govindarao et al., 2020); both of these processes have gained momentum in recent years. In particular, the relevance to the current study relates to the effect of Sb, Bi, Hg,

Ag and As, part of the LMCE assemblage of Frost et al. (2002), on the melting points of mixed metal assemblages, as Tomkins et al. (2007) summarized, and the textures formed (e.g. dendrites) upon the crystallization of such melts (Mavrogenes et al., 2013). We highlight therefore the forward thinking of Petruk (1968) who noted this as part of his observations and suggested that such a process may be relevant at Cobalt. Similarly, the physical mobilization of sulfides mentioned by Smyk and Watkinson (1990) is again noted. Lastly, Marshall (2008) discussed the relevance of Ag melts at Cobalt, but only in the context of late-stage silver as veins cutting earlier arsenides and carbonate gangue.

Although details of the proposed metal melt model (MMM) below needs refinement, the general idea is summarized (Fig. 26). Thus, rather than partial dissolution of sulfides (e.g. pyrrhotite to pyrite; Goodz et al., 1986) and complementary release of entrained metals as aqueous species, we suggest that metals were mobilized due to partial melting of sulfidic horizons via contact-type metamorphism proximal to Nipissing gabbroic magmas to generate mixed sulfarsenide melts (SAM). Although specific relevant model systems involving elemental assemblages of interest has not been experimentally explored (e.g. Co-Ni-As-S-Sb), temperature exceeding 500°C were likely and thus sufficient to generate melts given the elemental assemblages (Tomkins et al., 2007). Once generated, this melt needs to be mobilized, and we suggest this may have occurred as nano-melts entrained in the convecting hydrothermal fluid, related to the Nipissing gabbro, which we and others have documented as a saline fluid present in the pre-ore comb quartz and also implicated in intense wallrock alteration. This study also provides further important new data in this context, this being the probable abundance of carbonic fluids as both $\text{H}_2\text{O}-\text{CO}_2\pm\text{N}_2$ and $\text{CO}_2-\text{CH}_4\pm\text{N}_2$ types. Generation of this mixed volatile fluid strongly suggests variable oxidation of graphite in the Archean graphitic sedimentary rocks.

Such a fluid may be relevant as a means to dilatant earlier fractures that hosted the silver veins via fluid overpressuring, thus akin to the fracking model of Markl et al. (2016) for the European five-element veins and the fault-valve model for orogenic gold settings of Sibson et al. (1988). In addition, the carbonic inclusions noted also account for the abundance of late-stage carbonate in the veins. Lastly, if the carbonic fluid was immiscible at depth, as at the level of current exposure, it may have facilitated the upward floating of SAM, thus similar to the buoyant-segregation model of Knipping et al. (2015) whereby magnetite is floated due to wetting with immiscible fluids in magmas to form Kiruna-type Fe deposits. This mechanism of melt mobilization is suggested given the absence of physical mobility related to deformation, as suggested from mobilization of sulfide melts accompanying metamorphism (e.g. Frost et al., 2002; Tomkins et al., 2007).

Further evaluation of the MMM can also account for other important features in the Cobalt district – high ore tenor, metal zoning and textures. The anomalous high-ore tenor and narrow wallrock alteration halo has long been an anomalous feature noted at Cobalt (Andrews et al., 1986), but better resolved by a MMM since the amount of fluid needed is much reduced. As for zoning, it has been noted that from top to bottom, such as examined in detail at the Silverfields mine (Petruk, 1968), there is a distinct change from Ni-As, to Ni-Co-As, to Co-As, Co-Fe-S, to Fe-As. Importantly, each of these zones is internally complex with minor amounts of other elements (i.e. Co in the Ni-As zone), Ag is abundant in the upper Ni-Co zones, and S is omitted. We suggest the zoning reflects distillation or fractionation of the SAM upon its ascent, locally accumulating and cooling with enrichment of the residual melt in LMCE which enables it to be further mobilized. The upward concentration of Ag, which is known to be enriched in Sb and Hg (Petruk, 1968; Petruk et al., 1971b; Marshall, 2008; this study) which lower the melting

point of such mixed melts, is consistent with this model. As for the textures, it is important to note that whereas silver at Cobalt is renowned for its dendritic or rosette habit, the Co-Ni arsenide phases are also characterized by these features (Bastin, 1950; Petruk, 1968). Thus, we note that the MMM allows for a change in composition of the melt via its fractionation, hence formation of dendritic-textures in nickeline and skutterudite is accommodated. As for the more common presence of this texture in silver, this reflects its enrichment in the residual SAM. Formation of these disequilibrium textures are ascribed to undercooling (ΔT) of the melts and is favoured due to formation of the veins in a shallow-level setting (<4-5 km; Marshall et al., 1993). In this setting, both the low ambient temperature of the wallrock and the high-aspect nature of the narrow veins would favour heat loss. A similar ΔT model has been used to account for development of disequilibrium textures seen for example in pegmatites and has been modelled experimentally (e.g. London, 2008; Maneta and Baker, 2014).

The MMM can also provide a possible explanation of the limited vertical extents of the many veins mined which extended over a large area. As inferred above, the SAM would be concentrated while in a molten state and rise to a level controlled by the density and weight of these particles, which would have aggregated to a certain degree upon ascent. Though not numerically modelled, it is suggested that a level of neutral buoyancy would be reached, as in ascending magmas. In addition, the cooling of the SAM would bring about their solidification. Thus, these factors are suggested to potentially have controlled the limited vertical extent of the veins.

The Co-rich nature of the Cobalt district is considered to reflect the metal enrichment of the source, this being the sulfidic interflow horizons in the basement. There is not a sufficient database to properly assess this, but data in Smyk (1987) suggests similar abundances of each

(i.e., 10s to 100s ppm) for his limited sample collection. Thus, this might suggest differences in the relative mobility of Co versus Ni in the SAM generated may be responsible for the apparent Co-rich nature of the Cobalt district, but clearly needs further study. Similarly, the local-scale heterogeneity of the five-element veins, such as the Ag-rich core to the Cobalt district (section 2.4.4), might reflect variation in the abundance and chemistry of sulfides in the source interflow sedimentary rock units; this could be further studied and assessed via whole-rock and mineral chemistry. Also of relevance to metal zoning is a potential district-scale thermogradient emanating from the Nipissing gabbro injections.

As noted earlier, there is an overprint of the primary arsenide mineralogy by sulfarsenides which is here attributed to CDP processes (Figs. 12, 25). Thus, there is still an important role for fluids in the evolution of the Cobalt ore system, which we now ascribe to having modified its primary mineralogy. This stage accounts for the sulfarsenides and paragenetically similar complex mineralogy that the Cobalt veins are known for (e.g. Bastin, 1925, 1950; Petruk, 1968, 1971a, b). During this late stage, metals were also remobilized as melts, such as Ag and Bi (this study; Marshall, 2008) for which the eutectic of 260°C (Hansen and Anderkok, 1958) falls within the temperature constraints of fluid inclusions (Kerrick et al., 1986; Marshall et al., 1993). The presence of dendritic silver hosted in calcite without rimming arsenides, for which Cobalt is well known, and which resemble dendritic gold (e.g., Saunders and Burke, 2017; Sanders et al., 2008) likely formed from this process by mobilizing the silver from earlier rosette- and cruciform-textured silver.

2.7 Conclusion

The five-element association is an umbrella term that encompasses deposits from a variation of geologic settings. Despite a similar metal assemblage (Ag-Ni-Co-As-Bi-Sb-U-Cu-

Pb-Zn-Au), the metal association can form due to different processes. This study of the famed Cobalt setting for Ag-Co-Ni-As-Bi silicate-carbonate veins that formed synchronous with the Nipissing gabbro intrusion are interpreted to represent a district-scale homogeneous hydrothermal-metal melt system driven by contact metamorphism and partial melting of pre-existing sulfides in underlying Archean interflow sedimentary rocks. Fractures proximal to the regional Archean-Paeoproterozoic unconformity allowed for ingress of arsenide-sulfide melts and fluids, the former generated via metamorphism and the latter due to circulation of Huronian formational brines. This new model for the Cobalt ore setting addresses many of the outstanding issues for the setting, as summarized below.

1. Explains the localized and narrow wallrock alteration zones;
2. Vertical zoning of the ore systems, from top to bottom Ni-As, to Ni-Co-As, to Co-As, Co-Fe-As, to Fe-As;
3. The vertically restricted nature of the ore zones;
4. The development and distribution of disequilibrium textures which are ascribed to ΔT of the arsenide-sulfide melts;
5. Generation of the veins due to fluid overpressuring related to the carbonic nature of the fluids not recognized before, which also addresses the presence of abundant late carbonate in the veins;
6. The role of the interflow sedimentary units in the Archean basement as a contributor of metals and volatized carbon now related to the carbonic nature of the fluid based on fluid inclusion studies.

Based on these criteria, it is now possible to identify geochemical exploration vectors emphasising elemental cobalt. These include:

1. Locations where the Nipissing gabbro intrudes close to interflow sedimentary rock, particularly where massive sulfide lenses reside;
2. Within 200 m of the Nipissing gabbro, which is assumed the average extent of the contact aureole;
3. Proximal to the regional Archean-Paleoproterozoic unconformity;
4. Within or proximal to fault and/or fracture zones, lithological contacts, or intersections with shallow-dipping quartz-carbonate-sulfide veins;
5. The limited vertical extent of five-element mineralization is likely real and not apparent, as this relates to the depth at which neutral buoyancy of the migrating melts was achieved;
6. The central area of Cobalt favours Co-arsenides, particularly skutterudite (CoAs_3), which correlates to high Ag values; however, peripheral areas show a higher Co:As ratio.
7. Vertical metal zonation of the five-element veins is probable, inferring vein-specific depths at which Co is favoured; however, this requires further study for each vein.

A working model for the generation of the arsenide-sulfide melts is proposed, but there is further need to better assess this model, in particular the sourcing of the metals, the variation of chemistry of the source rocks, the validity of the mobility and ascent of micro-melts into the ore system, and the new interpretations for the genesis of both the primary and secondary mineral assemblages, both of which accommodate recent advances in models for ore deposit systems.

References

- Acosta-Góngora, P., Gleeson, S.A., Samson, I.M., Ootes, L., and Corriveau, L., 2015, Golf refining by bismuth melts in the iron oxide-dominated NICO Au-Co-Bi ($\pm\text{Cu}\pm\text{W}$) Deposit, NWT, Canada, *Economic Geology*, v. 110, p. 291-314.
- Andrews, A.J., Owsiacki, L., Kerrich, R., and Strong, D.F., 1986, The silver deposits of Cobalt and Gowganda, Ontario. I: Geology, petrology and whole-rock chemistry: *Canadian Journal of Earth Sciences*, v. 23, p. 1480–1506.
- Appleyard, E.C., 1980, Host-rock alteration at the Silver fields mine, Cobalt, Ontario – final report, Ontario Geological Survey, Geoscience Research Grant No. 70, 83 p.
- Ayer, J., Amelin, Y., Corfu, F., Kamo, S., Ketchum, J.F., Kwok, K., and Trowell, N.F., 2002a, Evolution of the Abitibi greenstone belt based on U-Pb geochronology: Autochthonous volcanic construction followed by plutonism, regional deformation and sedimentation: *Precambrian Research*, v. 115, p. 63–95.
- Ayer, J.A., Trowell, N.F., and Josey, S., 2004a, Geological compilation of the Abitibi greenstone belt: Ontario Geological Survey Map P3565.
- Ayer, J.A., Thurston, P.C., Bateman, R., Dubé, B., Gibson, H.L., Hamilton, M.A., Hathway, B., Hocker, S.M., Houlié, M.G., Hudak, G., Ispolatov, V.O., Lafrance, B., Lesher, C.M., MacDonald, P.J., Péloquin, A.S., Piercey, S.J., Reed, L.E. and Thompson, P.H., 2005, Overview of results from the Greenstone Architecture Project: Discover Abitibi Initiative; Ontario Geological Survey, Open File Report 6154, 146 p.
- Ayer, J.A., Chartrand, J.E., Grabowski, G.P.D., Josey, S., Rainsford, D. and Trowell, N.F., 2006, Geological compilation of the Cobalt–Temagami area, Abitibi greenstone belt, Ontario Geological Survey, Preliminary Map P.3581, scale 1:100 000.
- Bastin, E.S., 1925, Primary native silver ores of South Lorraine and Cobalt, Ontario. *Economic Geology*, v. 20, p. 1-24.
- Bastin, E.S., 1939, The nickel-cobalt-native silver ore type: *Economic Geology*, v. 34, p. 40–79.

- Bastin, E.S., 1950, Significant replacement textures at Cobalt and South Lorraine, Ontario, Canada, *Economic Geology*, v. 45, p. 808-817.
- Bau, M., 1991, Rare-earth element mobility during hydrothermal and metamorphic fluidrock interaction and the significance of the oxidation state of europium. *Chem. Geol.* 93, p. 219–230.
- Bau, M., and Möller, P., 1992, Rare earth element fractionation in metamorphogenic hydrothermal calcite, magnesite and siderite. *Mineralogy and Petrology*, v. 45, p. 231-245.
- Baumann, L., Kuschka, E., and Seifert, T., 2000, Lagerstätten des Erzgebirges, Enke, Stuttgart, 303 p.
- Biagioni, C., D’Orazio, M., Fulignati, P., George, L.L., Mauro, D., and Zaccarini, F., 2020, Sulfide melts in ore deposits from low-grade metamorphic settings: insights from fluid and Tl-rich sulfosalt microinclusions from the Monte Arsiccio mine (Apuan Alps, Tuscany, Italy), *Ore Geology Reviews*, v. 123, 103589.
- Bodnar, R.J., 2003a, Introduction to fluid inclusions. *In* I. Samson, A. Anderson, & D. Marshall, eds. *Fluid Inclusions: Analysis and Interpretation*. Mineral. Assoc. Canada, Short Course 32, p. 1-8.
- Bodnar, R.J., 2003b, Introduction to aqueous-electrolyte fluid inclusions. *In* I. Samson, A. Anderson, & D. Marshall, eds. *Fluid Inclusions: Analysis and Interpretation*. Mineral. Assoc. Canada, Short Course 32, p. 81-100.
- Boyle, R.W., 1968, The geochemistry of silver and its deposits: Geological Survey of Canada, Bulletin 160, 264 p.
- Boyle, R. W., and Dass, A. S., 1971b, Origin of the native silver veins at Cobalt, Ontario, *In* The silver-arsenide deposits of the Cobalt-Gowganda region, Ontario, *Edited by* E. G. Berry: *The Canadian Mineralogist*, 11, Part 1, p. 4-14–4-17.
- Brugger, J., Lahaya, Y., Costa, S., Lambert, D., and Bateman, R., 2000b, Inhomogenous distribution of REE in scheelite and dynamics of Archean hydrothermal systems (Mt.

- Charlotte and Drysdale gold deposits, Western Australia), *Contributions to Mineralogy and Petrology*, v. 139, pg. 251-264.
- Burisch, M., Gerdes, A., Walter, B.F., Neumann, U., Fettel, M., and Markl, G., 2017, Methane and the origin of five-element veins: mineralogy, age, fluid inclusion chemistry and ore forming processes in the Odenwald, SW Germany: *Ore Geology Reviews*, v. 81, p. 42–60.
- Burke, J.S., Hanley, J., Trottier, C., Ootes, L., Zajacz, Z., Sharpe, R., and Fayek, M., 2018, The origin of polymetallic Ni-Co-As-Bi-Sb(-Ag-U) veins in the East Arm Basin and southern Slave Province, Northwest Territories, Unpublished M.Sc. thesis, Halifax, Canada, St. Mary's University.
- Card, K.D., McIlwaine, W.H., and Meyn, H.D., 1973, Geology of the Maple Mountain area, Operation Maple Mountain, districts of Timiskaming, Nipissing and Sudbury: Ontario Division of Mines, GR 106, 160 p.
- Changkakoti, A., and Morton, R., 1986, Electron microprobe analyses of native silver and associated arsenides from the Great Bear Lake silver deposits, Northwest Territories, Canada: *Canadian Journal of Earth Science*, v. 23, p. 1470–1479.
- Changkakoti, A., Morton, R., Gray, J., and Yonge, C., 1986, Oxygen, hydrogen, and carbon isotopic studies of the Great Bear Lake silver deposits, Northwest Territories: *Canadian Journal of Earth Science*, v. 23, p. 1463–1469.
- Ciobanu, C.L., Cook, N.J., Damian, F., and Damian, G., 2006, Gold scavenged by bismuth melts: An example from Alpine shear-remobilizates in the Highiş Massif, Romania, *Mineralogy and Petrology*, v. 87, p. 351-384.
- Corfu, F., and Andrews, A. J., 1986, A U-Pb age for mineralized Nipissing diabase, Gowganda, Ontario: *Canadian Journal of Earth Sciences*, v. 23, p. 107–109.
- Daigneault, R., Mueller, W.U., and Chown, E.H., 2004, Abitibi greenstone belt plate tectonics: A history of diachronic arc development, accretion and collision, *In* Eriksson, K.A., Altermann, W., Nelson, D.R., Mueller, W., Catuneanu, O., and Strand, K., eds., *The Precambrian earth: Tempos and events*: Amsterdam, Elsevier, *Developments in Precambrian Geology* 12, p. 88–103.

- Davis, D.W., 2002, U-Pb geochronology of Archean metasediments in the Pontiac and Abitibi subprovinces, Québec: Constraints on timing, provenance and regional tectonics: *Precambrian Research*, v. 115, p. 97–117.
- Dimroth, E., Imreh, L., Goulet, N., and Rocheleau, M., 1983, Evolution of the south-central segment of Archean Abitibi Belt, Quebec; Part II, Tectonic evolution and geomechanical model: *Canadian Journal of Earth Sciences*, v. 20: p. 1355–1373.
- Dong, G., Morrison, G., and Jaireth, S., 1995, Quartz textures in epithermal veins, Queensland – Classification, origin, and implication, *Economic Geology*, v. 90, p. 1841-1856.
- Doughty, M., Eyles, N., and Eyles, C., 2013, High-resolution seismic reflection profiling of neotectonic faults in Lake Timiskaming, Timiskaming Graben, Ontario-Quebec, Canada. *Sedimentology*, v. 60, p. 983-1006.
- Dunham, K., Beer, K.E., Ellis, R.A., Gallagher, M.J., Nutt. M.J.C., and Webb, B.C., 1978, *In* Bowie, S.H.U, Kvalheim, A., and Haslam, H.W., eds., *Mineral Deposits of Europe, Northwest Europe: The Institution of Mining and Metallurgy and the Mineralogical Society*, London, United Kingdom, v. 1, p. 263–317.
- Eakins, P.R., 1961, Cylindroidal jointing in diabase at Gowganda, Ontario: *Geological Association of Canada*, v. 13–16, p. 85–93.
- Essarraj, S., Boiron, M.C., Cathelineau, M., Banks, D.A., and Benharref, M., 2005, Penetration of surface-evaporated brines into the Proterozoic basement and deposition of Co and Ag at Bou Azzer (Morocco): evidence from fluid inclusions: *Journal of African Earth Science*, v. 41, p. 25–39.
- Fahrig, W.F., and Wanless, R.K., 1963, Age and significance of diabase dyke swarms of the Canadian Shield: *Nature*. v. 200, p. 934–937.
- Fahrig, W.F., Gaucher, E.H., and Larochelle, A., 1964, Paleomagnetism of diabase dykes of the Canadian Shield: *Canadian Journal of Earth Sciences*, v. 2, p. 278-298.
- Fairbairn, M.W., Hurley, P.M., Card, K.D., and Knight, C.J., 1969, Correlation of radiometric ages of Nipissing diabase and Huronian metasediments with Proterozoic orogenic events in Ontario: *Canadian Journal of Earth Sciences*, v. 6, p. 489–497.

- Fanlo, I., Subías, I., Gervilla, F., Paniagua, A., García, B., 2004, The composition of Co–Ni–Fe sulfarsenides, diarsenides and triarsenides from the San Juan de Plan deposit, Central Pyrenees, Spain. *Can. Mineral.* v. 42, p. 1221–1240.
- Franklin, J., Kissin, S., Smyk, M., and Scott, S., 1986, Silver deposits associated with the Proterozoic rocks of the Thunder Bay district, Ontario: *Canadian Journal of Earth Science*, v. 23, p. 1576–1591.
- Frieman, B.M., Kuiper, Y., Kelly, N.M., Monecke, T., and Kylander-Clark, A., 2017, Constraints on the geodynamic evolution of the southern Superior Province: U-Pb LA-ICP-MS analysis of detrital zircon in successor basins of the Archean Abitibi and Pontiac subprovinces of Ontario and Quebec, Canada, *Precambrian Research*, v. 292, DOI:10.1016/j.precamres.2017.01.027
- Frost, B.R., Mavrogenes, J.A., and Tomkins, A.G., 2002, Partial melting of sulfide ore deposits during medium and high-grade metamorphism: *The Canadian Mineralogist*, v. 40, p. 1–18.
- Goldstein, R.H., and Reynolds, T.J., 1994, Systematics of fluid inclusions in diagenetic minerals: *Society for Sedimentary Geology Short Course 31*, 199 p.
- Götze, J., Plötze, M., and Habermann, D., 2001, Origin, spectral characteristics and practical applications of the catholuminescence (CL) of quartz – a review, *Mineralogy and Petrology*, v. 71, p. 225-250.
- Goodz, M.D. and Watkinson, D.H., Smejkal, V., and Pertold, Z., 1986, Sulfur-isotope geochemistry of silver-sulpharsenide vein mineralization, Cobalt, Ontario: *Canadian Journal of Earth Science*, v. 23, p. 1551–1567.
- Govindarao, B., Pruseth, K.L., and Mishra, B., 2020, Sulfide partial melting and galena-tetrahedrite intergrowth textures: An experimental study, *Mineralogical Magazine*, V. 84(6), p. 859-868.
- Gunning, H.C., and Ambrose, J.W., 1939, The Timiskaming-Keewatin problem in the Rouyn-Harricaw region, northwestern Quebec: *Transactions of the Royal Society of Canada*, v. 33, Ser. 3, Sec. 4, p. 19–49.

- Halls, C., and Stumpfl, E., 1972, The five-element (Ag-Bi-Co-Ni-As) vein deposit – A critical appraisal of the geological environments in which it occurs and of the theories affecting its origin: Proceedings Volume: 24th International Geological Congress.
- Hamilton, M.A., 2006, Summary of U-Pb geochronological results for 2005–2006 programs, Precambrian Geoscience Section, Ontario Geological Survey; unpublished report of the Jack Satterly Geochronology Laboratory, Department of Geology, University of Toronto, Toronto, Ontario, 10 p.
- Hamilton, G., 2020, Mineralogical and Fluid Inclusion Studies of the Five-Element Type Polymetallic (Co+Ni+Cu+Pb+Bi+Ag±Au±U) veins of the McAra Property, Southwest Timiskaming District, Ontario, Canada, Unpublished M.Sc. thesis, Sudbury, Canada, Laurentian University.
- Hansen, M., and Anderko, K., 1958, Constitution of Binary Alloys: McGraw Hill, New York, 1305 p.
- Hastie, E., Schindler, M., Kontak, D.J., and Lafrance, B., 2021, Significance of gold nanoparticle aggregation in orogenic gold deposits. *Nature Communications Earth & Environment* 2, Article number: 57, doi.org/10.1038/s43247-021-00126-6.
- Heather, K.B., 2001, The geological evolution of the Archean Swayze greenstone belt, Superior province, Canada: Unpublished Ph.D. thesis, Staffordshire, UK, Keele University, 370 p.
- Hester, B.W., 1967, Geology of the silver deposits near Miller Lake, Gowganda: *The Canadian Mining and Metallurgical Bulletin*, November. v. LXX, p. 277–286.
- Hofmann, F., 1992, Die Minerale des Annaberger Reviers im Sächsischen Erzgebirge: *Lapis* 24–32.
- Ichikuni, M., 1973, Partition of strontium between calcite and solution: Effect of substitution by manganese, *Chemical Geology*, v. 11, p. 315-319.
- Jaffe, F.C., 1986, Switzerland, *In* Dunning, F.W., and Evans., A.M., eds., *Mineral Deposits of Europe*, v. 3: Central Europe: The Institution of Mining and Metallurgy and the Mineralogical Society, London, p. 41–54.

- Jambor, J.L., 1971a, General geology of the Cobalt area, *In* The silver-arsenide deposits of the Cobalt-Gowganda region, Ontario, *Edited by* L.G. Berry: The Canadian Mineralogist, v. 11, Part 1, p. 12–33.
- Jambor, J.L., 1971c, Gangue mineralogy, *In* The silver-arsenide deposits of the Cobalt-Gowganda region, Ontario, *Edited by* L.G. Berry: The Canadian Mineralogist, v. 11, Part 1, p. 232–262.
- Jambor, J.L., 1971d, Wall rock alteration, *In* The silver-arsenide deposits of the Cobalt-Gowganda region, Ontario, *Edited by* L.G. Berry: The Canadian Mineralogist, v. 11, Part 1, p. 402–413.
- Jambor, J.L., 1971g, Origin of silver veins, *In* The silver-arsenide deposits of the Cobalt-Gowganda region, Ontario, *Edited by* L.G. Berry: The Canadian Mineralogist, v. 11, Part 1, p. 272–304.
- Kerrich, R., Strong, D., Andrews, A., and Owsiacki, L., 1986, The silver deposits at Cobalt and Gowganda, Ontario. III: Hydrothermal regimes and source reservoirs-evidence from H, O, C, and Sr isotopes and fluid inclusions: Canadian Journal of Earth Science, v. 23, p. 1519–1550.
- Kiefer, S., Majzlan, J., Chovan, M., Števkó, M., 2017, Mineral compositions and phase relations of the complex sulfarsenides and arsenides from Dobšiná (Western Carpathians, Slovakia). Ore Geol. Rev. v. 89, p. 894–908.
- Kissin, S.A., 1988, Nickel-cobalt-native silver (five-element) veins: A rift-related ore type. *In*: Kisvarsany, G., Grant, S., (Eds.), Proceedings Volume: North American Conference on Tectonic Control of Ore Deposits and the Vertical and Horizontal Extent of Ore Systems. University of Missouri, Rolla, p. 268–279.
- Kissin, S.A., 1992, Five-element (Ni-Co-As-Ag-Bi) veins: Geoscience Canada, v. 19, p. 113–124.
- Knight, C. W., 1924, Geology of the mine workings of Cobalt and South Lorrain silver areas: Ontario Department of Mines, Annual Report (1922) 3 1.

- Knipping, J.L., Bilenker, L.D., Simon, A.C., Reich, M., Barra, F., Deditius, A.P., Lundstrom, C., Bindeman, I., and Munizaga, R., 2015, Giant Kiruna-type deposits form by efficient floatation of magmatic magnetite suspensions, *Geology*, v. 43, p. 591-594.
- Kontak, D.J., and Jackson, S., 1995, Laser-ablation ICP-MS micro-analysis of calcite cement from a Mississippi-Valley-Type Zn-Pb deposit, Nova Scotia: Dramatic variability in REE content on macro- and micro-scales, *The Canadian Mineralogist*, v. 33, p. 445-467.
- Kontak, D.J., and Jackson, S.J., 1999, Documentation of variable trace- and rare-earth-element abundances in carbonates from auriferous quartz veins in Meguma lode-gold deposits, Nova Scotia, *The Canadian Mineralogist*, v. 37, p. 469-488.
- Kreissl, S., Gerdes, A., Walter, B., Neumann, U., Wenzel, T., and Markl, G., 2018, Reconstruction of a >200 Ma multi-stage “five element” Bi-Co-Ni-Fe-As-S system in the Penninic Alps, Switzerland: *Ore Geology Reviews*, v. 95, p. 746–788.
- Krogh, T.E., Davis, D.W., and Corfu, F., 1984, Precise U -Pb zircon and baddeleyite ages for the Sudbury area, *In The geology and ore deposits of the Sudbury structure*, Edited by E.G. Pye, A. J. Naldrett, and P. E. Giblin: Ontario Geological Survey, Special v. 1, p. 431–446.
- Krogh, T.E., Kamo, S.L., and Bohor, B.F., 1996, Shock metamorphosed zircons with correlated U-Pb discordance and melt rocks with concordant protolith ages indicate an impact origin for the Sudbury structure: *Earth Processes: Reading the isotopic code: American Geophysical Union, Geophysical Monograph*, v. 95, p. 343–353.
- Lawrence, L.J., 1968, The mineralogy and genetic significance of a Consols-type vein, *In The Main Lode Horizon, Broken Hill, N.S.W.: Proceedings of the Australasian Institute of Mining and Metallurgy*, No. 226, Pl. 1, p. 47–57.
- Lindsey, D. A., 1967, The sedimentology of the Huronian Gowganda Formation, Ontario: Unpublished Ph.D. thesis, Baltimore, United States of America, The Johns Hopkins University.
- Lindsey, D.A., 1969, Glacial sedimentation of the Precambrian Gowganda Formation, Ontario, Canada: *Geologic Society of America Bulletin*, v. 80, p. 1685–1704.

- London, D., 2008, Pegmatites, Special Publication 10, Mineralogical Association of Canada, 347 p.
- London, D., 2009, The origin of primary textures in granitic pegmatites, *Canadian Mineralogist*, v. 47, p. 697–724.
- Lovell, H.L., and Caine, T.W., 1970, Geology of South Lorrain Township: Ontario Department of Mines and Northern Affairs, Geological Report 83, 95 p.
- Maneta, V. and Baker, D.R., 2014, Exploring the effect of lithium on pegmatite textures: An experimental study. *American Mineralogist*, v. 99, p. 1383-1403.
- Markl, G., Burisch, M., Neumann, U., 2016, Natural fracking and the genesis of five- element veins: *Minerallium Deposita*, v. 51(6), p. 703–712.
- Marshall, D., 2008, Economic Geology Models 2. Melt inclusions of native silver and native bismuth: A re-examination of possible mechanisms for metal enrichment in five-element deposits, *Geoscience Canada*, v. 35, p. 137-145.
- Marshall, D., and Watkinson, D.H., 2000, The Cobalt Mining District: silver sources, transport and deposition: *Exploration and Mining Geology*, v. 9, No. 2, p. 81–90.
- Marshall, D.D., Diamond, L.W., and Skippen, G.B., 1993, Silver transport and deposition at Cobalt, Ontario, Canada; fluid inclusion evidence: *Economic Geology*, v. 88, p. 837–854.
- Maslennikov, V.V., and Large, R.R., 2021. Editorial for Special Issue “Pyrite varieties and LA-ICP-MS geochemistry in ore genesis and exploration”, *Minerals*, v. 11, 131.
- Mathieu, J., Kontak, D.J., Turner, E.C., Fayek, M. and Layne, G., 2015, In situ SIMS (O, S) and LA ICP-MS (trace elements) micro-analysis of multiple cement phases reveal a complex diagenetic fluid history: A case study of Phanerozoic cements on Victoria Island, NWT, *Chemical Geology*, v. 415, p. 47-69.
- Mavrogenes, J.A., and Bodnar, R.J., 1994, Hydrogen movement into and out of fluid inclusions in quartz: Experimental evidence and geologic implications: *Geochimica et Cosmochimica. Acta*, v. 58, p. 141-148.

- Mavrogenes, J., Frost, R., and Sparks, H.A., 2013, Experimental evidence of sulfide melt evolution via immiscibility and fractional crystallization, *The Canadian Mineralogist*, v. 51, p. 841-850.
- Mernagh, T.P., Heinrich, C.A., and Mikucki, E.J., 2004, Temperature gradients recorded by fluid inclusions and hydrothermal alteration at the Mount Charlotte gold deposit, Kalgoorlie, Australia, *The Canadian Mineralogist*, v. 42, p. 1383-1403.
- Miller, W.G., 1913, *The Cobalt-Nickel Arsenides and Silver Deposits of Timiskaming: Ontario Bureau of Mines*, v. 19, pt. 2.
- Möller, P., and Morteani, G., 1983, On the geochemical fractionation of rare earth elements during the formation of Ca-minerals and its application to problems of the genesis of the ore deposits, *In The Significance of Trace Elements in Solving Petrogenetic Problems and Controversies* (S.S. Augustithis, ed.). Theophrastus Publ. S.A., Athens, Greece (p. 747-791).
- Moncada, D., Baker, D., Bodnar, R.J., 2017, Mineralogical, petrographic and fluid inclusion evidence for the link between boiling and epithermal Ag-Au mineralization in the La Luz area, Guanajuato Mining District, México, *Ore Geology Reviews*, v. 89, p. 143-170.
- Moncada, D., Mutchler, S., Nieto, A., Reynolds, T.J., Rimstidt, J.D., Bodnar, R.J., 2012, Mineral textures and fluid inclusion petrography of the epithermal Ag-Au deposits at Guanajuato, Mexico: application to exploration, *J. Geochem. Explor.*, v. 114, p. 20-35.
- Monecke, T., Mercier-Langevin, P., Dubé, B., and Frieman, B.M., 2017, Geology of the Abitibi Greenstone Belt, *Reviews in Economic Geology*, v. 19, p. 7-49.
- Montsion, R.M., Thurston, P., Ayer, J., 2018, 1:2 000 000 Scale Geological Compilation of the Superior Craton - Version 1: Mineral Exploration Research Centre, Harquail School of Earth Sciences, Laurentian University Document Number MERC-ME-2018-017
- Moore, E.S., 1956, *Geology of the Miller Lake portion of the Gowganda Silver Area: Ontario Department of Mines*, v. 64, pt. 5, p. 1-37.
- Müller, H., 1860, *Der Erzdistrict von Schneeberg im Erzgebirge: Cotta's Gangstud.* v. 3, p. 1-223.

- Naumov, G.B., Motorina, Z.M., and Naumov, V.B., 1971a, Conditions of formation of carbonates in veins of the lead-cobalt-nickel-silver-uranium type (translation from *Geokhimiya*, No 8, p. 938–948): *Geochemistry International*, v. 8, 590–598.
- Nichols, R. S., 1988, Archean geology and silver mineralization controls at Cobalt, Ontario. *CIM Bulletin*, v. 81, p. 40–48.
- Ohmoto, H., Lasaga, A.C., 1982, Kinetics of reactions between aqueous sulfates and sulfides in hydrothermal systems. *Geochim. Cosmochim. Acta*, v. 46, p. 1727–1745.
- Ohmoto, H. and Rye, R.O., 1979, Isotope of sulfur and carbon, *In* Barnes, H.L.Ed., *Geochemistry of Hydrothermal deposits*, John Wiley & Sons, p. 509-567.
- Owsiacki, L., 1982, Geology of Lundy Township (northern half), District of Timiskaming, *In* Summary of fieldwork, 1982, by the Ontario Geologic survey, *Edited by* J. Wood, O.L. White, R.B. Barlow, and A.C. Colvine: Ontario Geological Survey, Miscellaneous Paper 100, p. 214–217.
- Paton, C., Hellstrom, J., Paul, B., Woodhead, J. and Hergt, J., 2011, Iolite: Freeware for the visualisation and processing of mass spectrometric data. *Journal of Analytical Atomic Spectrometry*.
- Patterson, G.C., 1979, No. 521 Metallogenic relationships of base-metal occurrences in the Cobalt area: Ontario Geologic Survey, Miscellaneous Paper 90.
- Percival, J.A., Skulski, T., Sanborn-Barrie, M., Stott, G.M., Leclair, A.D., Corkery, M.T., and Boily, M., 2012, Geology and tectonic evolution of the Superior Province, Canada, Chapter 6, *In* Tectonic Styles in Canada: The LITHOPROBE Perspective, *Edited by* J.A. Percival, F.A. Cook, and R.M. Clowes: Geological Association of Canada, Special Paper 49, p. 321–378.
- Petrella, L., Thébaud, N., Fougereuse, D., Evans, K., Quadir, Z., and Laflamme, C., 2020, Colloidal gold transport: a key to high-grade gold mineralization?, *Mineralium Deposita*, v. 55, p. 1247-1254.
- Petruk, W., 1968, Mineralogy and origin of the Silverfields silver deposit in the Cobalt area, Ontario, *Economic Geology*, v. 63, p. 512-531.

- Petruk, W., 1971a, General characteristics of the deposits, *In* The silver-arsenide deposits of the Cobalt-Gowganda region, Ontario, *Edited by* L.G. Berry: *The Canadian Mineralogist*, v. 11, p. 76–107.
- Petruk, W., 1971b, Mineralogical characteristics of the deposits and textures of the ore minerals, *In* The silver-arsenide deposits of the Cobalt-Gowganda region, Ontario, *Edited by* L.G. Berry: *The Canadian Mineralogist*, v. 11, part 1, p. 108–139.
- Petruk, W., 1971c, Geochemistry of the ores, *In* The silver-arsenide deposits of the Cobalt-Gowganda region, Ontario, *Edited by* L.G. Berry: *The Canadian Mineralogist*, v. 11, part 1, p. 140-149.
- Petruk, W., Harris, D.C., and Stewart, J.M., 1971a, Characteristics of the arsenides, sulpharsenides, and antimonides, *In* The silver-arsenide deposits of the Cobalt-Gowganda region, Ontario, *Edited by* L.G. Berry: *The Canadian Mineralogist*, v. 11, part 1, p. 150-186.
- Petruk, W., Harris, D.C., Cabri, L.J., and Stewart, J.M., 1971b, Characteristics of the silver-antimony minerals, *In* The silver-arsenide deposits of the Cobalt-Gowganda region, Ontario, *Edited by* L.G. Berry: *The Canadian Mineralogist*, v. 11, part 1, p. 187-195.
- Potter, E.G., and Taylor, R.P., 2009, The lead isotope composition of ore minerals from precious metal-bearing polymetallic vein systems in the Cobalt Embayment, Northern Ontario: metallogenic implications: *Economic Geology*, v. 104, p. 869–879.
- Potter, E.G., and Taylor, R.P., 2010, The stable and radiogenic isotopic attributes of precious-metal-bearing polymetallic veins from the Cobalt Embayment, northern Ontario, Canada: Genetic and exploration implications: *The Canadian Mineralogist*, v. 48, p. 391–414.
- Poulin, R., Kontak, D.J., McDonald, A., and McClenaghan, M.B., 2018, Trace element chemistry of scheelite and its applications as an ore deposit discriminator, *Canadian Mineralogist*, v. 56, p. 265-302.
- Robinson, B., 1984, General geology of the Beaver-Temiskaming mine, Cobalt, Ontario: Geological Association of Canada, Joint Annual Meeting, London, Ontario, Fieldtrip Guidebook 4, p. 17–29.

- Robinson, B., and Ohmoto, H., 1973, Mineralogy, fluid inclusions, and stable isotopes of the Echo Bay U-Ni-Ag-Cu deposits, Northwest Territories, Canada: *Economic Geology*, v. 68, p. 635–656.
- Roedder, E., 1984, Fluid inclusions: *Rev. Mineralogy*, v. 12, 644 p.
- Rollinson, H.R., 1993, *Using geochemical data: evaluation, presentation, interpretation*, Harlow :Longman Scientific & Technical.
- Ruiz-Agudo, E., Putnis, C.V., and Putnis, A., 2014, Coupled dissolution and precipitation at mineral-fluid interfaces, *Chemical Geology*, v. 383, p. 132-146.
- Rusk, B., and Reed, M., 2002, Scanning electron microscope-cathodoluminescence analysis of quartz reveals complex growth histories in veins from the Butte porphyry copper deposit, Montana, *Geology*, v. 30, p. 727-730.
- Sampson, E., and Hriskevich, M.E., 1957, Cobalt arsenide minerals associated with aplites at Cobalt, Ontario: *Economic Geology*, v. 52, p. 60-75.
- Sander, M.V., and Black, J.E., 1988, Crystallization and recrystallization of growth-zoned vein quartz crystals from epithermal systems – implications for fluid inclusion studies, *Economic Geology*, v. 83, p. 1052-1060.
- Saunders, J.A., and Burke, M., 2017, Formation and aggregation of gold (electrum) nanoparticles in epithermal ores, *Minerals*, v. 7, 163 p.
- Saunders, J.A., Unger, D.L., Kamenov, G.D., Fayek, M., Hames, W.E., and Utterback, W.C., 2008, Genesis of middle Miocene Yellowstone hot-spot-related bonanza epithermal Au-Ag deposits, Northern Great Basin, USA, *Mineralium Deposita*, v. 43, p. 715-734.
- Scharrer, M.S., Kreissl, S.B., and Markl, G.A., 2019, The mineralogical variability of hydrothermal native element-arsenide (five element) associations and the role of physicochemical and kinetic factors concerning sulfur and arsenic: *Ore Geology Reviews*, v. 113 (2019) 103025, p. 1–28.
- Scott, S.D., 1972, The Ag-Co-Ni-As ores of the Siscoe Metals of Ontario mine, Gowganda, Ontario, Canada: *Proceedings, 24th International Geological Congress, Montreal, Sec. 4*, p. 528–538.

- Scott, S.D., and O'Connor, T.P., 1971, Fluid inclusions in vein quartz, Silverfields mine, *In* The silver-arsenide deposits of the Cobalt-Gowganda region, Ontario, *Edited by* L.G. Berry. *The Canadian Mineralogist*, v. 11, p. 263–271.
- Sergiades, A.O., 1968, Silver Cobalt Calcite Vein Deposits of Ontario: Ontario Department of Mines, Mineral Resources Circular No. 10, 498 p.
- Shannon, R.D., 1976, Revised effective ionic radii and systematic studies of interatomic distances in halides and chalcogenides. *Acta Crystallographica Section A: Crystal Physics, Diffraction, Theoretical and General Crystallography*, v. 32, p. 751–767.
- Sibson, R.H., Robert, F., and Poulsen, K.H., 1988, High-angle reverse faults, fluid-pressure cycling, and mesothermal gold-quartz deposit, *Geology*, v. 16, p. 551-555.
- Silver, L.T., and Green, J. C., 1972, Time constants for Keweenawan igneous activity. *Geological Society of America, Abstracts with Programs*, v. 4, p. 665-666.
- Sirbescu, M.L.C., Schmidt, C., and Veksler, I.V., 2017, Experimental crystallization of undercooled felsic liquids: Generation of pegmatitic texture, *Journal of Petrology*, v. 58, p. 539-568.
- Slater, E., Kontak, D.J., and McDonald, A., 2021, Origin of a Miocene multi-stage epithermal Ag-Zn-Pb-Sn deposit: The Cortaderas breccia body, Pirquitas Mine, NW Argentina, *Mineralium Deposita*, v. 56, p. 381-406.
- Smith, M.D., and Heaman, L.M., 1999, Constraints on the timing of felsic magmatism associated with the Matachewan igneous events: preliminary results for the Creighton granite, Ontario [abs.]: Geological Association of Canada-Mineralogical Association of Canada Joint Meeting, Program with Abstracts, v. 24, 119 p.
- Smyk, M. C., 1987, Geology of Archean interflow sedimentary rocks and their relationship to Ag-Bi-Co-Ni-As veins, Cobalt area, Ontario, Unpublished M.Sc. thesis, Ottawa, Canada, Carleton University.
- Smyk, M.C., and Watkinson, D.H., 1990, Sulphide remobilization in Archean volcano-sedimentary Proterozoic silver vein genesis, Cobalt, Ontario: *Canadian Journal of Earth Science*, v. 27, p. 1170–1181.

- Sun, S., and McDonough, W.F., 1989, Chemical and isotopic systematics of oceanic basalts, *In* Saunders, A.D., and Norry, M.J., eds., *Magmatism in the ocean basins: Geological Society of London Special Publication 42*, p. 313-345.
- Symons, D.T.A., 1970, Paleomagnetism of the Nipissing diabase, Cobalt area, Ontario: *Canadian Journal of Earth Sciences*, v. 72, p. 86–90.
- Tomkins, A.G., and Mavrogenes, J.A., 2002, Mobilization of gold as a polymetallic melt during pelite anatexis at the Challenger gold deposit, South Australia: A metamorphosed Archean deposit: *Economic Geology*, v. 97, p. 1249–1271.
- Tomkins, A.G., Pattison, D.R., and Zaleski, E., 2004, The Hemlo Gold Deposit, Ontario: An example of melting and mobilization of a precious metal-sulfosalt assemblage during amphibolite facies metamorphism and deformation. *Economic Geology*, v. 99, p. 1063-1084.
- Tomkins, A.G., Pattison, D.R., and Frost, B.R., 2007, On the initiation of metamorphic sulfide anatexis, *Journal of Petrology*, v. 48(3), p. 511–535.
- Thomson, R., 1957a., *The Proterozoic of the cobalt area: Royal Society of Canada, The Proterozoic in Canada, Special Publication 2*, p. 40–45.
- Thomson, R., 1964a, Cobalt silver area, northern sheet, Timiskaming district: Ontario Department of Mines, Map 2050.
- Thomson, R., 1967, Cobalt and District. Canadian Institute of Mining and Metallurgy (CIM). Centennial Field Excursion, Northwestern Quebec-Northern Ontario, p. 136-143.
- Thorpe, R., 1974, Lead isotope evidence on the genesis of the silver-arsenide vein deposits of the Cobalt and Great Bear Lake areas, Canada: *Economic Geology*, v. 69, p. 777-791.
- Thorpe, R.I., Goodz, M.D., Jonasson, I.R., and Blenkinsop, J., 1986, Lead-isotope study of mineralization in the Cobalt district, Ontario: *Canadian Journal of Earth Sciences*, v. 23, p. 1568–1575.
- Thurston, P.C., 2002, Autochthonous development of Superior Province greenstone belts?: *Precambrian Research*, v. 115, p. 11–36.

- Thurston, P.C., and Chivers, K.M., 1990, Secular variation in greenstone sequence development emphasizing Superior province, Canada: *Precambrian Research*, v. 46, p. 21–58.
- Thurston, P.C., Ayer, J.A., Goutier, J., and Hamilton, M.A., 2008, Depositional gaps in Abitibi greenstone belt stratigraphy: a key to exploration for syngenetic mineralization: *Economic Geology*, v. 103, p. 1097–1134.
- Tooth, B., Brugger, J., Ciobanu, C., and Liu, W., 2008, Modeling of gold scavenging by bismuth melts coexisting with hydrothermal fluids, *Geology*, v. 36, p. 815-818.
- Tooth, B., Ciobanu, C., Green, L., and O'Neill, B.O., Bi-melt formation and gold scavenging from hydrothermal fluids: An experimental study, *Geochimica et Cosmochimica Acta*, v. 75, p. 5423-5443.
- Van den Kerkhof, A., and Thiéry, R., 2001, Carbonic inclusions, *Lithos*, v. 55, 49–68.
- Voisey, C.R., Willis, D., Tomkins, A.G., Wilson, C.J.L., Micklethwaite, S., Salvemini, F., Bougoure, J., and Rickard, W.D.A., 2020, Aseismic refinement of orogenic gold systems, *Economic Geology*, v. 115, p. 33-50.
- White, S.E., 2019, Structure and stratigraphy of the Archean basement near Cobalt, Ontario, Ontario Geological Survey, Open File Report 6360, 428, p. 29-1 to 29-9.
- Wilson, J., 1949, Some major structures of the Canadian Shield: *Transactions of the Canadian Institute of Mining and Metallurgy*, v. 52, p. 231–242.
- Woodhead, J., Hellstrom, J., Hergt, J., Greig, A. & Maas, R., 2007, Isotopic and elemental imaging of geological materials by laser ablation Inductively Coupled Plasma mass spectrometry. *Journal of Geostandards and Geoanalytical Research*, 31, p. 331-343.
- Wykes, J.L., and Mavrogenes, J.A., 2005, Hydrous sulfide melting: Experimental evidence for the solubility of H₂O in sulfide melts: *Economic Geology*, v. 100, p. 157-164.
- Zhong, S., and Mucci, A., 1995, Partitioning of rare earth elements (REEs) between calcite and seawater solutions at 25°C and 1 atm, and high dissolved REE concentrations, *Geochimica et Cosmochimica Acta*, v. 59, p. 443-453.

Tables

Table 1. Mineral abbreviations. Note that all arsenides and sulfarsenides contain Ni, Co, and Fe substitution in their chemical formula.

Mineral	Abbreviation	Chemical formula	Mineral	Abbreviation	Chemical formula
Acanthite	Aca	Ag ₂ S	Hematite	Hmt	Fe ₂ O ₃
Actinolite	Act	Ca ₂ Si ₈ O ₂₂ (OH) ₂	Loellingite	Lo	FeAs ₂
Alkali feldspar	Afs	(K,Na)AlSi ₃ O ₈	Native bismuth	Bi	Bi
Arsenopyrite	Apy	FeAsS	Native silver	Ag	Ag
Bismuthinite	Bis	Bi ₂ S ₃	Nickeline	Nic	NiAs
Bornite	Bn	Cu ₅ FeS ₄	Ni-skutterudite	Ni-skutt	(Ni,Co,Fe)As ₃
Calcite	Cal	CaCO ₃	Plagioclase	Plg	(Na,Ca)(Si,Al) ₄ O ₈
Carbonate	Cb	X _Y CO ₃ (Z)	Pyrite	Py	FeS ₂
Chalcopyrite	Cp	CuFeS ₂	Pyroxene	Px	XYT ₂ O ₆
Chlorite	Chl	(Fe,Mg,Al) ₆ (Si,Al) ₄ O ₁₀ (OH) ₈	Pyrrhotite	Po	Fe _(1-x) S
Cobaltite	Cob	CoAsS	Quartz	Qtz	SiO ₂
Cubanite	Cub	CuFe ₂ S ₃	Rammelsbergite	Ram	NiAs ₂
Dolomite	Dol	CaMg(CO ₃) ₂	Safflorite	Saff	CoAs ₂
Epidote	Ep	(Ca,Mn) ₂ (Al,Fe) ₃ (SiO ₄)(Si ₂ O ₇)O(OH)	Skutterudite	Skutt	CoAs ₃
Galena	Gn	PbS	Sphalerite	Sp	ZnS
Gersdorffite	Ger	NiAsS			

Table 2. Representative SEM-EDS raster data for bulk native silver-arsenide pods, Ag dendrites in pod cores (see Fig. 11). The following data are averages and one standard deviation in at. % and wt. %. Detection limit is 0.1 wt. %.

		Pod average and 1 Std Dev	Ag dendrite average and 1 Std Dev
Ag	(at. %)	11.8 ± 1.2	91.0 ± 1.5
	(wt. %)	17.3 ± 37.8	92.6 ± 40.5
As	(at. %)	59.1 ± 1.3	1.8 ± 1.1
	(wt. %)	59.8 ± 58.7	1.3 ± 20.7
Bi	(at. %)	<0.1 ± <0.1	<0.1 ± <0.1
	(wt. %)	0.1 ± 0.7	0.0 ± 1.4
Co	(at. %)	18.6 ± 0.8	0.1 ± 0.1
	(wt. %)	14.8 ± 13.4	0.1 ± 1.5
Cu	(at. %)	0.5 ± 0.1	0.4 ± 0.5
	(wt. %)	0.4 ± 2.1	0.2 ± 7.6
Fe	(at. %)	5.2 ± 0.3	0.2 ± 0.1
	(wt. %)	4.0 ± 4.1	0.1 ± 2.3
Ni	(at. %)	1.5 ± 0.1	0.5 ± 0.4
	(wt. %)	1.2 ± 1.7	0.3 ± 5.8
S	(at. %)	2.2 ± 0.7	1.6 ± 0.1
	(wt. %)	1.0 ± 6.5	0.5 ± 0.9
Sb	(at. %)	0.9 ± 0.1	4.1 ± 0.4
	(wt. %)	1.5 ± 2.8	4.7 ± 12.3
Te	(at. %)	<0.1 ± <0.1	0.1 ± 0.1
	(wt. %)	0.1 ± 1.2	0.1 ± 2.7
Zn	(at. %)	0.1 ± 0.1	0.3 ± 0.3
	(wt. %)	0.1 ± 1.1	0.2 ± 4.5

Table 3. Representative SEM-EDS spot analysis data for five-element vein arsenide and sulfarsenide minerals in at. % and wt. %. Horizontal headings refer to representative minerals analyzed, with reference to Figures 12 (number for analysis is labeled). Detection limit (DL) is 0.1 for both at. % and wt. %.

		1) Apy 1	2) Apy 2	3) Apy 3	4) Cob 1	5) Cob 2	6) Cob 3	7) Ger 1	8) Ger 2	9) Ger 3
Ag	(at. %)	<DL	<DL	<DL	<DL	<DL	<DL	<DL	<DL	<DL
	(wt. %)	<DL	<DL	<DL	<DL	<DL	<DL	<DL	<DL	0.1
As	(at. %)	35.7	41.6	38.1	33.6	39.6	36.5	50.9	39.5	40.4
	(wt. %)	46.6	53.4	49.6	44.1	50.8	41.3	60.7	50.7	51.6
Bi	(at. %)	<DL	0.2	<DL	0.3	0.2	0.2	0.2	0.2	<DL
	(wt. %)	<DL	0.7	<DL	1.0	0.8	0.7	0.5	0.7	<DL
Co	(at. %)	0.3	4.7	14.9	29.9	21.8	10.9	2.8	7.0	10.2
	(wt. %)	0.3	4.7	15.3	30.9	22.0	9.7	2.7	7.1	10.3
Cu	(at. %)	0.1	<DL	<DL	<DL	<DL	0.1	<DL	<DL	0.5
	(wt. %)	0.1	<DL	<DL	<DL	<DL	0.1	<DL	<DL	0.5
Fe	(at. %)	35.2	28.6	14.2	0.4	4.7	1.5	1.5	5.2	7.1
	(wt. %)	34.3	27.4	13.8	0.3	4.4	1.3	1.3	4.9	6.7
Ni	(at. %)	<DL	0.1	0.8	3.9	7.4	8.8	28.3	21.5	12.2
	(wt. %)	<DL	0.1	0.8	4.0	7.4	7.8	26.5	21.6	12.2
S	(at. %)	27.6	24.8	31.0	31.0	26.4	28.4	16.3	26.6	28.9
	(wt. %)	15.4	13.6	17.2	17.4	14.5	13.7	8.3	14.7	15.8
Sb	(at. %)	<DL	0.1	0.1	1.0	<DL	4.6	<DL	0.1	<DL
	(wt. %)	<DL	0.1	0.1	2.2	<DL	8.5	<DL	0.2	<DL
Te	(at. %)	<DL	<DL	<DL	<DL	<DL	8.7	<DL	<DL	<DL
	(wt. %)	<DL	<DL	0.1	<DL	<DL	16.7	<DL	<DL	<DL
Zn	(at. %)	0.2	<DL	0.2	<DL	<DL	0.3	<DL	<DL	<DL
	(wt. %)	0.2	<DL	0.2	<DL	<DL	0.3	<DL	<DL	<DL
		10) Lo 1	11) Lo 2	12) Lo 3	13) Nic 1	14) Nic 2	15) Nic 3	16) Ni-skutt 1	17) Ni-skutt 2	18) Ni-skutt 3
Ag	(at. %)	<DL	0.1	0.1	<DL	<DL	0.1	<DL	<DL	<DL
	(wt. %)	<DL	0.2	0.1	<DL	0.1	0.1	<DL	<DL	<DL
As	(at. %)	65.3	67.7	65.8	38.7	40.8	43.9	69.0	71.8	71.1
	(wt. %)	71.7	73.3	71.3	43.9	45.2	49.2	73.9	76.4	75.9

Bi	(at. %)	<DL	<DL	0.1	<DL	0.2	<DL	<DL	<DL	<DL
	(wt. %)	0.1	<DL	0.2	<DL	0.7	<DL	<DL	<DL	0.1
Co	(at. %)	1.0	4.7	10.0	0.6	0.8	17.2	2.2	6.5	8.4
	(wt. %)	0.9	4.0	8.5	0.5	0.7	15.2	1.8	5.4	7.1
Cu	(at. %)	<DL	0.3	<DL	0.3	0.3	<DL	1.7	<DL	0.1
	(wt. %)	<DL	0.3	<DL	0.3	0.3	<DL	1.5	<DL	0.1
Fe	(at. %)	31.9	21.2	12.5	0.4	0.3	0.3	0.3	0.1	0.7
	(wt. %)	26.2	17.1	10.1	0.4	0.2	0.2	0.2	0.1	0.6
Ni	(at. %)	<DL	5.5	10.6	58.0	54.9	37.0	25.6	20.3	18.2
	(wt. %)	<DL	4.6	9.0	51.5	47.7	32.5	21.5	17.0	15.2
S	(at. %)	1.3	0.4	0.6	0.4	<DL	0.1	0.7	1.0	1.0
	(wt. %)	0.6	0.2	0.3	0.2	<DL	<DL	0.3	0.4	0.4
Sb	(at. %)	0.1	0.1	<DL	1.1	2.6	0.4	0.2	0.1	0.2
	(wt. %)	0.2	0.1	<DL	2.1	4.7	0.8	0.3	0.2	0.3
Te	(at. %)	0.1	<DL	0.1	0.6	0.2	1.0	0.1	<DL	<DL
	(wt. %)	0.1	<DL	0.2	1.2	0.4	2.0	0.1	<DL	<DL
Zn	(at. %)	0.3	0.2	0.2	<DL	<DL	<DL	0.3	<DL	0.3
	(wt. %)	0.3	0.1	0.2	<DL	<DL	<DL	0.3	<DL	0.3
		19) Ram 1	20) Ram 2	21) Ram 3	22) Saff 1	23) Saff 2	24) Saff 3	25) Skutt 1	26) Skutt 2	27) Skutt 3
Ag	(at. %)	<DL	<DL	<DL	<DL	<DL	<DL	<DL	<DL	0.3
	(wt. %)	<DL	<DL	<DL	0.2	<DL	<DL	<DL	<DL	0.4
As	(at. %)	62.7	64.8	65.5	65.7	65.2	69.4	70.0	69.0	73.5
	(wt. %)	69.4	70.7	71.1	71.1	70.8	74.7	74.3	74.3	76.2
Bi	(at. %)	<DL	<DL	0.1	<DL	<DL	<DL	<DL	0.1	1.2
	(wt. %)	0.1	<DL	0.2	<DL	<DL	<DL	<DL	0.4	3.4
Co	(at. %)	0.5	1.2	9.0	27.4	18.9	10.6	24.0	17.1	13.4
	(wt. %)	0.5	1.0	7.7	23.3	16.1	9.0	20.0	14.5	11.0
Cu	(at. %)	<DL	1.8	0.1	<DL	<DL	<DL	<DL	0.1	<DL
	(wt. %)	<DL	1.7	0.1	<DL	<DL	<DL	<DL	0.1	<DL
Fe	(at. %)	0.3	0.2	1.0	4.8	14.2	9.5	2.9	2.4	4.3
	(wt. %)	0.2	0.2	0.8	3.9	11.5	7.6	2.3	1.9	3.3

Ni	(at. %)	30.6	27.5	22.8	1.4	0.2	9.7	0.8	8.9	0.2
	(wt. %)	26.5	23.5	19.4	1.2	0.2	8.2	0.7	7.5	0.1
S	(at. %)	5.5	3.4	1.7	0.5	0.8	0.7	1.0	2.2	5.8
	(wt. %)	2.6	1.6	0.8	0.2	0.4	0.3	0.5	1.0	2.6
Sb	(at. %)	0.4	0.3	<DL	0.2	0.5	0.1	1.2	0.2	0.1
	(wt. %)	0.7	0.5	<DL	0.3	0.8	0.1	2.1	0.4	0.1
Te	(at. %)	<DL	<DL	<DL	0.1	0.1	<DL	<DL	<DL	0.2
	(wt. %)	<DL	<DL	<DL	0.1	0.1	<DL	0.1	<DL	0.3
Zn	(at. %)	<DL	0.8	<DL	<DL	0.1	<DL	<DL	<DL	0.2
	(wt. %)	<DL	0.7	<DL	<DL	0.1	<DL	<DL	<DL	0.2

Table 4. Representative SEM-EDS spot analysis data for five-element vein late remobilized Ag blebs and acanthite, arsenide-hosted Bi blebs, late remobilized Bi and bismuthinite with respect to Figure 13. Data is presented in atomic % (at. %) and weight % (wt. %) with detection limit of 0.1 for at. % and wt. %.

		Late Native Ag Avg	Late Native Ag Standard Dev	Aca Avg	Aca Standard Dev	Vein native Bi bleb Avg	Vein native Bi bleb Standard Dev	Late Native Bi Avg	Late Native Bi Standard Dev	Bis Avg	Bis Standard Dev
Ag	(at. %)	91.6	3.1	67.7	3.1	<DL	<DL	<DL	<DL	0.3	0.3
	(wt. %)	91.3	47.7	83.8	55.8	<DL	<DL	<DL	<DL	0.3	1.0
As	(at. %)	0.8	0.4	5.3	1.3	7.2	6.6	5.2	7.6	6.7	5.4
	(wt. %)	0.6	0.9	4.5	16.2	3.0	17.5	2.1	16.7	4.2	12.1
Bi	(at. %)	1.4	5.6	<DL	<DL	80.5	8.5	86.8	11.5	45.6	10.5
	(wt. %)	2.9	32.5	<DL	<DL	93.5	63.0	95.8	70.1	80.8	65.7
Co	(at. %)	0.1	0.1	2.1	0.4	3.7	2.9	2.5	2.9	2.4	1.8
	(wt. %)	0.1	0.2	1.4	4.0	1.2	6.0	0.8	5.0	1.2	3.3
Cu	(at. %)	0.2	0.3	0.3	0.1	0.3	0.6	0.2	0.4	0.1	0.1
	(wt. %)	0.1	0.5	0.2	0.9	0.1	1.4	0.1	0.7	0.1	0.3
Fe	(at. %)	0.3	0.4	2.1	0.1	3.0	2.4	0.6	0.7	0.9	1.0
	(wt. %)	0.2	0.6	1.3	1.1	0.9	4.7	0.2	1.2	0.4	1.6
Ni	(at. %)	0.2	0.2	0.3	0.1	0.6	0.5	1.4	1.8	3.9	2.2
	(wt. %)	0.1	0.3	0.2	0.8	0.2	1.1	0.4	3.2	2.0	3.8
S	(at. %)	7.0	10.7	22.1	3.7	3.8	1.5	2.7	1.2	39.5	11.1
	(wt. %)	2.2	9.6	8.1	19.7	0.9	1.7	0.5	0.1	10.7	10.7
Sb	(at. %)	2.0	2.0	0.2	<DL	0.2	0.2	0.1	0.1	0.1	0.1
	(wt. %)	2.3	6.7	0.2	0.3	0.1	0.7	0.1	0.5	0.1	0.3
Te	(at. %)	0.2	0.2	0.1	<DL	0.1	0.1	0.1	0.2	0.1	0.2
	(wt. %)	0.2	0.6	0.2	0.8	0.1	0.5	0.1	0.5	0.1	0.7
Zn	(at. %)	0.2	0.3	<DL	<DL	0.6	1.5	0.3	0.6	0.2	0.3
	(wt. %)	0.1	0.5	<DL	0.3	0.2	3.4	0.1	1.1	0.1	0.6

Table 5. Elemental ranges of five-element vein assay values by weight (ppm).

Element	Minimum (ppm)	Maximum (ppm)	Element	Minimum (ppm)	Maximum (ppm)
Ag	<1.0	22,100	Fe	2000	331,000
As	<30	467,697	Mo	0.6	3,030
Au	<0.1	22	Ni	10	213,000
Bi	<0.1	51,900	Pb	0.8	61,800
Co	2.4	165,500	S	<100	328,000
Cu	1.7	81,955	Sb	<0.1	10,600
Hg	0.2	70	Zn	<2.0	40,100

Table 6. Representative five-element vein assay data for five-element vein Ag and arsenide mineral groupings by weight (ppm). Representative samples were chosen to illustrate variance of elemental abundance in non-stoichiometric minerals. Horizontal headings refer to representative mineral groupings with respect to Figures 14 – 19. The vertical headings refer to the elemental abundance detected in each of the representative samples. Detection limits are element-specific and available in Appendix B.

	1) Ag	2) Ag	3) Ag	4) As	5) As	6) CoAs	7) CoAs	8) CoAs	9) CoAs ₂
Ag (ppm)	18950	1495	2890	158	54	8.0	39	292	15
As (ppm)	28100	147500	27500	290000	66100	174000	8280	52300	300000
Au (ppm)	0.05	0.004	0.001	0.104	2.320	2.700	0.012	0.010	0.014
Bi (ppm)	270	840	20	100	780	3060	240	200	3590
Co (ppm)	29700	30700	6590	7160	4070	93100	5000	26800	134500
Cu (ppm)	30	2750	470	30	340	30	20	2500	70
Fe (ppm)	40100	40300	69700	226000	53900	52200	25400	34200	80000
Mo (ppm)	260	10	40	10	10	130	30	130	40
Ni (ppm)	76400	4820	290	3300	110	23100	510	5080	28200
Pb (ppm)	30	4.7	50	350	9940	14.5	100	150	100
S (ppm)	13900	1800	8000	139000	37300	62300	3700	22700	14600
Sb (ppm)	6780	990	800	80	50	80	50	170	2050
Zn (ppm)	80	40	70	30	11850	20	50	40	130
	10) CoAs ₂	11) CoAs ₂	12) CoAs ₃	13) CoAs ₃	14) CoAs ₃	15) NiAs	16) NiAs	17) NiAs	18) NiAs ₂
Ag (ppm)	26	16	140	6.0	80	2.0	537	12	2.0
As (ppm)	300000	92500	101500	159000	300000	24400	29600	300000	49500
Au (ppm)	0.014	0.001	0.001	0.124	0.494	0.064	0.036	0.001	4.500
Bi (ppm)	3280	170	20	3480	540	3300	1240	660	290
Co (ppm)	96600	29500	16050	39700	79400	2720	3900	47400	15700
Cu (ppm)	2280	70	480	10	80	3.4	9410	10	10
Fe (ppm)	23400	22200	87400	48200	20900	3000	25300	44900	37100
Mo (ppm)	3.2	20	250	10	10	0.7	50	20	70
Ni (ppm)	72500	180	110	2580	77000	14750	18800	165500	20200
Pb (ppm)	9.8	160	30	9.2	7.0	3.6	21600	6.8	10.6
S (ppm)	51200	5900	45600	29500	36000	2700	26300	14200	16600
Sb (ppm)	190	90	1070	140	340	70	180	2010	140

Zn (ppm)	4.0	20	60	20	9.0	2.0	950	2.0	20
	19) NiAs ₂	20) NiAs ₂	21) NiAs ₃	22) NiAs ₃	23) NiAs ₃				
Ag (ppm)	20	22	25	34	667				
As (ppm)	70200	680	176000	175000	285000				
Au (ppm)	0.020	0.010	0.009	0.217	0.289				
Bi (ppm)	370	8.4	90	7980	7970				
Co (ppm)	9930	190	33600	30800	63800				
Cu (ppm)	540	1470	10	10	310				
Fe (ppm)	74000	70500	34100	45900	32700				
Mo (ppm)	150	1.0	20	90	10				
Ni (ppm)	30600	230	55600	34100	111000				
Pb (ppm)	20	18050	20	3.6	340				
S (ppm)	23700	10900	36700	14200	82500				
Sb (ppm)	760	7.7	650	170	300				
Zn (ppm)	120	2760	60	30	30				

Table 7. Representative SEM-EDS spot analysis data for five-element vein dolomite and calcite with respect to Figure 21 in atomic % (at. %) and weight % (wt. %) with detection limit of 0.1 for at. % and wt. %.

		1) Dol Spectrum 1 (rhomb core)	2) Dol Spectrum 2 (rhomb rim)	Dol Average	Dol Standard Deviation	3) Cal Spectrum 1	4) Cal Spectrum 2	5) Cal Spectrum 3	Cal Average	Cal Standard Deviation
O	(at. %)	51.1	50.1	50.1	0.2	50.8	50.1	50.1	50.1	0.2
	(wt. %)	32.4	30.9	31.9	1.8	29.5	28.5	28.6	28.6	3.1
Na	(at. %)	<DL	<DL	<DL	<DL	<DL	<DL	<DL	<DL	0.1
	(wt. %)	<DL	<DL	<DL	<DL	<DL	<DL	<DL	<DL	1.8
Mg	(at. %)	15.6	16.3	19.8	1.6	1.1	0.1	0.1	0.2	0.2
	(wt. %)	15.0	15.2	19.1	24.4	1.0	0.1	0.1	0.1	5.5
Al	(at. %)	3.9	<DL	0.2	0.7	0.8	<DL	<DL	0.1	0.2
	(wt. %)	4.2	<DL	0.2	10.8	0.7	<DL	<DL	0.1	6.3
Si	(at. %)	0.2	0.1	0.1	<0.1	1.1	0.2	0.1	0.2	0.3
	(wt. %)	0.2	0.1	0.1	0.6	1.1	0.2	0.1	0.2	9.2
P	(at. %)	<0.1	<DL	<DL	<0.1	<DL	<DL	<DL	<DL	<0.1
	(wt. %)	0.1	<DL	<DL	0.2	<DL	<DL	<DL	<DL	0.6
S	(at. %)	<0.1	0.1	<DL	<0.1	0.1	<DL	<DL	<DL	<0.1
	(wt. %)	0.1	0.1	<DL	0.4	0.1	<DL	<DL	<DL	1.0
K	(at. %)	<DL	<DL	<DL	<0.1	<DL	<DL	<DL	<DL	0.1
	(wt. %)	<DL	<DL	<DL	0.1	<DL	<DL	<DL	<DL	3.4
Ca	(at. %)	26.3	29.8	28.2	1.1	45.3	48.8	49.7	48.9	0.8
	(wt. %)	41.9	46.0	45.0	27.2	65.9	69.5	71.0	70.0	38.1
Ti	(at. %)	<DL	<0.1	<DL	<0.1	<DL	<DL	<DL	<DL	<0.1
	(wt. %)	<DL	0.1	<DL	0.5	<DL	<DL	<DL	<DL	1.0
Mn	(at. %)	1.1	0.6	0.5	0.3	0.2	0.7	0.1	0.3	0.2
	(wt. %)	2.5	1.2	1.0	9.7	0.3	1.3	0.2	0.6	15.6
Fe	(at. %)	1.6	2.9	1.1	0.6	0.7	0.1	<0.1	0.1	0.1
	(wt. %)	3.5	6.3	2.4	21.1	1.4	0.1	0.1	0.2	6.3
Ni	(at. %)	0.1	<0.1	0.1	<0.1	<0.1	<DL	<DL	0.1	0.1
	(wt. %)	0.2	0.1	0.1	1.5	0.1	<DL	<DL	0.1	4.2
Y	(at. %)	<DL	<DL	<DL	<0.1	<DL	<DL	<DL	<DL	<0.1

	(wt. %)	<DL	<DL	<DL	0.5	<DL	<DL	<DL	<DL	1.2
Zr	(at. %)	<DL	<DL	<DL	<0.1	<DL	<DL	<DL	<DL	<0.1
	(wt. %)	<DL	<DL	<DL	0.3	<DL	<DL	<DL	<DL	0.7
La	(at. %)	<DL	<DL	<DL	<0.1	<DL	<0.1	<DL	<DL	<0.1
	(wt. %)	<DL	<DL	<DL	0.8	<DL	0.1	<DL	<DL	1.9

Table 8. LA-ICP-MS major, trace, and REE data of five-element vein dolomite and calcite with respect to Figures 21 and 22. Note to see additional information (e.g. detection limits) in Appendix E.

Sample Mineral Trend line	LR04G06A Calcite 1 Max REE	LR04G06A Calcite 1 Min REE	LR12G02 Calcite 1 Max REE	LR12G02 Calcite 1 Min REE	LR12G02 Calcite 2 Max REE	LR12G02 Calcite 2 Min REE	LR19G01 Dolomite Max REE
Mg (ppm)	951.4	60.8	2798.8	2215.2	478.5	775.6	118647.8
Ca (ppm)	547876	535374	532381	536451	535789	536611	280007
Mn (ppm)	5757.8	1454.7	17203.0	17434.1	6217.2	5947.6	8121.4
Fe (ppm)	2006.6	569.2	4593.0	4186.1	1043.7	1091.9	11576.6
Sr (ppm)	216.9	62.0	130.9	121.8	101.3	61.1	54.2
La (ppm)	618.44	0.03	209.28	0.40	115.07	0.91	34.41
Ce (ppm)	1239.94	0.11	557.59	0.80	274.97	1.62	82.33
Pr (ppm)	156.36	0.02	71.19	0.11	39.88	0.21	12.48
Nd (ppm)	615.25	0.09	300.66	0.77	202.08	1.19	62.92
Sm (ppm)	110.27	0.04	115.43	0.34	64.03	0.42	25.68
Eu (ppm)	1.02	<DL	13.89	0.74	10.66	0.11	2.36
Gd (ppm)	75.16	0.09	95.80	1.13	73.31	0.62	29.66
Tb (ppm)	8.41	0.05	10.84	0.25	9.30	0.14	4.02
Dy (ppm)	40.81	0.41	36.95	1.57	48.93	1.04	20.36
Ho (ppm)	7.36	0.18	4.69	0.40	7.62	0.20	3.32
Er (ppm)	19.67	0.82	8.36	1.22	15.93	0.63	7.26
Tm (ppm)	2.42	0.16	0.61	0.18	1.40	0.07	0.78
Yb (ppm)	16.46	1.58	4.12	0.93	5.80	0.53	4.52
Lu (ppm)	2.14	0.41	0.59	0.14	0.69	0.07	0.57
Eu Anomaly	<0.1	N/A	0.1	1.0	0.2	0.2	0.1
ΣREE (ppm)	2914	4	1430	9	870	8	291
(La/Lu)N	289.2	0.1	367.8	2.8	165.9	12.5	60.6
Sample Mineral Trend line	LR19G01 Dolomite Min REE	LR19G01 Calcite 1 Max REE	LR19G01 Calcite 1 Min REE	LR19G02 Calcite 1 Max REE	LR19G02 Calcite 1 Min REE	LR19G02 Calcite 2 Max REE	LR19G02 Calcite 2 Min REE
Mg (ppm)	126774.9	1111.3	3625.8	200.0	181.5	196.3	12.9
Ca (ppm)	291973	549665	515295	538669	537075	538472	541739

Mn (ppm)	3373.0	4327.7	9843.5	3178.6	3168.5	3162.7	3012.5
Fe (ppm)	13584.9	1275.2	2629.1	968.3	962.3	669.5	626.5
Sr (ppm)	23.0	402.1	117.6	56.9	56.4	48.4	42.2
La (ppm)	5.09	189.63	0.21	2.32	<DL	<DL	0.03
Ce (ppm)	12.79	469.57	0.48	5.35	<DL	0.01	0.06
Pr (ppm)	1.82	65.87	0.09	0.62	<DL	<DL	0.01
Nd (ppm)	9.41	303.98	0.48	2.43	<DL	<DL	0.11
Sm (ppm)	3.79	98.69	0.23	0.50	<DL	<DL	0.07
Eu (ppm)	0.63	15.74	0.04	0.04	<DL	<DL	<DL
Gd (ppm)	4.19	110.72	0.40	0.41	<DL	0.15	0.19
Tb (ppm)	0.86	16.84	0.09	0.04	<DL	0.06	0.03
Dy (ppm)	5.34	94.95	0.45	0.23	0.15	1.29	0.42
Ho (ppm)	1.13	16.51	0.08	0.08	0.09	0.56	0.23
Er (ppm)	3.39	41.63	0.36	0.34	0.58	2.68	0.94
Tm (ppm)	0.45	4.77	0.04	0.05	0.12	0.47	0.16
Yb (ppm)	3.08	29.36	0.31	0.80	1.28	4.38	0.87
Lu (ppm)	0.43	3.96	0.03	0.23	0.33	0.96	0.41
Eu Anomaly	0.2	0.2	0.1	0.1	N/A	N/A	N/A
ΣREE (ppm)	52	1462	3	13	3	11	5
(La/Lu)N	11.8	47.9	7.3	10.2	0.0	N/A	0.1
Sample	LR19G05	LR19G05	LR19G05	LR19G05	LR21G01	LR21G01	LR101G02
Mineral	Dolomite	Dolomite	Calcite 1	Calcite 1	Calcite 1	Calcite 1	Dolomite
Trend line	Max REE	Min REE	Max REE	Min REE	Max REE	Min REE	Max REE
Mg (ppm)	42456.6	92260.4	1348.8	1913.2	198.9	191.7	91837.0
Ca (ppm)	160720	17290	300747	288979	302958	295852	172037
Mn (ppm)	2800.4	4792.0	4464.6	5933.0	3374.1	3019.7	740.0
Fe (ppm)	3631.3	7878.0	1048.9	1804.5	874.6	712.3	1846.8
Sr (ppm)	51.0	56.2	54.7	105.6	26.9	33.9	98.2
La (ppm)	18.20	4.10	89.11	4.72	0.01	0.24	29.69
Ce (ppm)	34.56	8.09	158.82	8.40	0.05	0.21	22.21
Pr (ppm)	4.64	1.19	19.89	1.21	0.02	0.02	1.64
Nd (ppm)	21.60	6.86	91.16	6.01	0.19	0.07	5.43

Sm (ppm)	6.93	3.34	22.74	2.67	0.29	0.05	0.46
Eu (ppm)	1.00	0.32	3.84	0.30	0.05	0.01	0.09
Gd (ppm)	7.01	3.84	22.62	3.63	1.14	0.14	0.52
Tb (ppm)	0.88	0.58	2.37	0.45	0.50	0.02	0.04
Dy (ppm)	4.72	2.73	11.23	2.41	4.79	0.27	0.40
Ho (ppm)	0.78	0.57	1.96	0.49	1.13	0.06	0.14
Er (ppm)	2.13	1.57	4.22	1.31	4.91	0.18	0.80
Tm (ppm)	0.24	0.22	0.52	0.17	1.16	0.02	0.16
Yb (ppm)	1.93	1.73	3.30	1.47	11.89	0.28	1.76
Lu (ppm)	0.37	0.36	0.64	0.22	2.32	0.06	0.43
Eu Anomaly	0.1	0.1	0.2	0.1	0.1	0.2	0.2
ΣREE (ppm)	105	36	432	33	28	2	64
(La/Lu) _N	49.0	11.5	140.2	21.1	<0.1	4.4	69.2
Sample	LR101G02	LR10102	LR10102	LR105G02	LR105G02	LR105G02	LR105G02
Mineral	Dolomite	Calcite 1	Calcite 1	Dolomite	Dolomite	Calcite 1	Calcite 1
Trend line	Min REE	Max REE	Min REE	Max REE	Min REE	Max REE	Min REE
Mg (ppm)	93614.1	1595.1	981.9	81061.2	83614.1	2085.2	22.5
Ca (ppm)	165751	298173	301585	165629	165933	304883	301698
Mn (ppm)	2012.5	3321.4	2574.1	6701.7	10002.6	6495.9	1723.6
Fe (ppm)	9811.9	978.7	901.9	14142.4	15819.0	1368.0	332.4
Sr (ppm)	56.5	29.8	696.7	18.4	36.7	36.1	48.5
La (ppm)	12.35	362.33	27.13	25.71	3.22	135.81	0.03
Ce (ppm)	26.02	686.05	31.34	47.85	7.15	364.30	0.11
Pr (ppm)	2.89	77.84	2.54	6.12	1.01	56.66	0.02
Nd (ppm)	10.82	310.77	7.42	29.22	4.52	290.41	0.17
Sm (ppm)	1.63	54.98	1.12	7.36	1.21	68.28	0.09
Eu (ppm)	0.24	11.34	0.23	0.58	0.11	2.24	0.02
Gd (ppm)	1.68	62.71	1.24	7.90	1.32	62.07	0.25
Tb (ppm)	0.21	6.79	0.18	1.06	0.21	5.29	0.04
Dy (ppm)	1.21	32.88	1.25	5.90	1.41	18.49	0.30
Ho (ppm)	0.34	5.53	0.24	0.98	0.28	2.49	0.11
Er (ppm)	1.33	11.82	0.54	2.47	0.72	4.43	0.31

Tm (ppm)	0.26	0.95	0.06	0.24	0.09	0.32	0.06
Yb (ppm)	2.34	5.09	0.25	1.56	0.69	1.54	0.71
Lu (ppm)	0.46	0.70	0.03	0.24	0.11	0.25	0.12
Eu Anomaly	0.1	0.2	0.2	0.1	0.1	<0.1	0.1
ΣREE (ppm)	62	1630	74	137	22	1013	2
(La/Lu) _N	26.9	520.3	1029.0	105.7	30.1	534.8	0.3

Table 9. Fluid inclusion types hosted in quartz and calcite of five-element veins in order of abundance.

	Fluid Inclusion Type					
	i	ii	iii	iv	v	vi
Assemblage (at 20°C)	L-V-H	L-V-S	L-V	L-V	V	Decrepitated
Relative abundance	XX	X	X	X	XXX	XXX
Size	<5 µm	2-7 µm	3-5 µm	3-7 µm in qtz; up to 30 µm in cal	1-5 µm in qtz; up to 30 µm in cal	5-30 µm
Volume %	L:V:H, 75:15:15%	L:V:S, 60:10:30%	L:V, 80:20%	L:V 60:40%	V - 100%	V - 100%, some L and S
Shape	R, Ir	Ir	R	Ir, R	R	N
Occurrence	P in cores of comb qtz, I and S in qtz	I in cores of comb qtz	PS in qtz, I in quartz	PS and I in qtz, P in calcite	P along growth zones in qtz; I in quartz cores, S in qtz	P abundant in margins of comb qtz, PS in qtz

Abbreviations: L = liquid, V = vapor, H = halite, S = unknown solid, XXX = Abundant, XX = Common, X = Rare, Ir = Irregular, R = Regular, N = Negative, S. = secondary, PS = pseudosecondary, P. = primary, I = indeterminate, Quartz – qtz

Figures

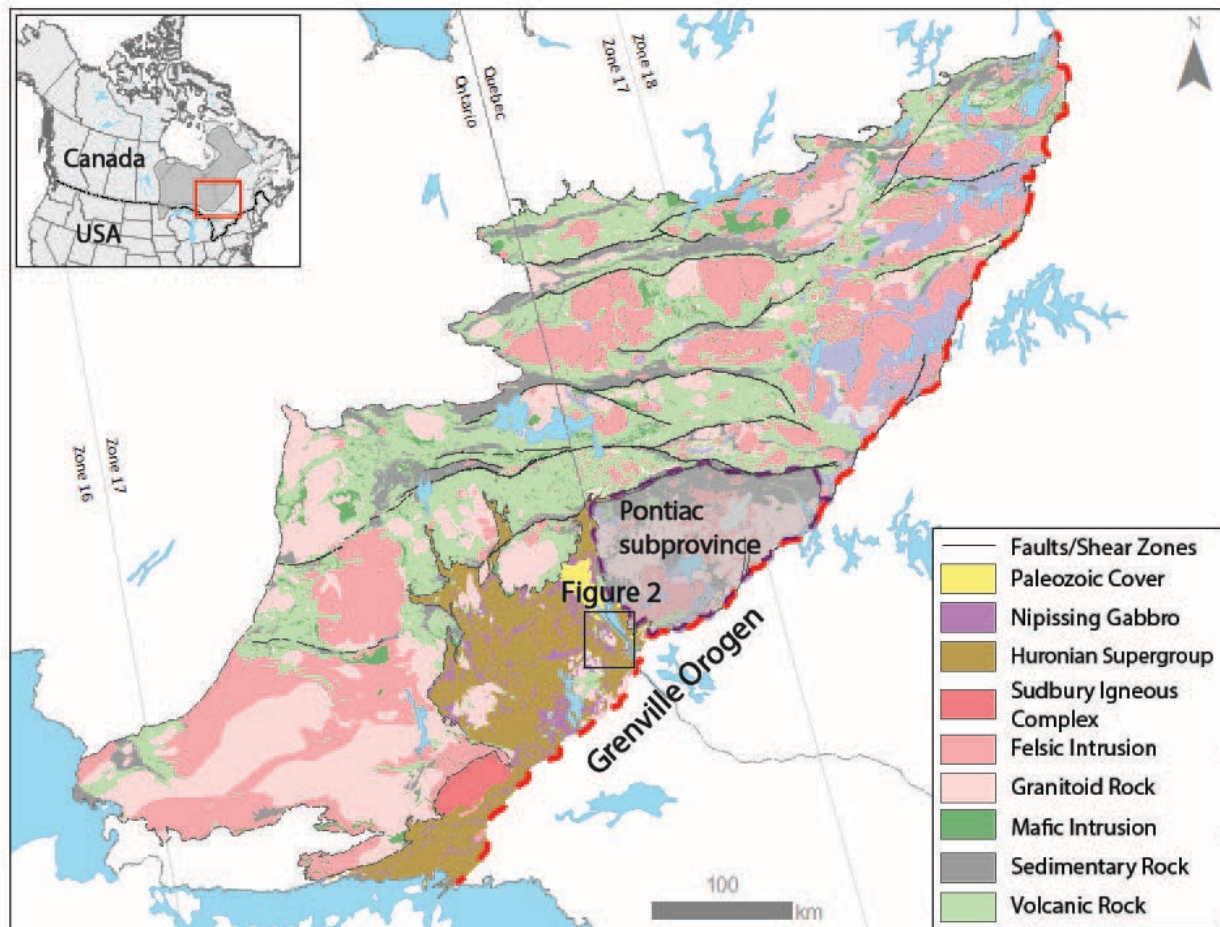


Figure 4. Location of Cobalt, Ontario, Canada with respect to the Abitibi subprovince, in the Superior province of the Canadian Shield. The Cobalt Embayment is roughly outlined by the Huronian Supergroup. The Cobalt district study area is outlined in the black box. The Pontiac subprovince is outlined by the greyed area and the Grenville Orogen bounding the Abitibi subprovince is indicated by the red dashed line (Montsion et al., 2018).

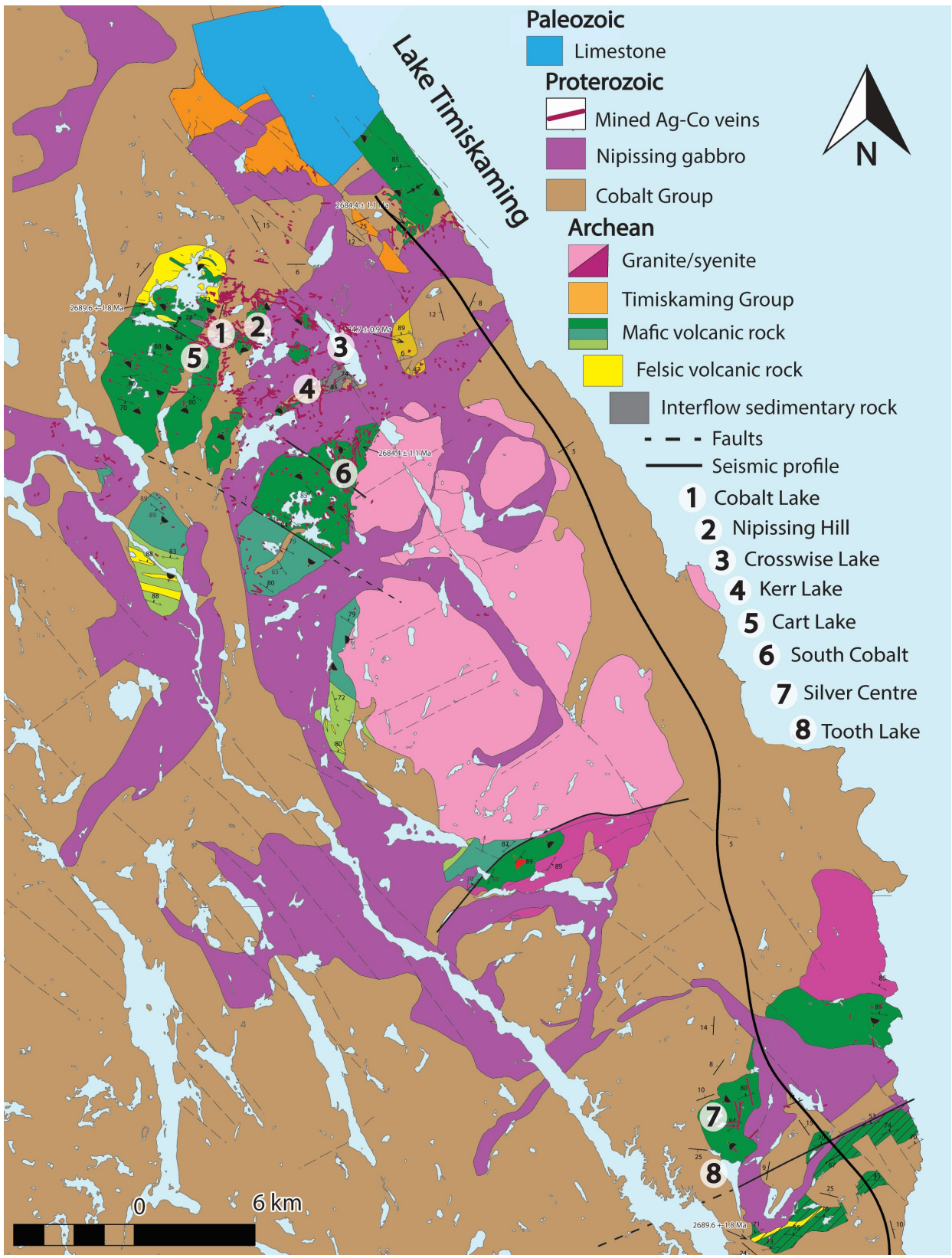


Figure 5. Location and geological setting of the Cobalt district (White et al., 2020 in prep.).

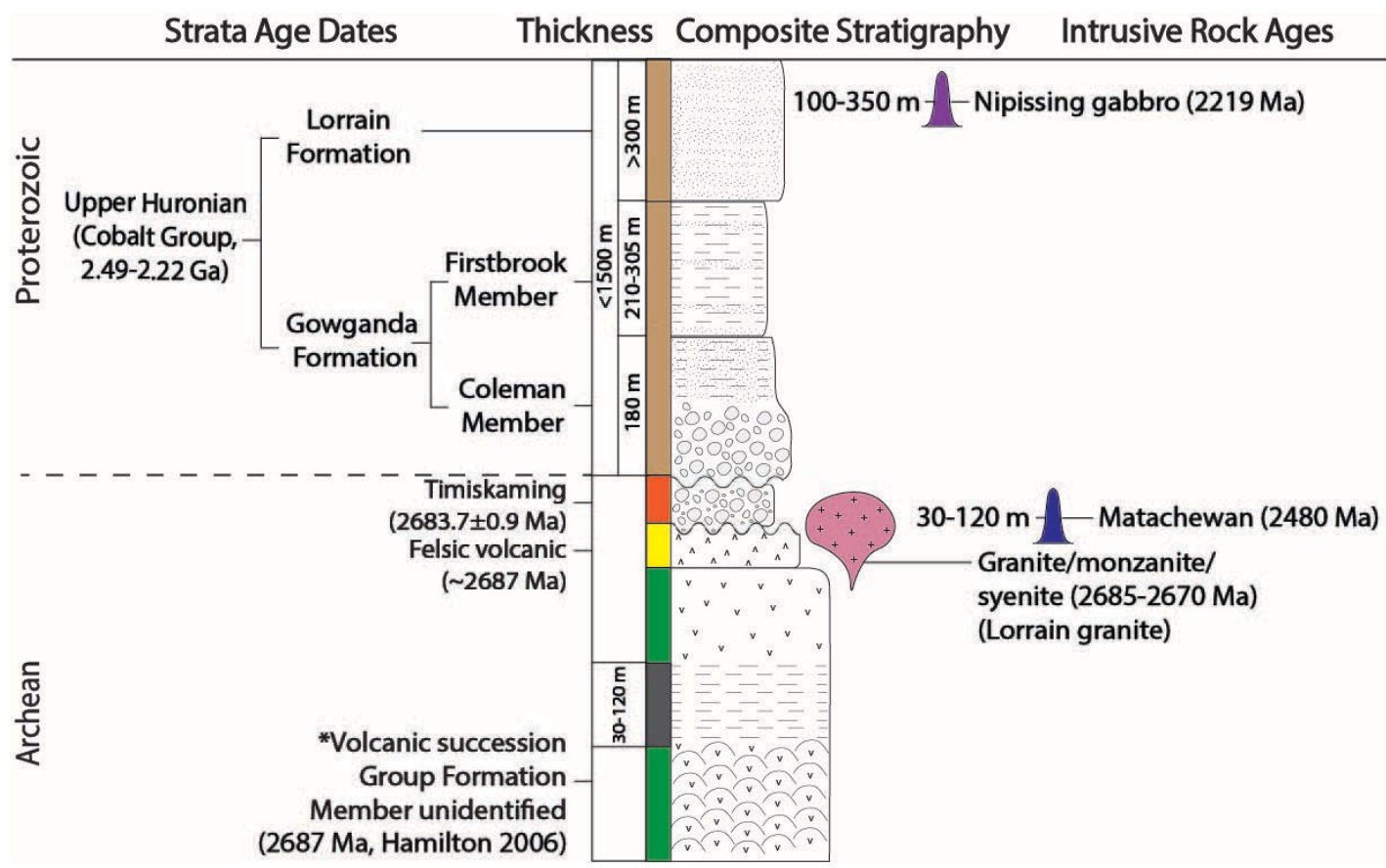


Figure 6. A stratigraphic section of idealized geological relationships and ages of formations and intrusions of the Cobalt Embayment.

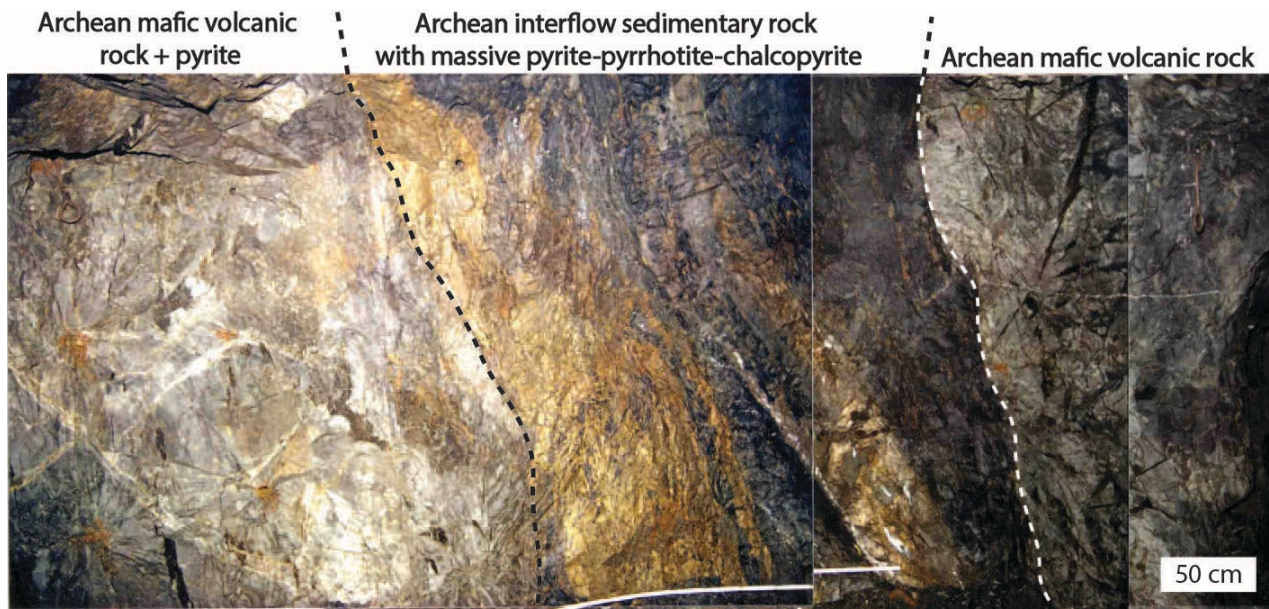


Figure 4. Massive pyrite, pyrrhotite, and chalcopyrite zones in Archean interflow sedimentary units (i.e. slates) bounded by mafic volcanic rock at the Beaver Temiskaming Mine North Face, 1463 Drift, 1450 Sub-level (D. Robinson, pers. commun., 2020; see additional images in App. A).

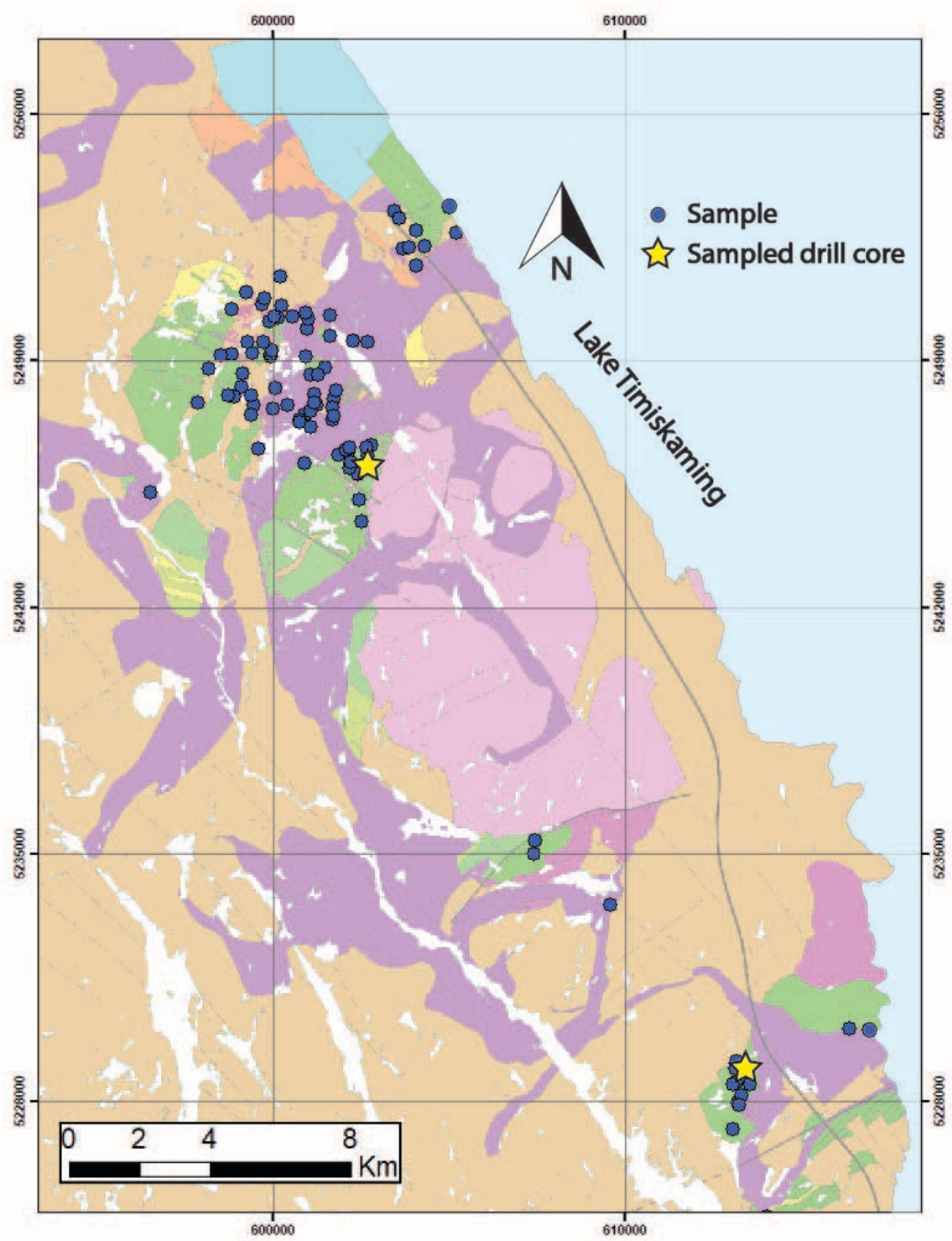


Figure 5. Distribution of samples used in this study from discard piles adjacent to historic mine workings, as well as the locations of sampled First Cobalt drill core featuring five-element vein mineralization and basement-hosted sulfide mineralization (representative examples of samples are in Figure 6).

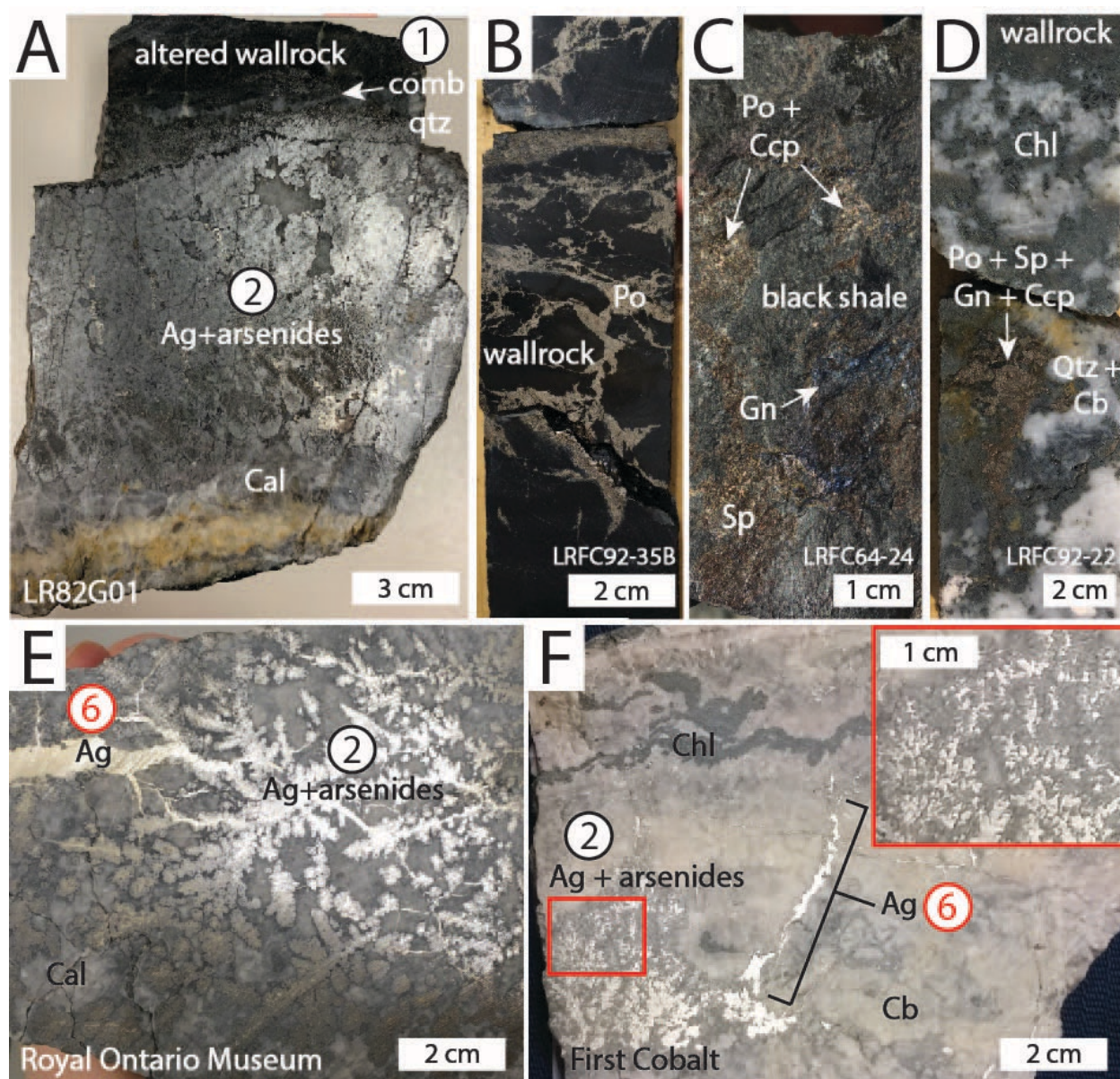


Figure 6. Representative mineralized samples at Cobalt. (A) Sample from discard pile featuring five-element mineralization. (B) Drill core (LRFC92-35B; 132.4 m) showing Archean interflow black shale breccia containing pyrrhotite. (C) Drill core (LRFC64-24; 121 m) showing Archean interflow black shale containing sphalerite, galena, pyrrhotite, and chalcopyrite. (D) Drill core (FCC-19-0192; 91.5 m) showing a quartz-carbonate-base-metal sulfide vein intersection hosted in Coleman wacke. (E) Sample of primary Ag and arsenide dendrites with calcite, and late cross-cutting remobilized native silver. (F) Five-element vein with native silver and arsenide rosettes (red boxed area enlarged in the upper right corner) with carbonate (ferroan dolomite) and late remobilized native silver (First Cobalt, 2020).

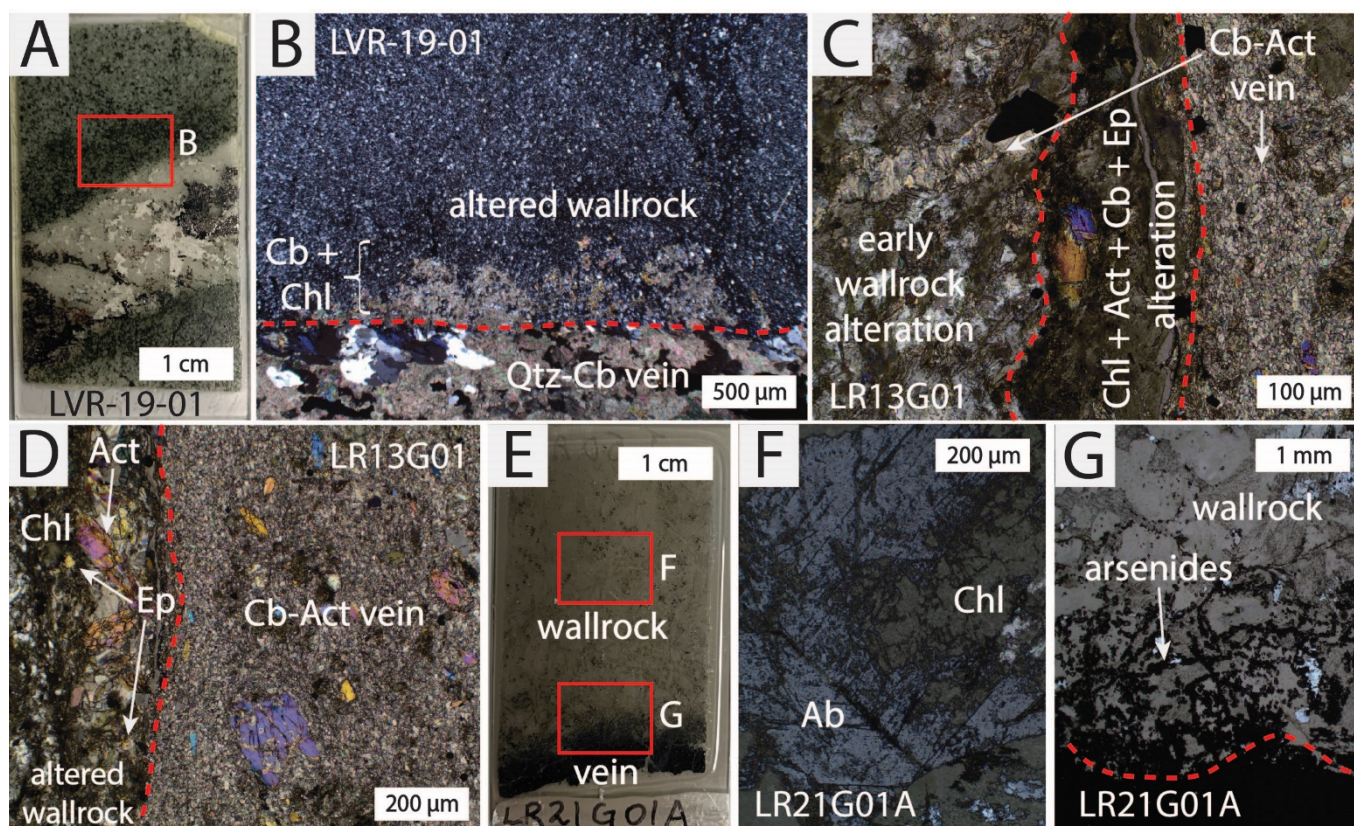


Figure 7. Photographs of polished thin sections in plane (A, E, G) cross-polarized (B, C, D, F) light showing features of wallrock alteration. Picture enlargements are outlined as red boxes. (A, B) Chloritized wallrock and narrow carbonate alteration to quartz-five-element vein. (C, D) Narrow zone of intense chlorite, actinolite, carbonate, and epidote alteration after gabbroic wallrock proximal vein with later carbonate lining a fracture. (E, F, G) Alteration of gabbro wallrock with close up of wallrock distal to vein (F) showing albitization of plagioclase and extensive replacement of pyroxene with chlorite. Close up of vein margin (G) shows alteration related to arsenides in the wallrock.

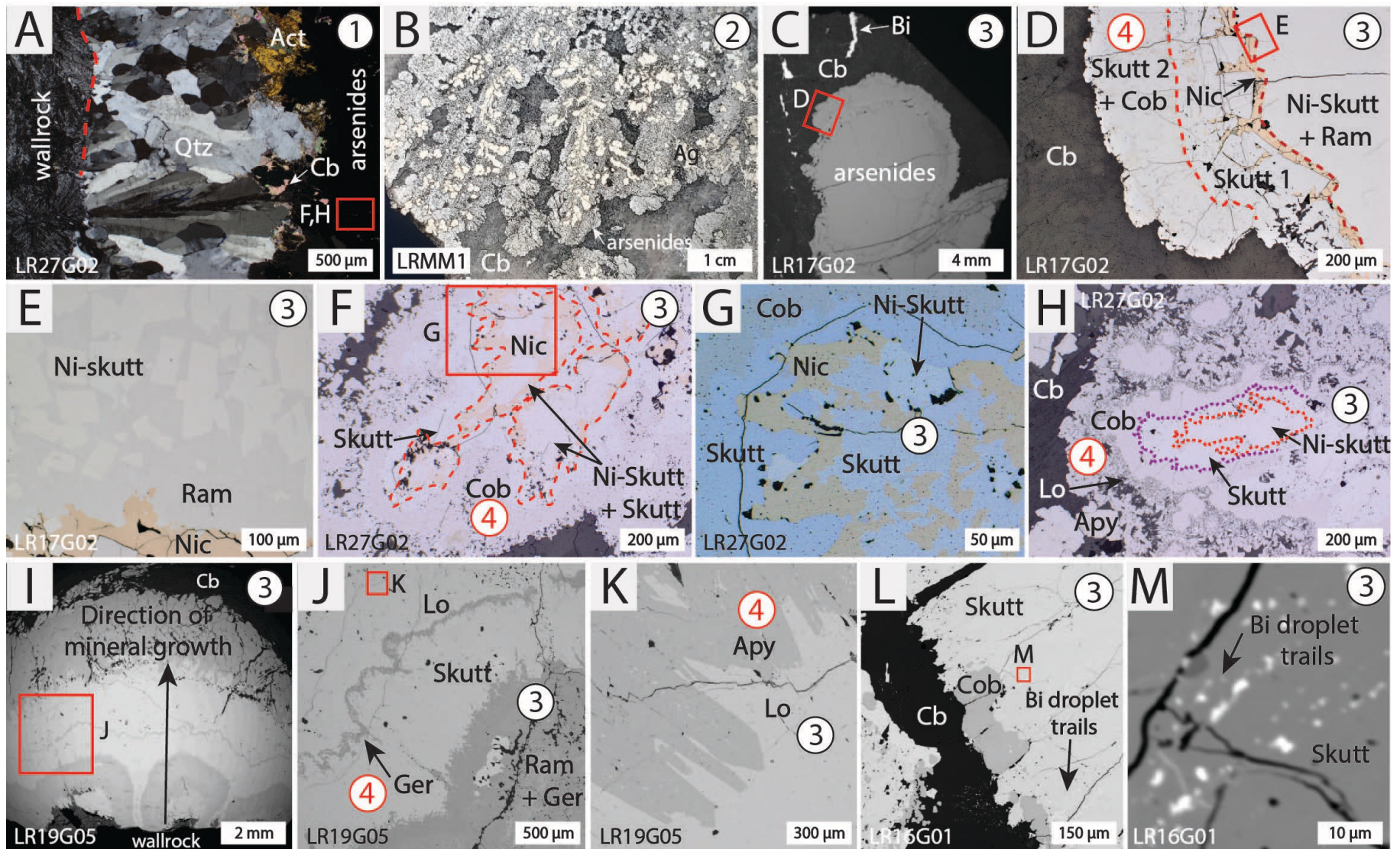


Figure 8. Photomicrographs in cross-polarized (A), reflected (B, D-H) light, and SEM-BSE images (C, I-M) of different vein stages as indicated by the numbers, which equate to the mineral paragenesis in Figure 10. Picture enlargements are outlined as red boxes.

Colored dashed lines are reaction interfaces. (A) Early comb quartz with flared texture radiating from wallrock contact with subsequent growth of extensional fibrous actinolite and overgrowth of carbonate around arsenide aggregates. (B) Native silver (Ag) dendrites coring arsenides (see close up in Fig. 11). (C-K) Common progression in the arsenide aggregates from early Ni-As phases (Nic, Ni-skutt, Ram) and Co-As (Skutt, Saff) that are replaced via CDP to Co-As-S (Cob) and Ni-As-S (Ger) phases. (L) Native bismuth droplets hosted in arsenide minerals. (M) Enlargement of L.

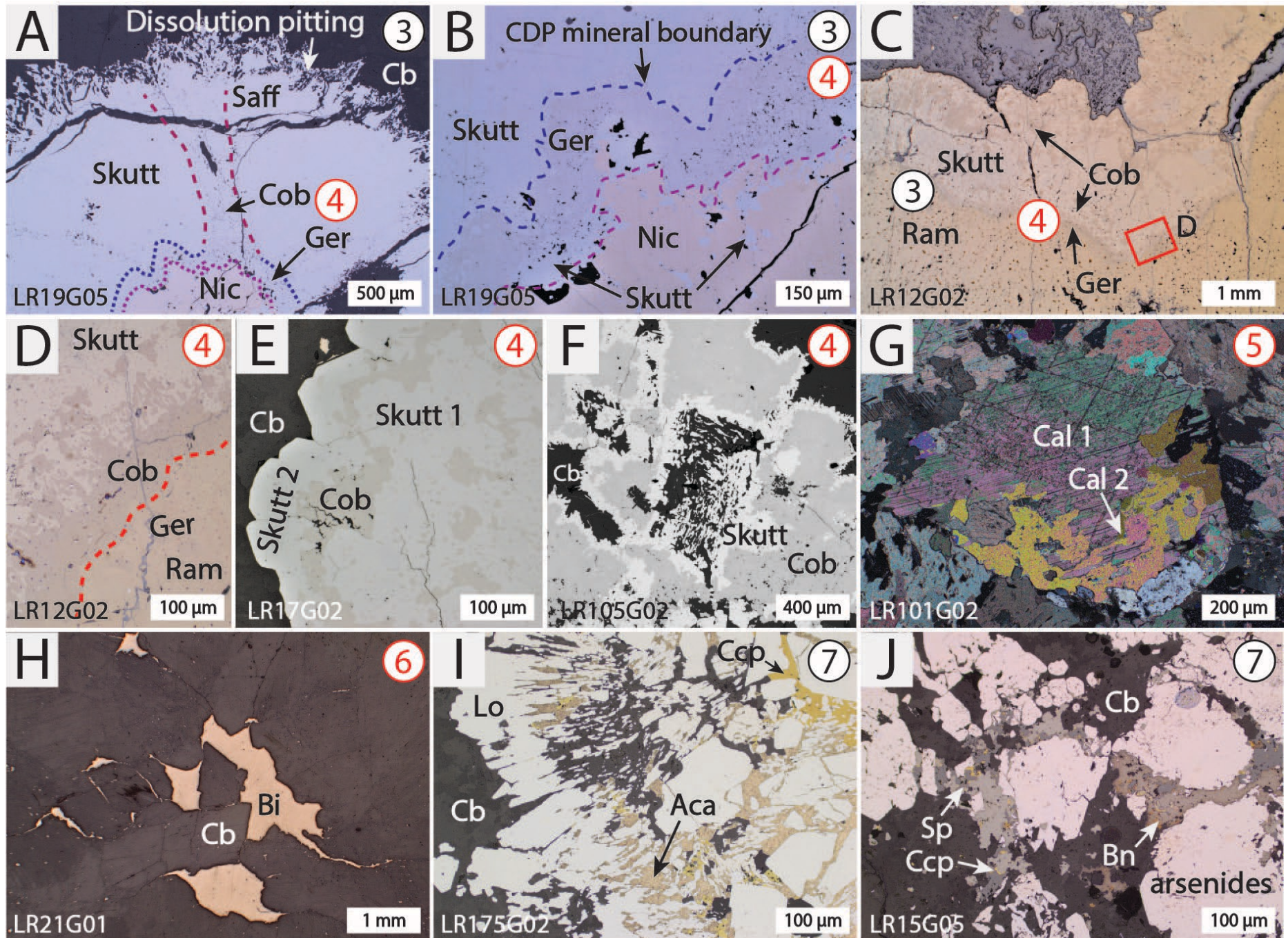


Figure 9. Photomicrographs in reflected (A-E, H-J) and cross-polarized (G) light, and an SEM-BSE image (F) of different vein stages as indicated by the numbers, which equate to the mineral paragenesis in Figure 10. Picture enlargements are outlined as red boxes. Colored dashed lines are reaction interfaces. (A-D) Common progression in the arsenide aggregates from early Ni-As phases (Nic) and Co-As (Skutt, Saff) that are replaced via CDP to Co-As-S (Cob) and Ni-As-S (Ger) phases along mineral interfaces. (E, F) Late skutterudite replacing cobaltite along dissolution feature later filled by carbonate. (G) Multi-generations of vein calcite accompanying native metal and arsenide mineralization (opaque phases). (H) Late native bismuth (Bi) lining fractures and pores in vein calcite. (I, J) Late sulfide phases (acanthite (Aca), sphalerite (Sp), chalcopyrite (Cp), bornite (Bn)) lining open space between various arsenides.

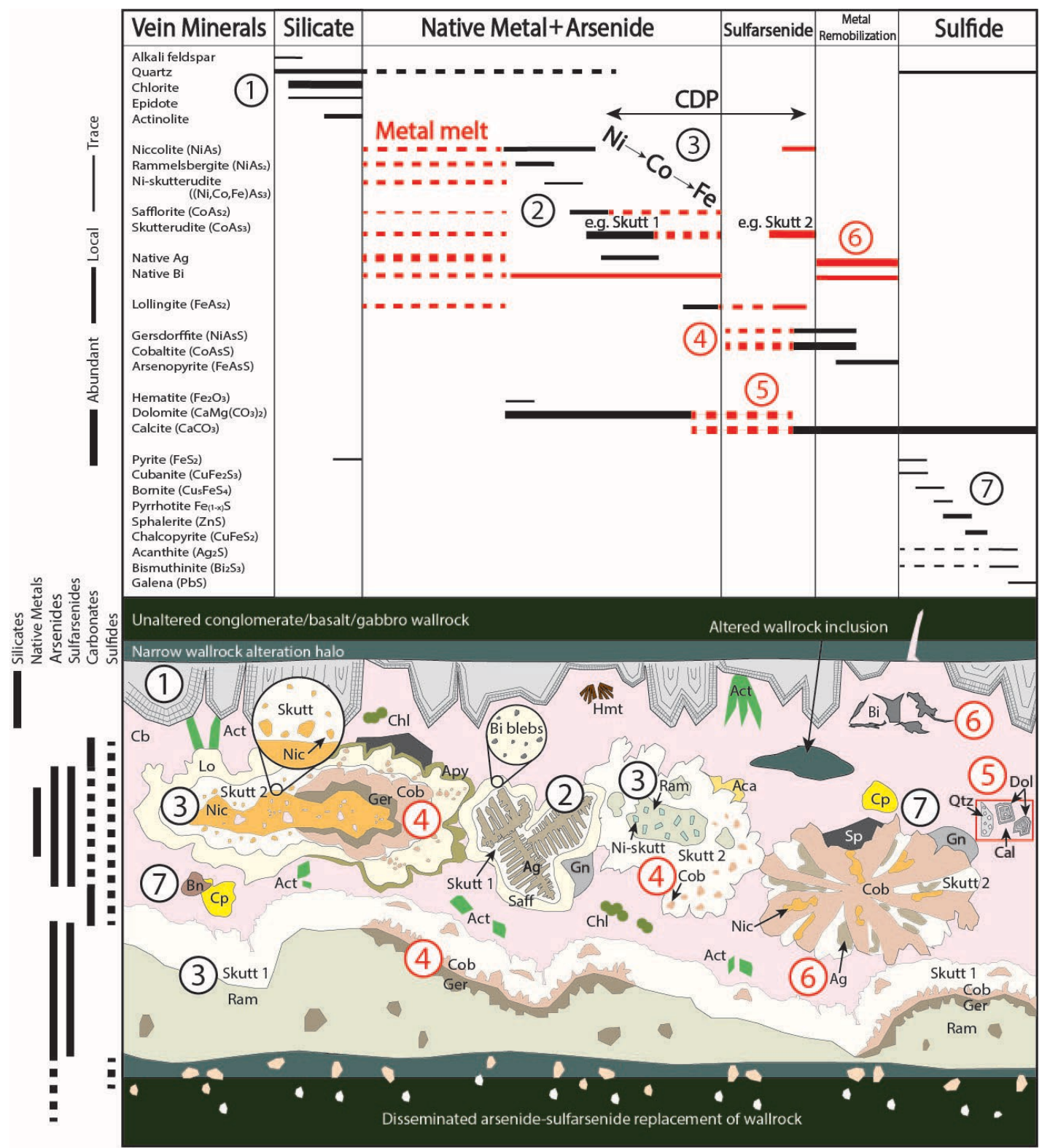


Figure 10. Summary of mineral paragenesis for the Cobalt five-element veins with a coupled schematic diagram summarizing the important relationships. Note that numbers represent the areas in the diagram with new findings highlighted in red whereas typical observations are in

black. The mineral colors used approximate what is seen in transmitted and reflected light for whatever is appropriate. Solid and dashed lines to the left of the schematic diagram indicate where in vein space the mineral stages are found within the veins.

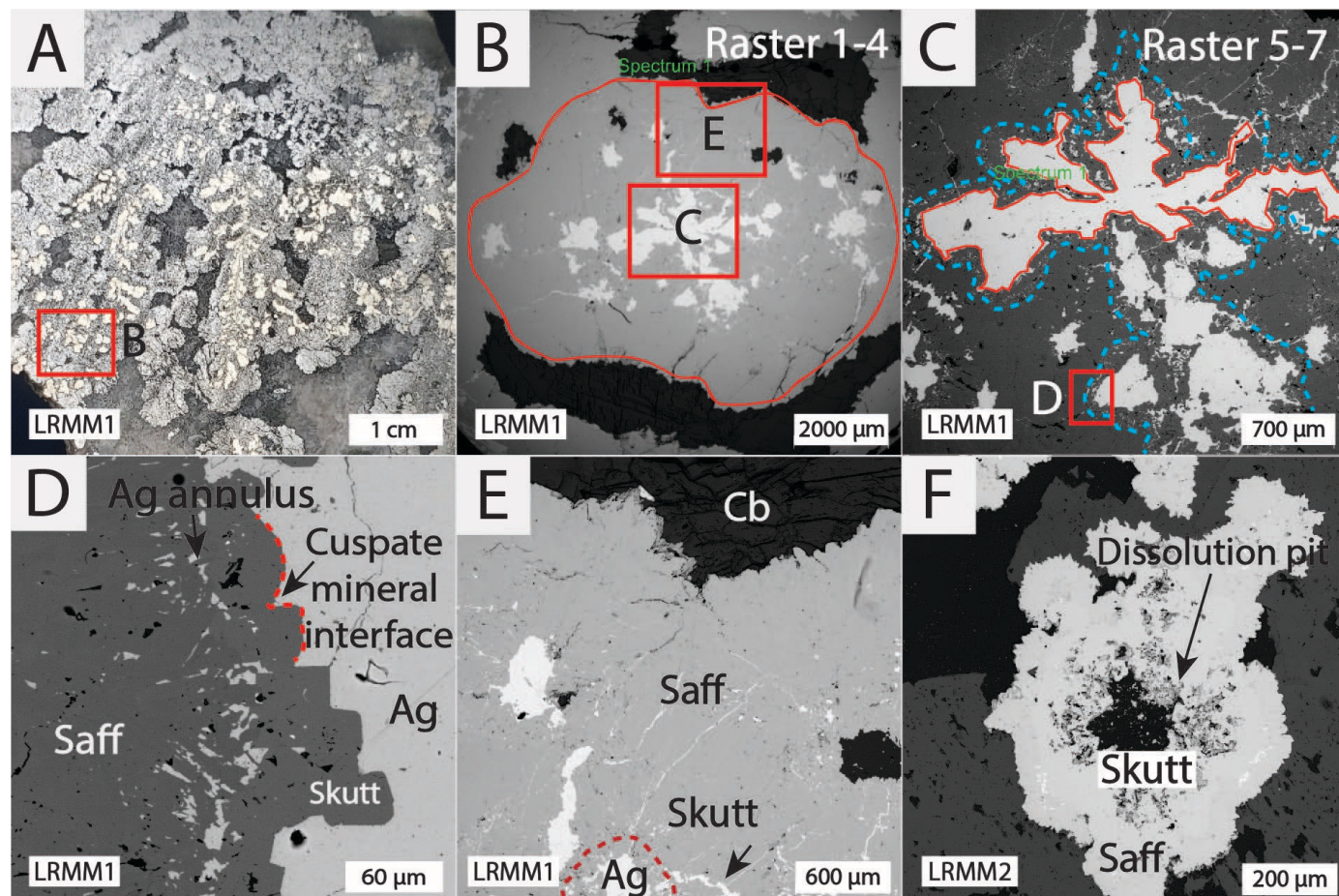


Figure 11. SEM-BSE images of representative primary (absent of CDP) five-element vein mineralization with native silver (Ag) dendrites coring arsenides pods surrounded by carbonate. Picture enlargements are outlined as red boxes. See Table 2 for raster data of areas in (B, C). (A, B) Example of one of four areas of raster analysis. Letters indicate areas shown in detail in C – E. (C) Area of Ag-Sb dendrite. Blue dashed line shows annulus of smaller Ag-Sb phases around larger Ag-Sb dendrite. (D) Cuspate interfaces between skutterudite and Ag-Sb phase. Note skutterudite subhedral crystal shapes. (E) Skutterudite-safflorite interface (red dashed line) defines the outer arsenide phase of the dendrites. (F) Small arsenide pod with a central dissolution pit which resembles Ag dendrites in other samples.

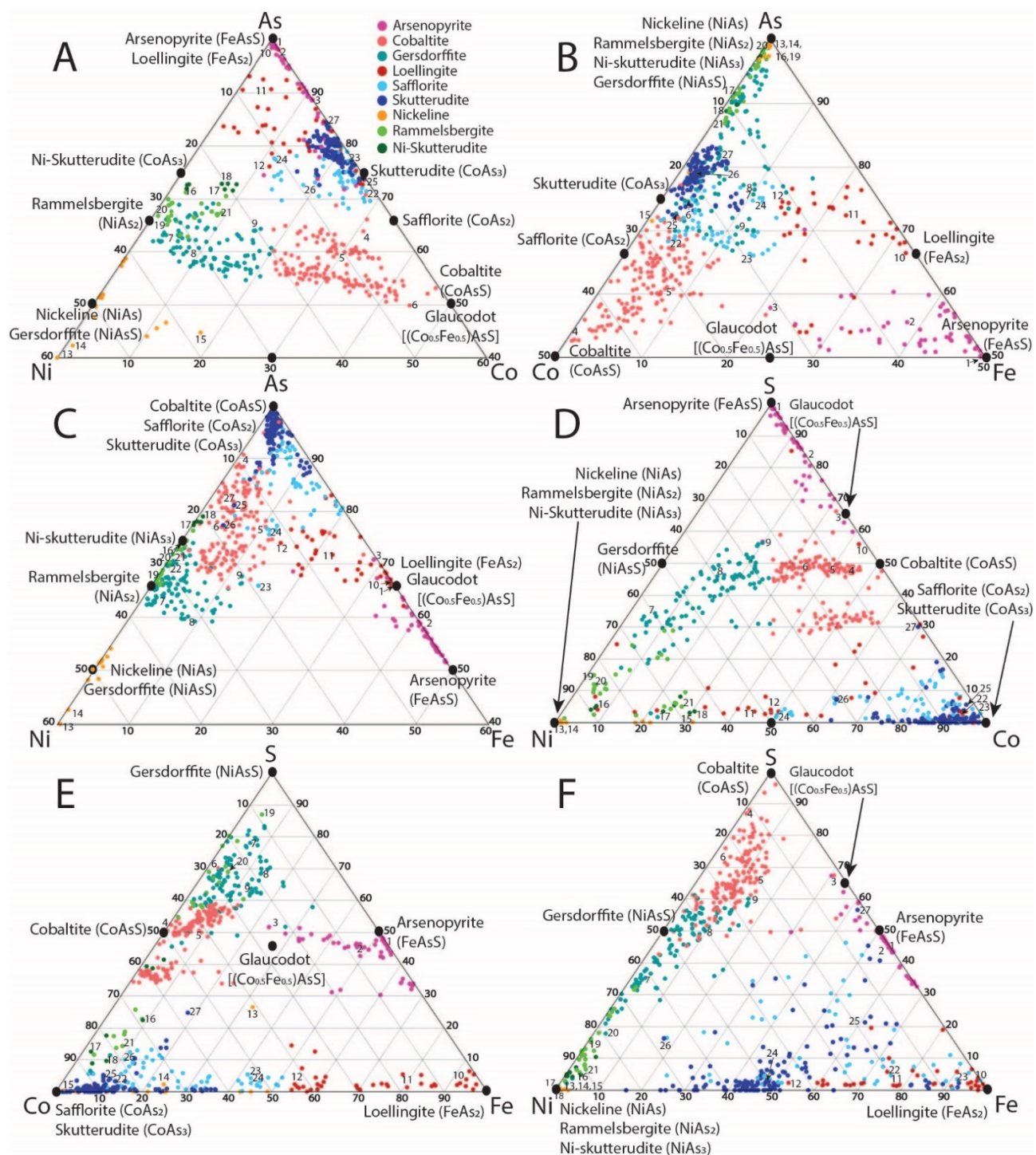


Figure 12. SEM-EDS data plotted for five-element vein arsenide and sulfarsenide mineral phases in different ternary spaces. Representative data for mineral composition are in Table 3, which correspond to the numbered samples in the ternary diagrams. Note end member Ni-Co-Fe-arsenide and sulfarsenide minerals are plotted on the diagram, but that the data illustrate that the arsenide and sulfarsenide phases are not stoichiometric. Note that A, B, and C are zoomed to the data, where only As greater than 60 (in A and C) and 50 (in B) is shown.

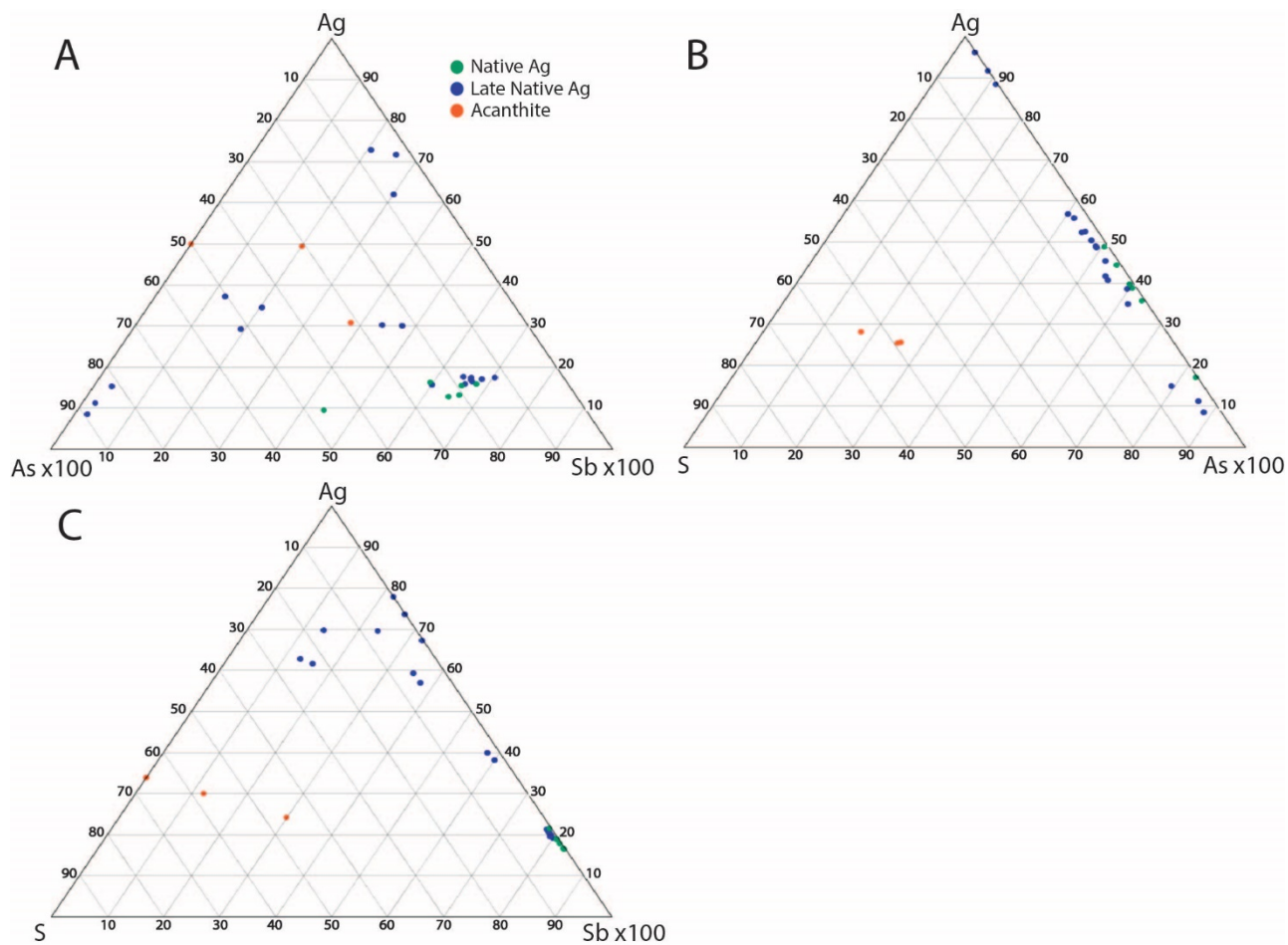


Figure 13. SEM-EDS data for five-element vein Ag-bearing minerals plotted in ternary space. Note that Sb and As are multiplied by 100 to see data spread better.

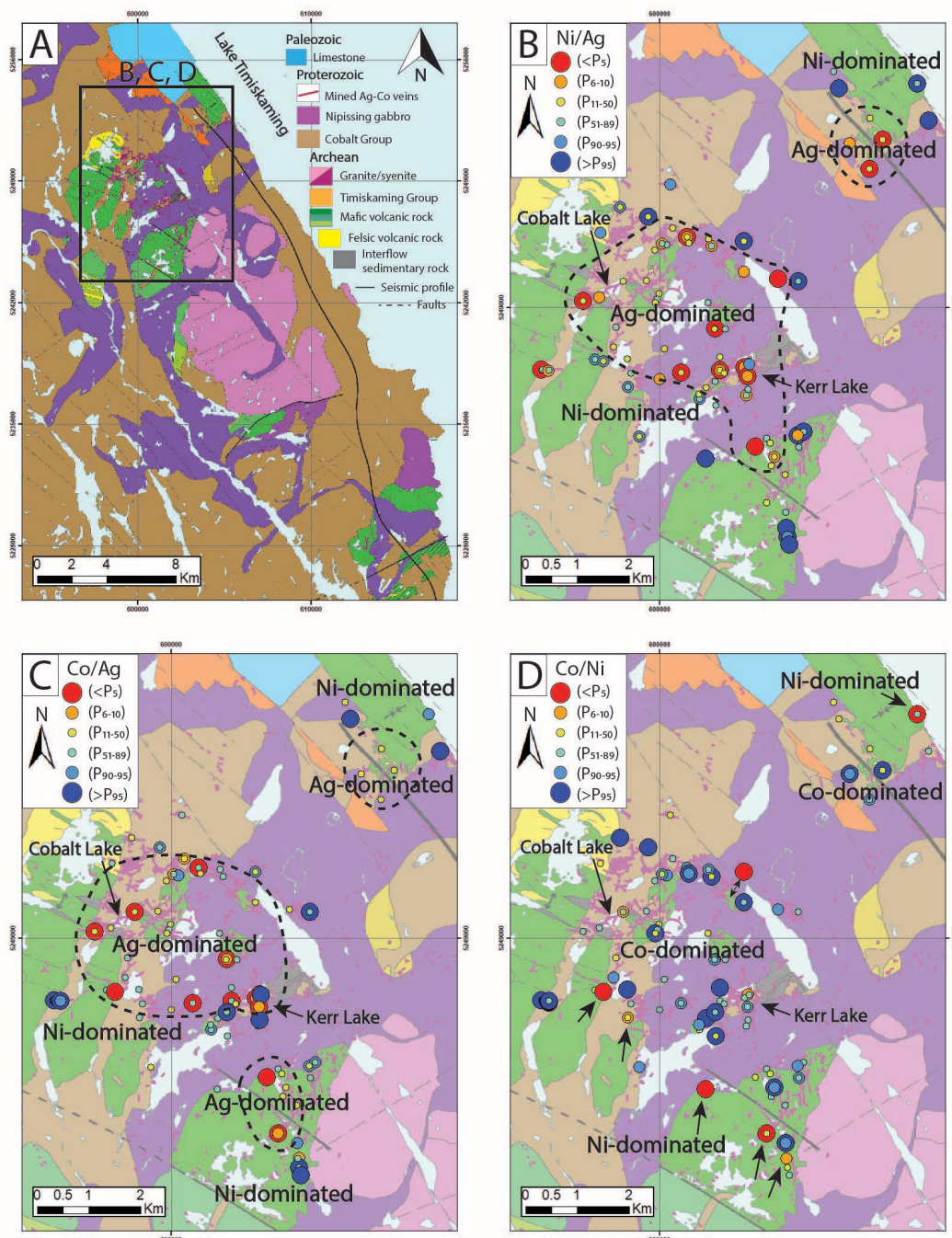


Figure 14. Representative metal percentile plots (in ppm) of the Cobalt subarea. More detailed maps, with additional element ratio layers, are given in Appendix G. Note that for any samples from the First Cobalt's database that were over-limit or under-limit were assigned the over-limit or under-limit detection values, respectfully. (A) Geological map of the study area (White et al., 2020 in prep.) with black box, referring to inset maps B, C, and D. (B) Ni/Ag; dashed areas are relatively Ag-dominated with respect to Ni. (C) Co/Ag; dashed areas are relatively Ag-dominated with respect to Co. (D) Co/Ni; black arrows point to Ni-dominated samples with respect to Co, which are spatially associated to the Archean mafic volcanic inliers as the green unit.

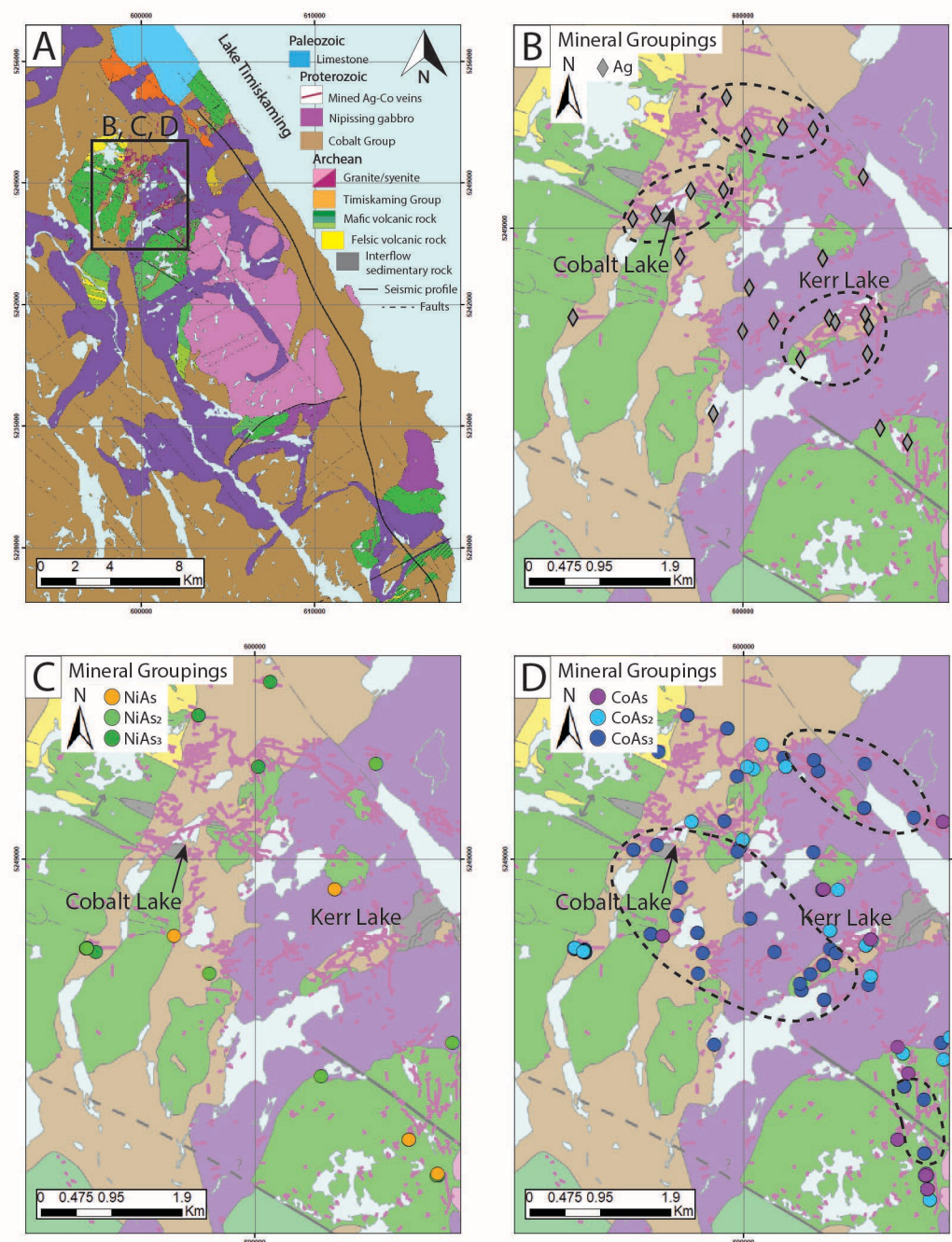


Figure 15. Representative mineral groupings plots of the Cobalt subarea. More detailed maps, with additional element ratio layers, are given in Appendix G. note that any samples from the First Cobalt's database that were over-limit or under-limit were assigned the over-limit or under-limit detection values, respectfully. (A) Geological map of the study area (White et al., 2020 in prep.) with the black box, referring to inset maps B, C, and D. (B) Ag-dominated samples; dashed areas show Ag-dominated samples, which occur in pockets of high vein density. (C) Ni-dominated samples spatially associated to the Archean mafic volcanic inliers as the green unit. (D) Co-dominated samples where CoAs₃ dominated samples occur most abundant in dashed areas, which roughly spatially correlate to Ag-dominated samples seen in B, and CoAs₂- and CoAs₁-dominated samples are peripheral to CoAs₃ distribution.

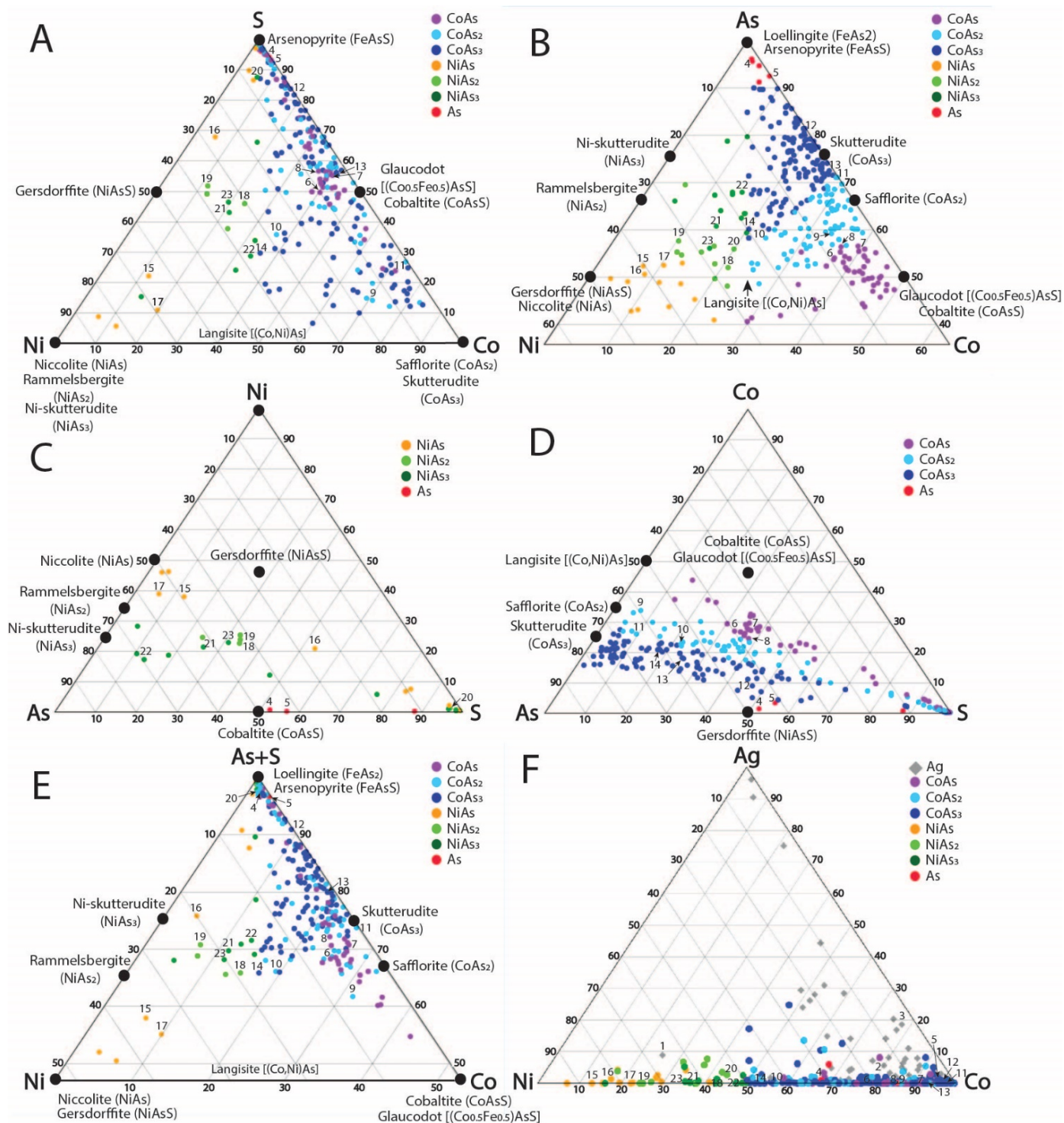


Figure 16. Five-element vein assay data plotted in ternary space with reference to the vein minerals. Samples are grouped as Ni and Co to As molar proportion (CoAs, CoAs₂, CoAs₃, NiAs, NiAs₂, NiAs₃). Representative samples of each mineral group (numbered, see data in Table 6) are for samples collected during the 2019 field season. Note that B and E are zoomed to the data, where only As greater than 60 is shown.

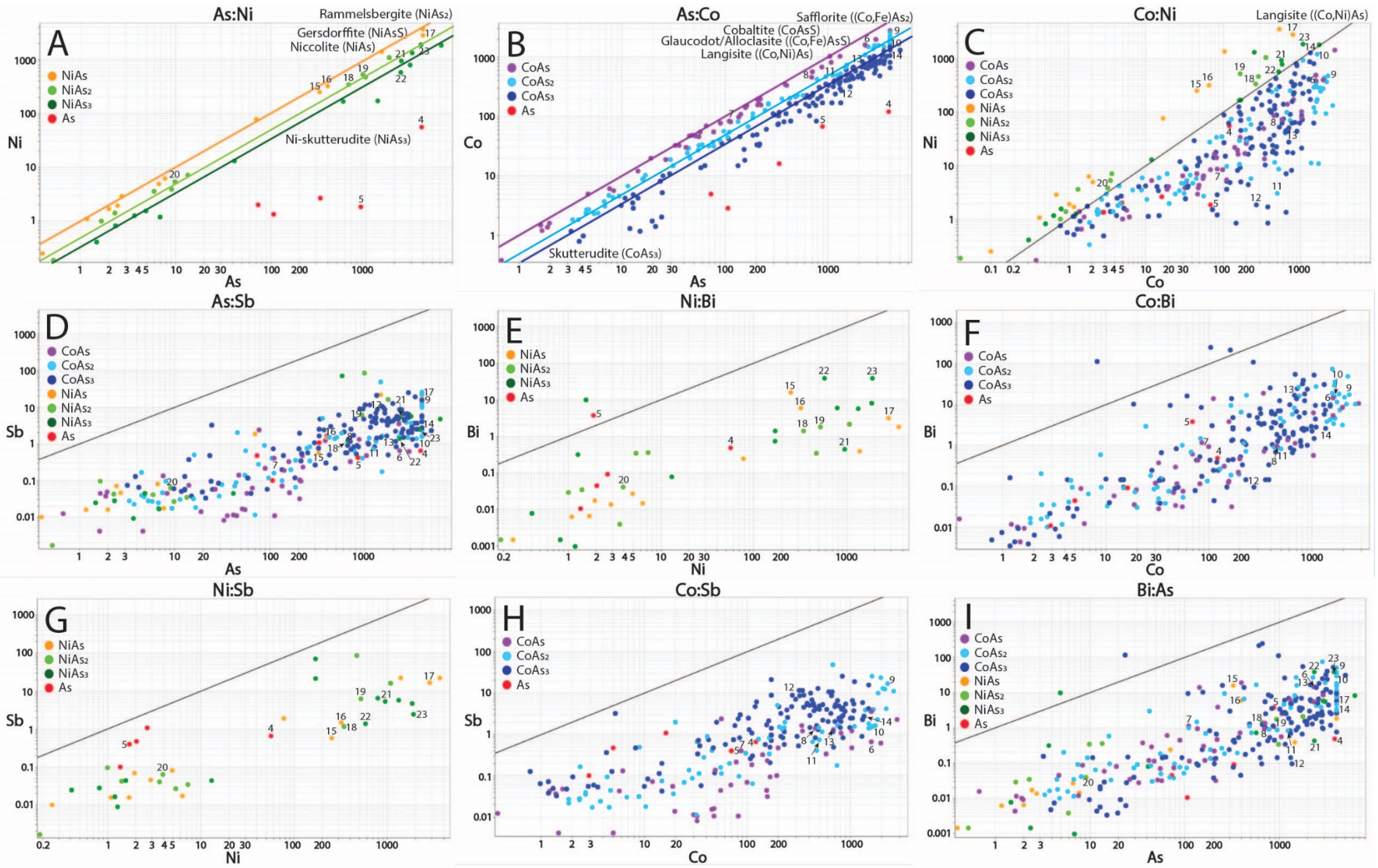


Figure 17. Five-element vein assay data of samples plotted in binary log-log space of five-element vein minerals showing Ni-Co-Bi-As-Sb covariance. Coloured lines show end-member mineral trajectories. Samples are grouped as Ni and Co to As molar proportion (CoAs , CoAs_2 , CoAs_3 , NiAs , NiAs_2 , NiAs_3) dependent on elemental proportions. Representative samples of each mineral group (numbered, see data in Table 6) are from the samples collected during the 2019 field season. Note end member Ni-Co-Fe-arsenide and sulfarsenide minerals plotted on the diagram as line trajectory (colors according to mineral) where applicable (black line is 1:1 projection).

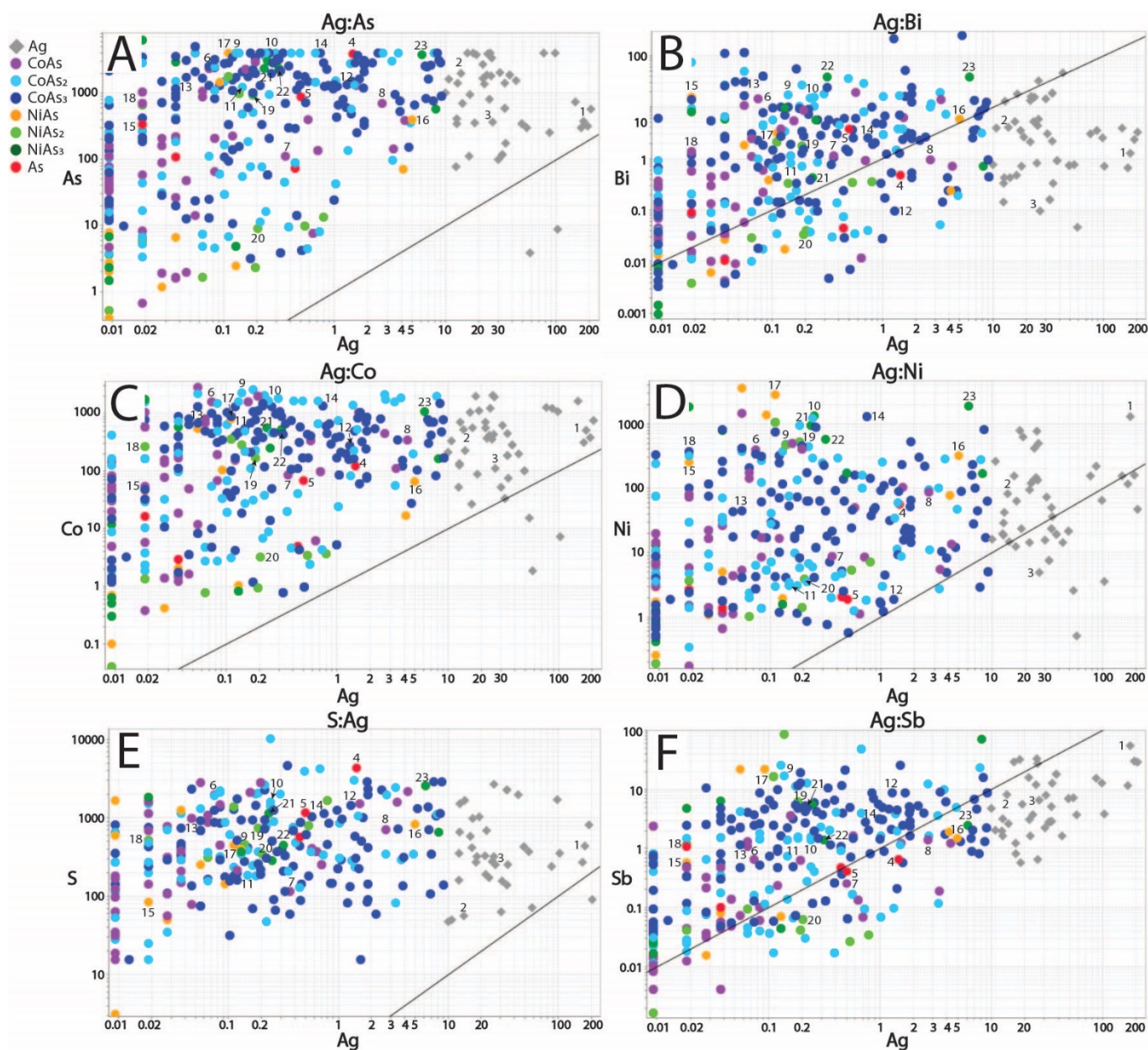


Figure 18. Five-element vein assay data for five-element vein samples plotted in binary space as a function of varying Ag abundance. Note data are in log-log space. Samples are grouped as Ag-dominated, Ni and Co to As molar proportion (CoAs, CoAs₂, CoAs₃, NiAs, NiAs₂, NiAs₃). Note high scatter of points for all plots (black line is 1:1 projection).

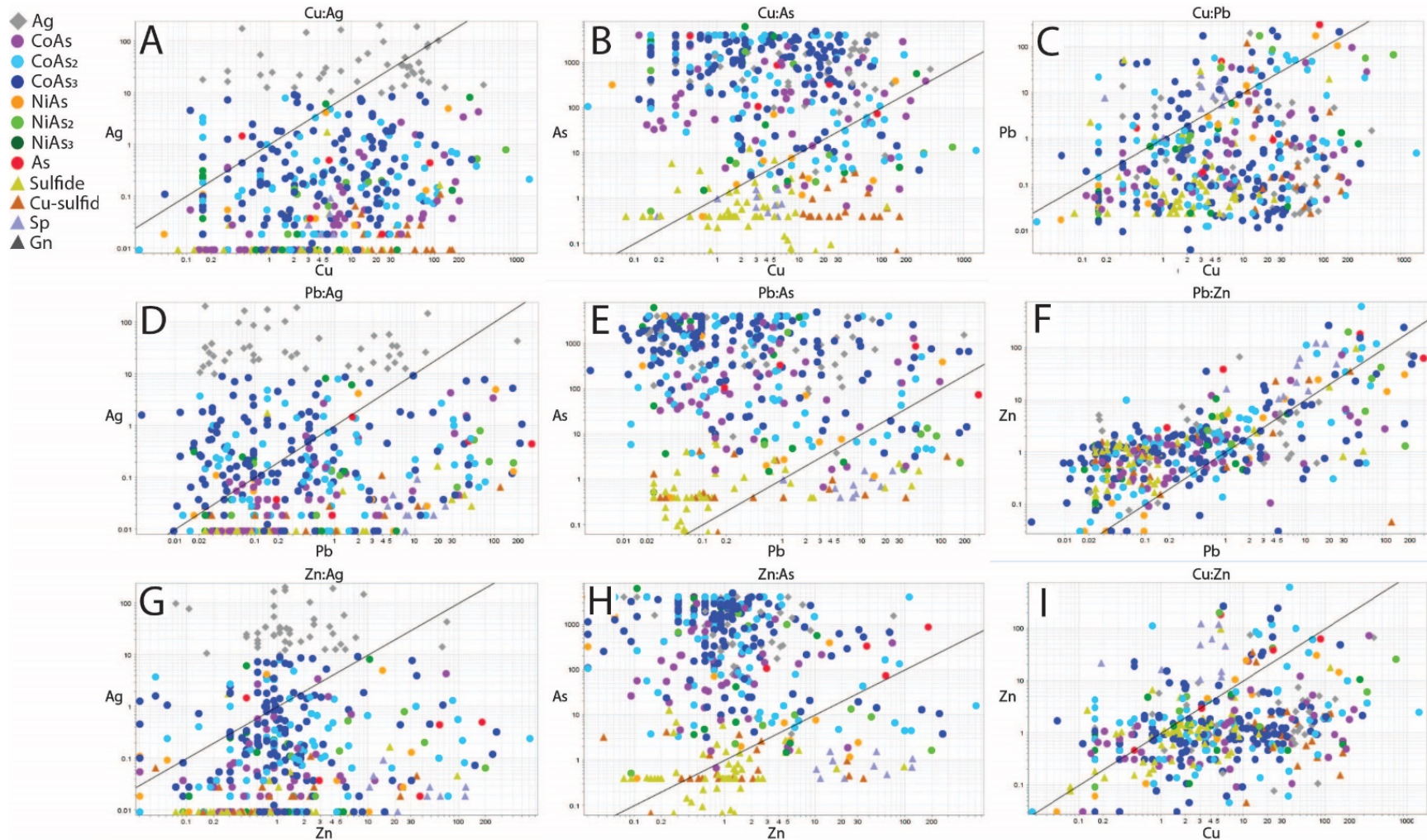


Figure 19. Five-element vein assay data for five-element vein samples plotted in binary space as a function of varying Cu, Pb, and Zn abundance with respect to the Ag and arsenide five-element phases. Note data are in log-log space. Samples are grouped as Ag-dominated, Ni and Co to As molar proportion (CoAs, CoAs₂, CoAs₃, NiAs, NiAs₂, NiAs₃), and Cu-sulfide-, sphalerite-, and galena-dominated. Note high scatter of points for all plots (black line is 1:1 projection), except for higher clustering for the Pb:Zn (F) and Cu:Zn (I) plots.

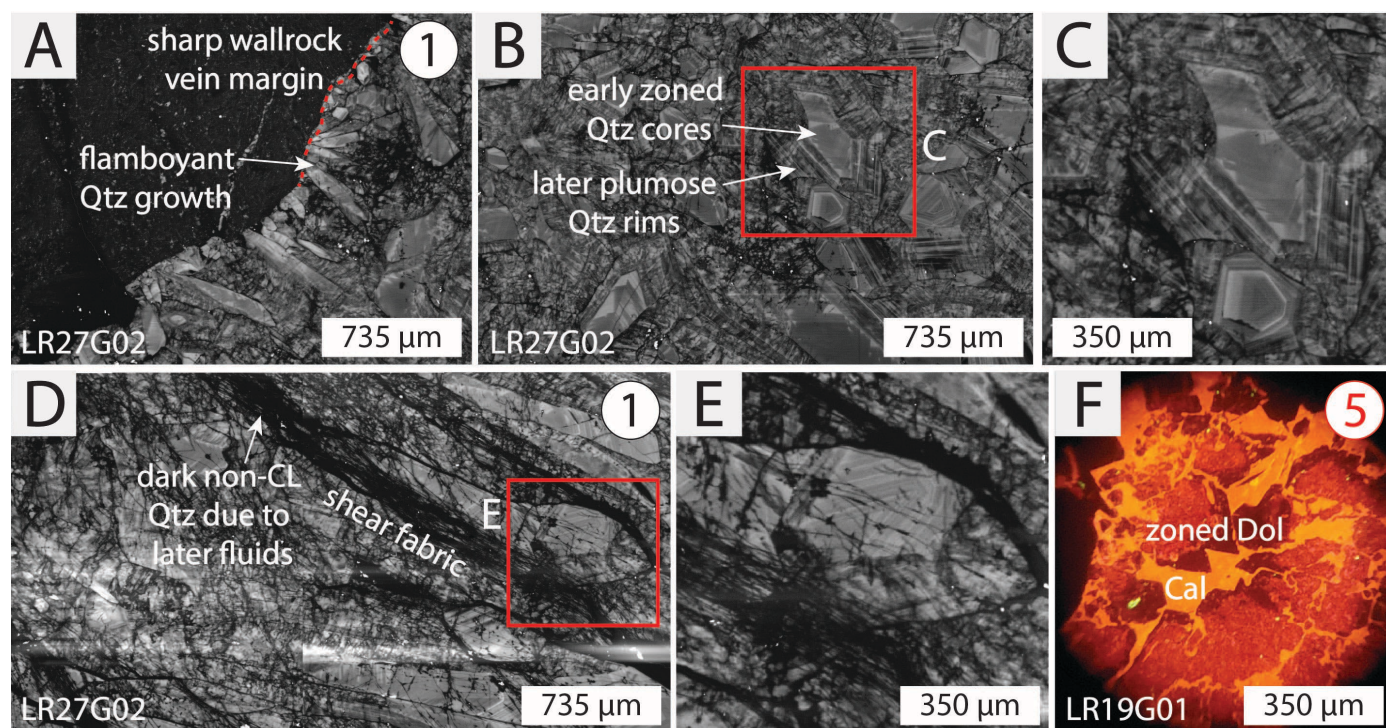


Figure 20. Cathodoluminescence (CL) images of vein quartz and carbonate. Numbers refer to vein paragenetic stages as in Figure 10. Picture enlargements are outlined as red boxes. (A, B) Flamboyant quartz radiating from vein contact. Note the euhedral zoned cores with zoned feathery-plumose rims. (C) Enlargement of (B). (D) Quartz featuring CL dark areas along fractures throughout overprinting shear fabric. (E) Enlargement of (D). (F) CL image of breccia-texture carbonate where partially dissolved, zoned dolomite precedes late calcite with subtle mottled zoning.

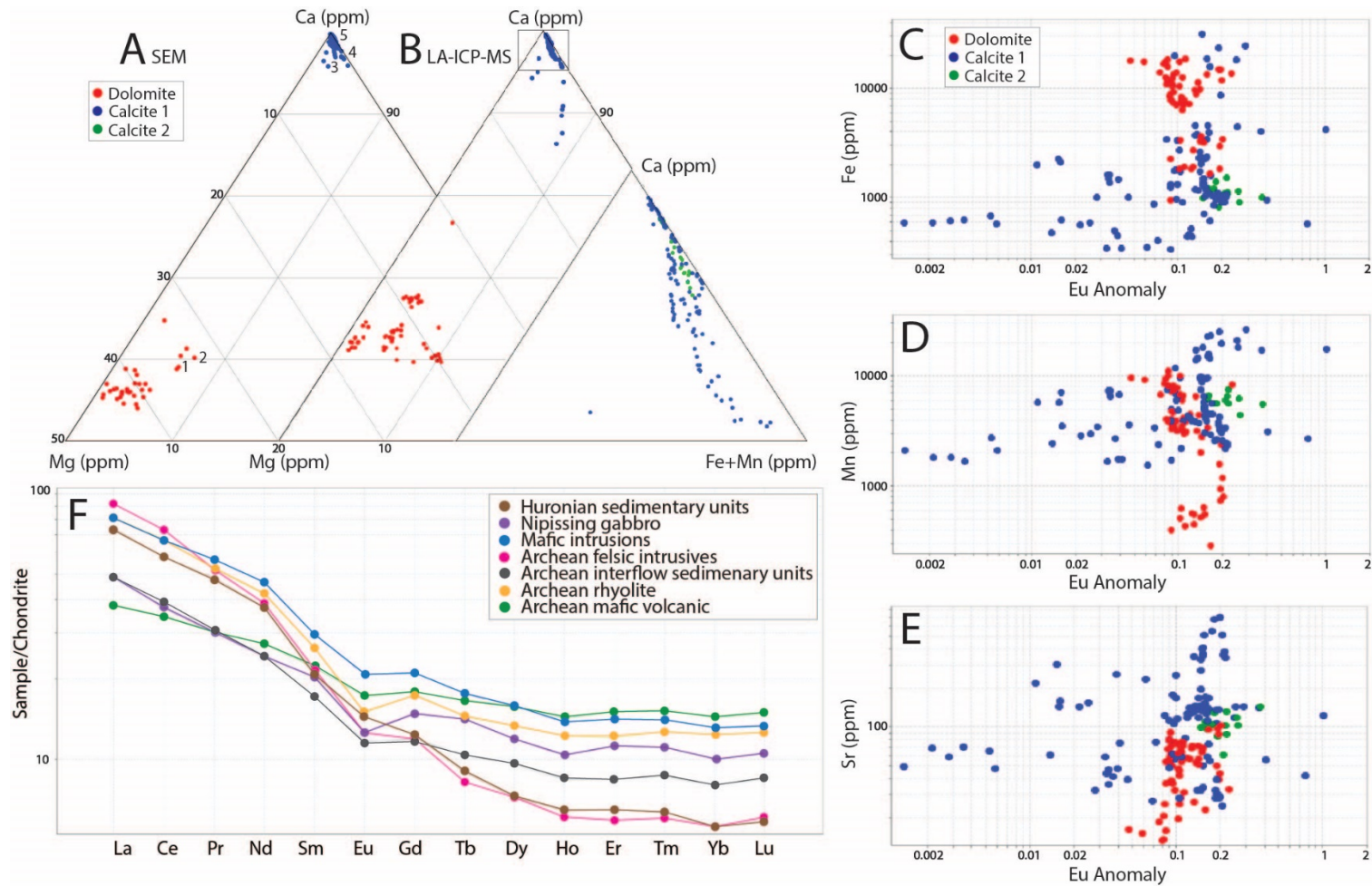


Figure 21. Major and trace-element data for vein carbonates. (A, B) Data plotted in Ca-Mg-(Fe+Mn) ternaries (>50% Ca component) as at.% in (A) and wt. % in (B). Note dolomite core and rim data overlap. For calcite data the Ca apex is enlarged to highlight two calcite generations. (C – E) Trace element data (Fe, Mn, Sr, respectively) plotted versus Eu anomaly. (F) Average chondrite-normalized REE plots in wt. % (using values of Sun and McDonough, 1989) for main lithologies in Cobalt (from White et al., 2020, in prep.).

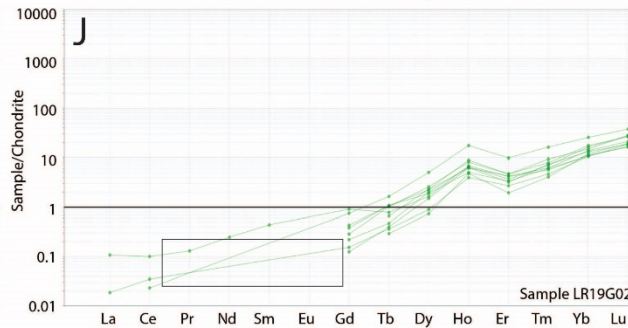
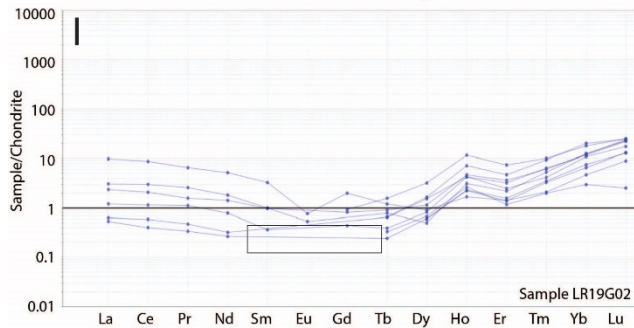
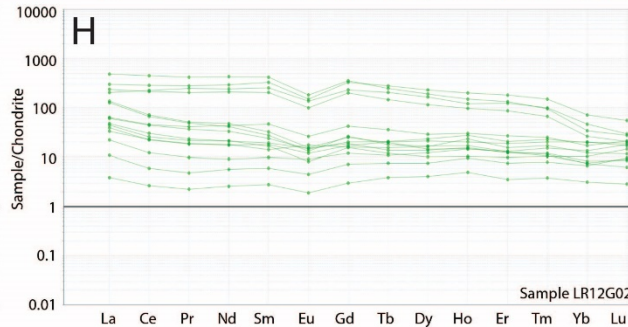
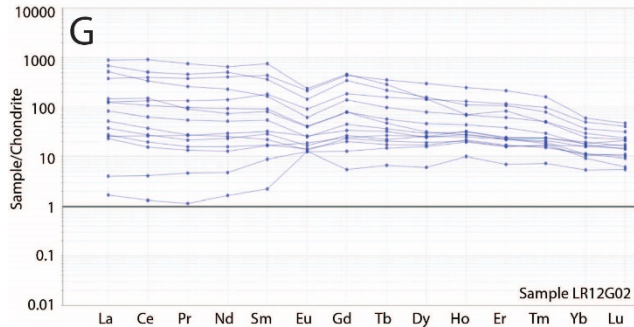
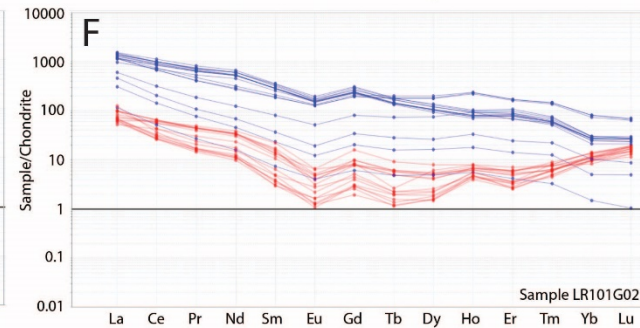
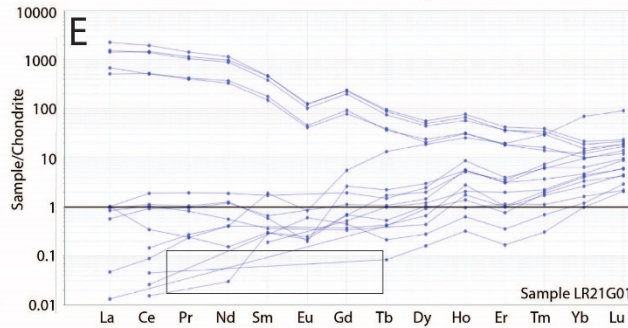
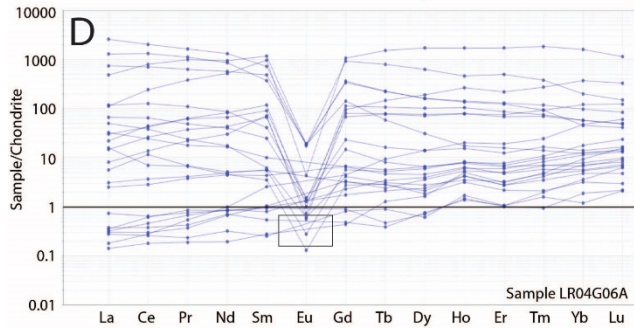
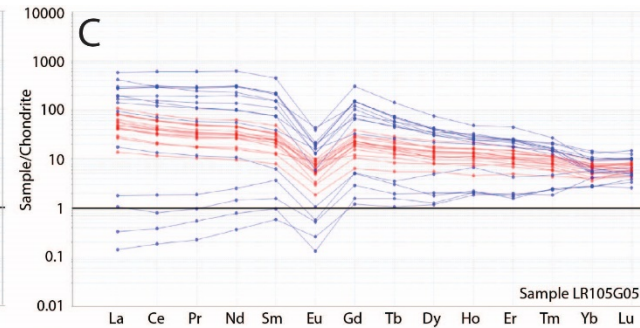
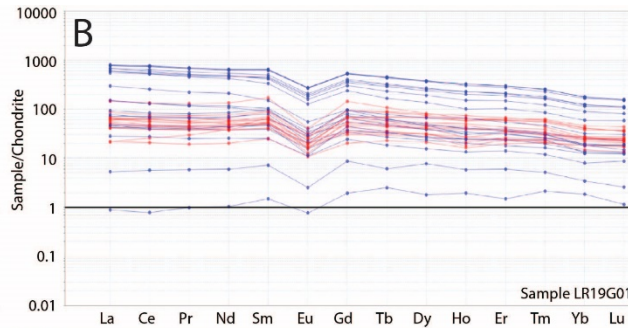
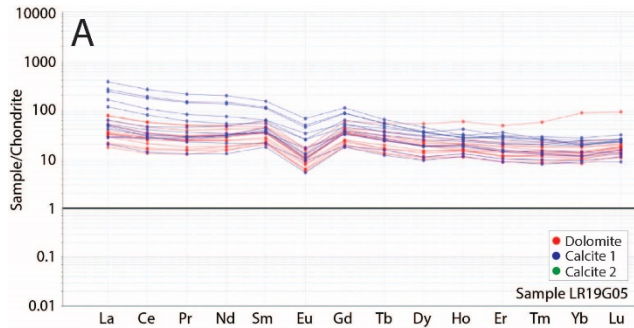


Figure 22. Chondrite-normalized REE plots for vein dolomite and calcite in wt. % (using values of Sun and McDonough, 1989). Note that the legend in A applies to the entire data set. Absence of data due to detection limits are outlined by black boxes, which infer data extrapolation.

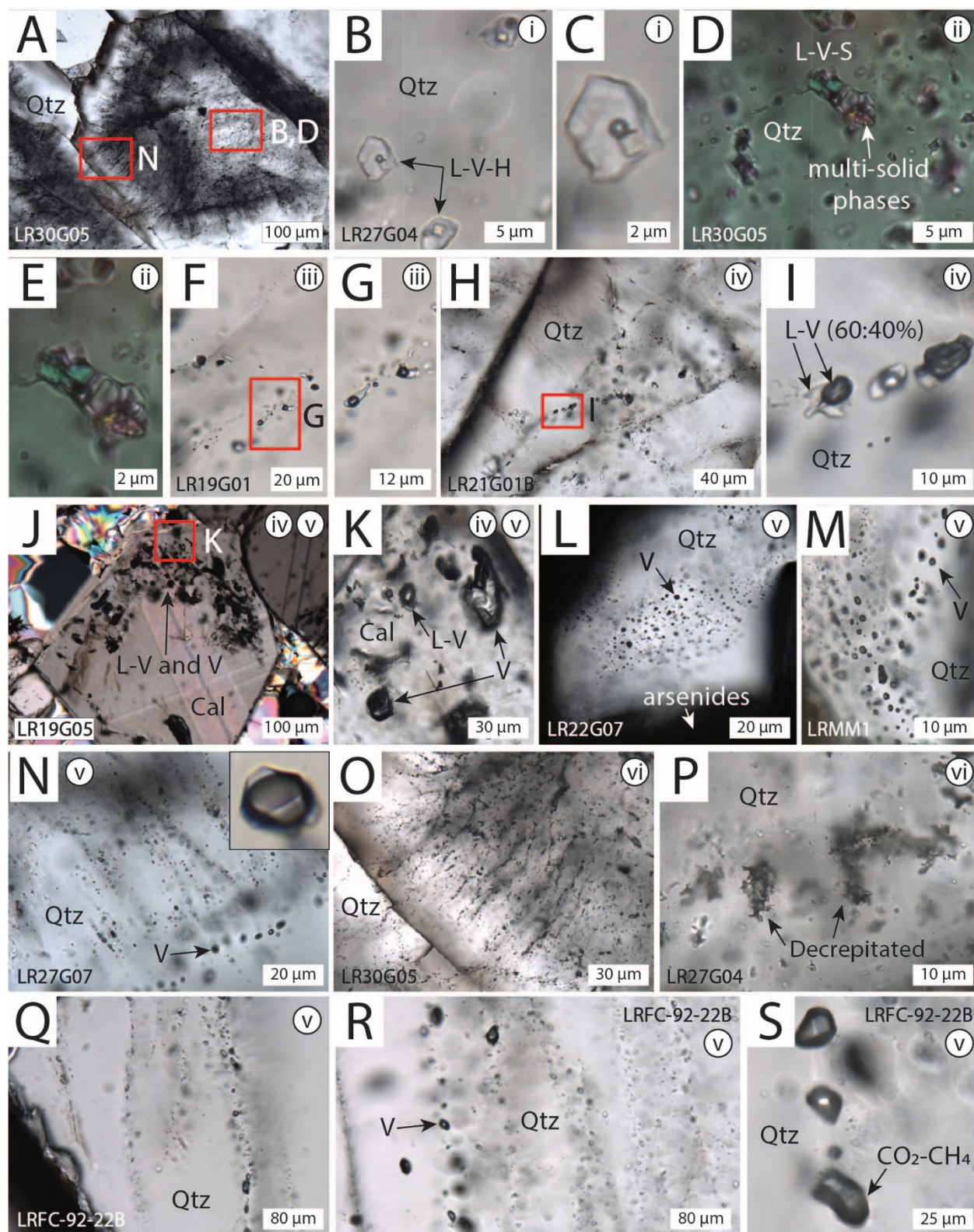


Figure 23. Petrographic images of fluid inclusion (FI) types in five-element veins as seen in plane (A-C, F-I, K-P) and cross-polarized (D, E, J) light. Picture enlargements are outlined as red boxes. Note that this figure is matched with the roman numerals to the fluid inclusion types

in Table 9 and schematic diagram Figure 24. (A) Comb quartz showing primary (and/or pseudosecondary) fluid inclusions coring quartz. (B) Close up of L-V-H-type found in comb quartz cores. (C) Enlargement of (B). (D) Close up of indeterminate L-V-S in comb quartz cores. Note the habit and the birefringence of the solid phases. (E) Enlargement of (D). (F) Pseudosecondary L-V (80:20) FI along late fractures in quartz (G) Enlargement of (F). (H) Pseudosecondary L-V (60:40) FI along late fractures in quartz. (I) Enlargement of (H). (J) Zonally arranged L-V and V-rich FI on the margins of euhedral calcite suggesting primary origin. (K) Enlargement of (J). (L) P V-type in quartz surrounded by arsenide rosettes. (M, N) V-type FI on secondary trails in quartz with close-up of V-rich inclusion with thin film of L as inset in N. (O) Arrays of decrepitated FI along growth trajectory of quartz. (P) Close up example of ubiquitous large decrepitated FI in undeformed comb quartz. (Q-S) V-rich inclusions in basement base-metal sulfide veins.

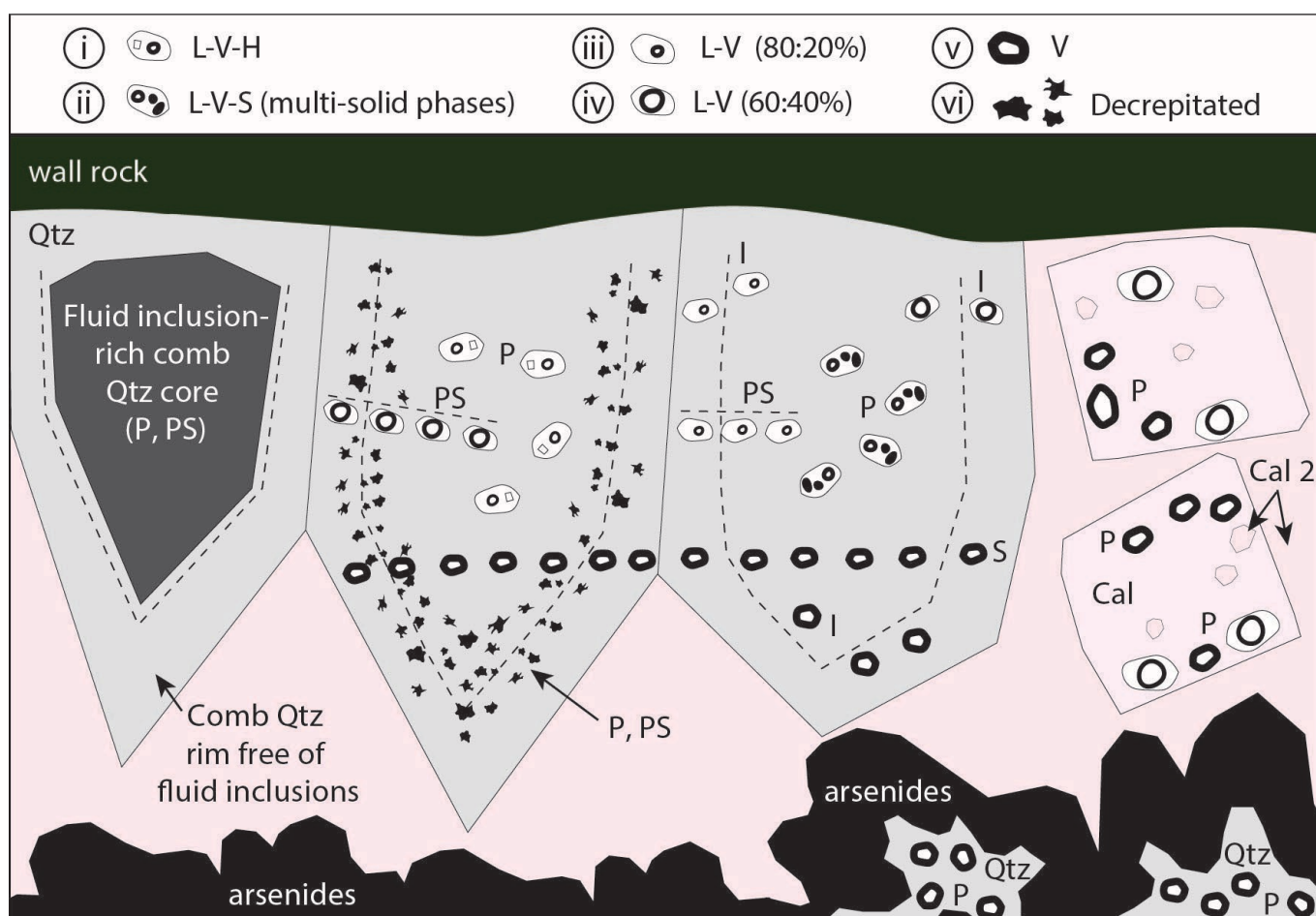


Figure 24. Schematic diagram of fluid inclusion assemblages (FIA) in the five-element veins. Abbreviations: L = liquid, V = vapor, H = halite, S = unknown solid phases, S = secondary, PS = pseudosecondary, P = primary, I = indeterminate.

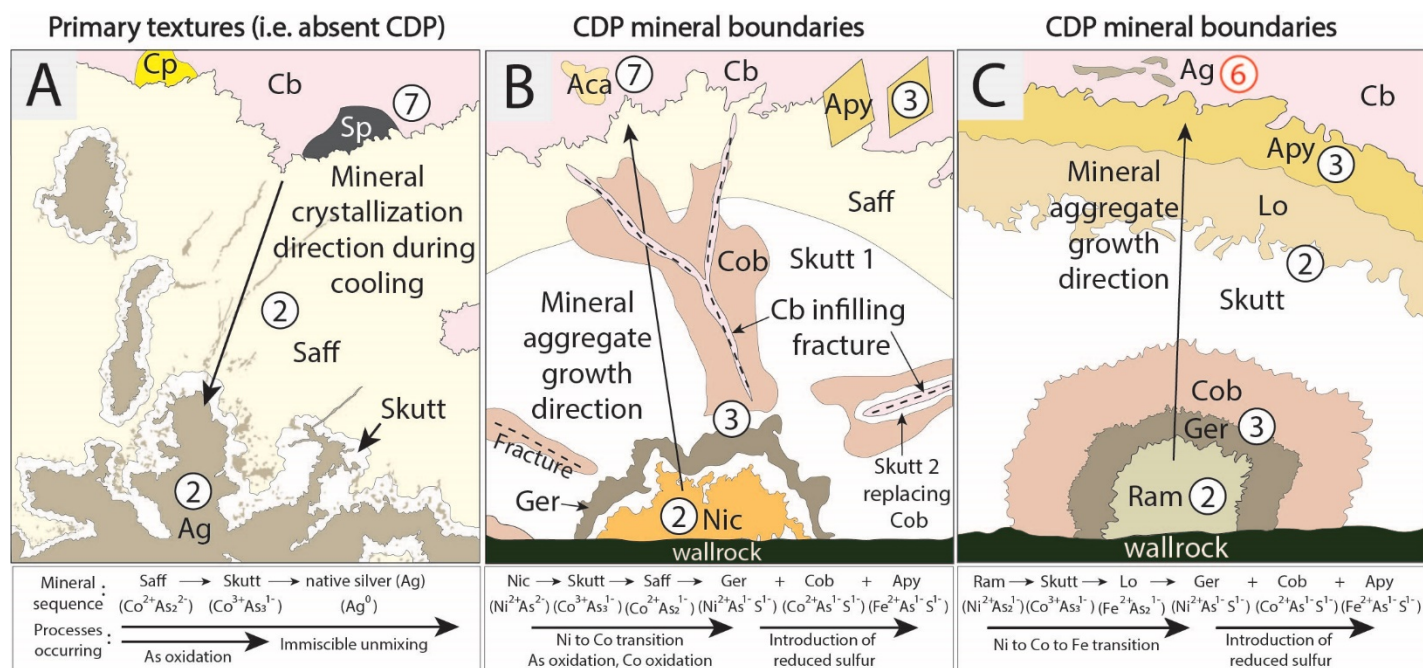


Figure 25. A subset of representative sequence of minerals and associated valence states of elements composing the minerals. Colours of the minerals reflect those seen in reflected (arsenides) or transmitted light (Cb). Numbers refer to vein paragenetic stages as in Figure 10.

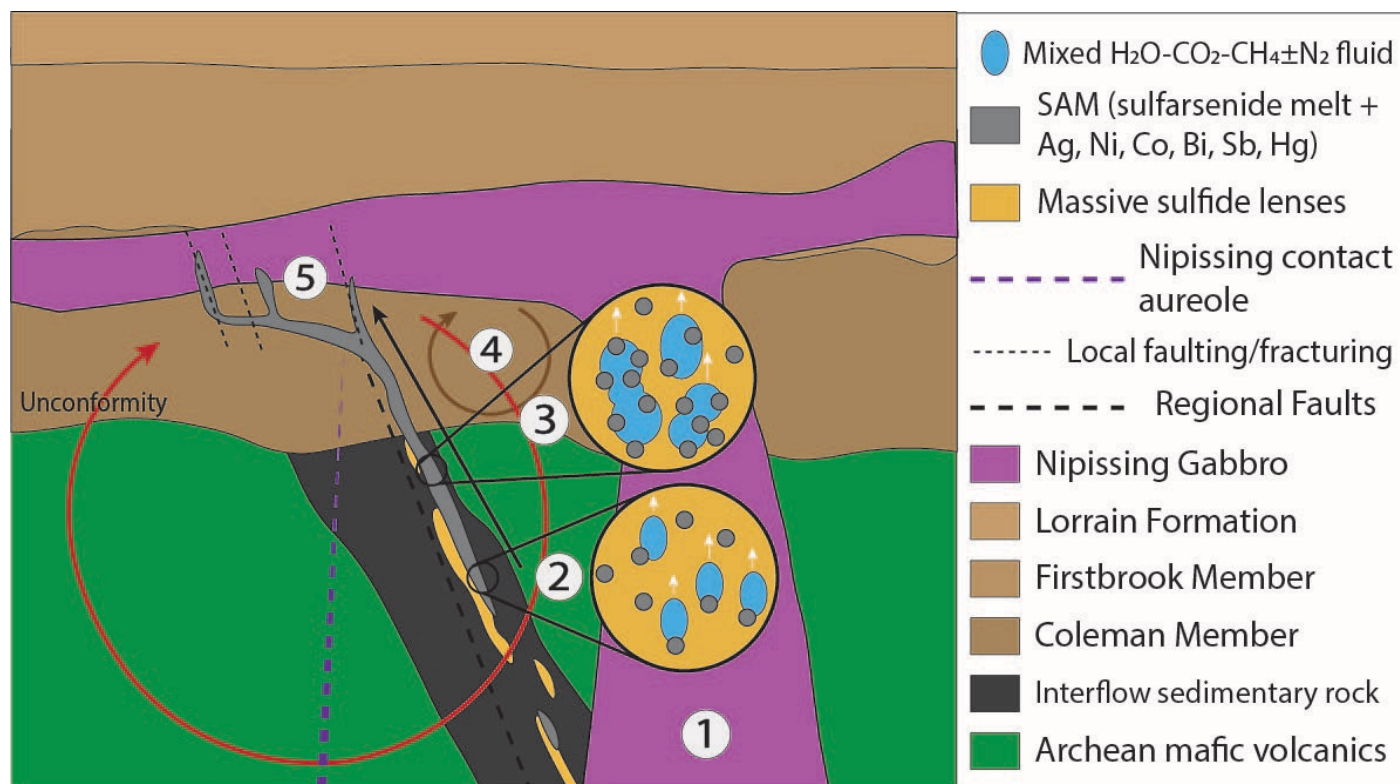


Figure 26. A proposed schematic genetic model for the Cobalt five-element vein system with numbers associated with the following events: (1) Nipissing gabbro intrudes country rock with proximal massive sulfide lenses in the Archean interflow sedimentary rock undergoing partial melting within its contact aureole. (2) Production of a sulfarsenide melt (SAM) containing Ag, Ni, Co, Bi, Sb and Hg and also generation of carbonic volatiles (CO₂+CH₄±N₂) that mix with convecting Huronian saline brine. The immiscible carbonic fluid floats the SAM upwards to the ore environment. (3) Aggregation of SAM upwards and injection into dilating veins. (4) Convection of Huronian saline brines, seen as L-V-Halite fluid inclusions, due to heating by the Nipissing gabbro. (5) Crystallization of the five-element veins due to undercooling via heat loss into the wall rock.